

© 2022

Schuyler C. Nardelli

ALL RIGHTS RESERVED

SEASONAL DYNAMICS OF PLANKTON ECOLOGY IN COASTAL ANTARCTICA

By SCHUYLER C. NARDELLI

A dissertation submitted to the

School of Graduate Studies

Rutgers, The State University of New Jersey

In partial fulfillment of the requirements

For the degree of

Doctor of Philosophy

Graduate Program in Oceanography

Written under the direction of

Oscar M. Schofield

And approved by

---

---

---

---

New Brunswick, New Jersey

May 2022

## ABSTRACT OF THE DISSERTATION

Seasonal dynamics of plankton ecology in coastal Antarctica

by SCHUYLER C. NARDELLI

Dissertation Director:  
Oscar M. Schofield

The West Antarctic Peninsula (WAP) has experienced significant increases in atmospheric and ocean temperatures since the 1950s, with subsequent decreases in winter sea ice extent and duration. Concurrently, phytoplankton biomass has decreased along the northern portion of the peninsula, associated with a shift from large-celled diatoms to smaller-celled cryptophytes and mixed flagellates, and krill populations previously located north of the peninsula have shifted their range south to coastal WAP waters. Despite these changes, a comprehensive understanding of the seasonal dynamics of coastal Antarctic phytoplankton and krill remains in question. Filling this gap in our understanding is crucial for contextualizing long-term change. This dissertation is focused on understanding the austral summer seasonal dynamics of plankton ecology at Palmer Station, Antarctica, and the resulting implications for predator foraging.

*Chapter 1* provides overall context for the observed changes and implications for ecology of the WAP. *Chapters 2 and 3* document phytoplankton seasonal succession and diversity using data from samples analyzed with an Imaging FlowCytobot. In *Chapter 2*, a convolutional neural network was built to automatically sort collected images of WAP phytoplankton, and in *Chapter 3* the neural network was applied to two field seasons of samples collected from Palmer Station. The findings highlight remarkable similarities in

phytoplankton seasonal succession between years despite significant differences in annual sea ice extent and total phytoplankton biomass. In both years, there was a tight connection between sea ice retreat and bloom initiation timing and a decrease in cell size from late spring to early autumn associated with increases in meteoric meltwater.

*In Chapter 4*, 12 years of autonomous underwater glider data from the Palmer region were paired with a photoacclimation model to characterize phytoplankton growth and bloom phenology from summer to early autumn. Results showed a distinct phase shift at the beginning of February caused by increased wind-mixing of sedimentary iron to surface waters, which increased growth rates and cellular chlorophyll concentrations, diluted predator concentrations reducing grazing pressure, and led to a significant autumn bloom.

*In Chapter 5*, bi-weekly acoustic surveys were conducted to evaluate seasonal changes in krill availability in adjacent Adélie and gentoo penguin foraging regions near Palmer Station. From summer to autumn, results showed a migration of adult krill inshore and an increase in diel vertical migration behavior. Additionally, there were significantly different oceanographic properties and krill swarming behaviors in Adélie and gentoo foraging regions only 10 km apart, suggesting a potential driver of differences in local penguin foraging behavior between species.

*Chapter 6* summarizes the main findings of the dissertation and suggests directions for future research. Ultimately, this dissertation improves our understanding of summer seasonal phytoplankton and krill dynamics, providing context for predicting how coastal Antarctic ecosystems might respond and adapt to continued environmental change.

## Acknowledgments

First and foremost, I would like to thank my advisor Dr. Oscar Schofield for being an amazing mentor and friend. From our first conversation, your dedication to your students was evident, and I could not have asked for a more supportive environment in which to build my research foundation. You have an incredible way of guiding students while still allowing them to build independence and confidence in their skills and abilities. I really appreciate your willingness to let me pursue my own scientific questions and interests, even if they were sometimes a bit outside your expertise. I have truly enjoyed working with you, and I hope our professional paths cross again in the future!

Thank you also to my dissertation committee, Grace Saba, Josh Kohut, and Doug Nowacek, for your additional support and guidance. Your different backgrounds and perspectives helped me to think more broadly about my research, which not only improved my dissertation but also helped me to learn and grow as a scientist.

I am grateful for the folks in the Oceanography department that supported me throughout my PhD. Thank you to all the professors that challenged me in classes, to the graduate program directors during my tenure, Yair Rosenthal and John Wilkin, to our faithful department chair, Oscar Schofield, and to all the administrative specialists who helped me navigate logistics throughout my time at Rutgers. I am also appreciative of the RU COOL group, including the glider team and technicians that helped me countless times throughout my research, and all the professors and students that made my Thursday mornings a little brighter throughout the pandemic. DMCS is such a warm and supportive community amidst a large university, and I am thankful to have found a home there.

Thank you to all the members of the Schofield lab I overlapped with during my time at Rutgers, including Nicole C., Filipa, Mike B., Quintin, and Michael C. Having successful role models ahead of me helping to guide me through the graduate school process was so valuable, and I am excited to see the work that comes out of the lab in the coming years. Thanks especially to Nicole Waite for all your hard work to keep the lab running – you are truly an inspiration! It was so easy and fun to work with you, and I really appreciate all your help analyzing samples for my dissertation.

I feel incredibly lucky that I had the opportunity to work for the Palmer LTER. I was originally drawn to the project for the science, but the people are what made my experience so special. I learned so much from every PI, grad student, post doc and technician I had the privilege of working with, all while having a ton of fun. Additional thanks to all the Palmer Station personnel that supported my science during my four trips to Antarctica. Palmer felt like a second home during graduate school thanks to all the friendly and supportive folks who work there.

I had an atypical graduate school experience in that I split my time between three places: Rutgers, Antarctica, and VIMS. I have made some truly incredible friends in all three places (too many to list!), and they all played a role in supporting me throughout my PhD. It is great to have friends who can talk science but also know how to have fun. I am so grateful for all the adventures we shared and I can't wait for future adventures!

A huge thank you to my family for being my cheerleaders through this endeavor. Nick and Neesha – thanks for being science role models and providing a great example of how to maintain healthy work-life balance. Sophie – your strength and resilience inspire me to push through my own challenges. Thanks for being a good friend and listener

during stressful moments of grad school. Mom and Dad – thank you for your endless love and encouragement, I feel so lucky every day to have parents as supportive as you!

And finally, to Jack – I feel so fortunate that research in Antarctica brought us together. Thanks for always knowing how to make me laugh and supporting me through all the ups and downs over the last 5 years, I can't wait for the next chapter!

Funding: A big thank you to my funding sources throughout my PhD including internal Rutgers funding (Rutgers Institute of Earth, Ocean, and Atmospheric Sciences graduate fellowship), external research funding (NSF Palmer Antarctica Long-Term Ecological Research project (PLR-1440435), NASA (19-IDS19-0085), and the Teledyne Webb Graduate Research Fellowship), and travel funding for conferences (MTS Travel Award).

# Table of Contents

Abstract of the Dissertation .....	ii
Acknowledgments.....	iv
List of tables.....	x
List of figures .....	xi
<b>1. Introduction.....</b>	<b>1</b>
<b>2. Developing a convolutional neural network to classify phytoplankton images collected with an Imaging FlowCytobot along the West Antarctic Peninsula .....</b>	<b>6</b>
2.1 Abstract .....	6
2.2 Introduction .....	7
2.3 Methods .....	9
2.3.1 <i>Phytoplankton image collection and processing</i> .....	9
2.3.2 <i>Model development</i> .....	10
2.3.3 <i>Model validation</i> .....	11
2.3.4 <i>Model application</i> .....	11
2.3.5 <i>Sea ice characterization</i> .....	12
2.4 Results .....	12
2.4.1 <i>Model accuracy</i> .....	12
2.4.2 <i>Phytoplankton seasonal succession at Palmer Station</i> .....	13
2.4.3 <i>Sea ice dynamics</i> .....	14
2.5 Discussion .....	14
2.5.1 <i>Model development: successes and challenges</i> .....	14
2.5.2 <i>Phytoplankton seasonal succession at Palmer Station</i> .....	17
2.5.3 <i>Conclusions and next steps</i> .....	19
2.6 Acknowledgments .....	21
2.7 Tables .....	22
2.8 Figures .....	23
<b>3. Coastal phytoplankton seasonal succession and diversity on the West Antarctic Peninsula .....</b>	<b>26</b>
3.1 Abstract .....	26
3.2 Introduction .....	27
3.3 Methods .....	30
3.3.1 <i>Sample collection</i> .....	30
3.3.2 <i>Phytoplankton pigment analysis</i> .....	31

3.3.3	<i>Phytoplankton species and size analysis</i> .....	32
3.3.4	<i>Defining phytoplankton seasonal succession phases</i> .....	35
3.3.5	<i>Nutrient analyses</i> .....	36
3.3.6	<i>Meltwater composition</i> .....	37
3.3.7	<i>Water column stability</i> .....	37
3.3.8	<i>Weather data</i> .....	38
3.3.9	<i>Sea ice data</i> .....	38
3.3.10	<i>Statistical analyses</i> .....	39
3.4	Results	39
3.4.1	<i>HPLC versus IFCB taxonomy comparison</i> .....	39
3.4.2	<i>Interannual differences</i> .....	40
3.4.3	<i>Spring-autumn environmental trends</i> .....	42
3.4.4	<i>Spring-autumn phytoplankton succession patterns</i> .....	43
3.5	Discussion	45
3.5.1	<i>Drivers of interannual differences in phytoplankton biomass and composition</i> .....	46
3.5.2	<i>Drivers of phytoplankton seasonal succession</i> .....	49
3.5.3	<i>HPLC versus IFCB-derived abundance and taxonomy</i> .....	53
3.6	Acknowledgments	58
3.7	Tables	60
3.8	Figures	63
3.9	Supplementary tables	71
3.10	Supplementary figures	73
<b>4.</b>	<b>Assessing ecological drivers of phytoplankton bloom phenology in coastal Antarctica</b> .....	<b>76</b>
4.1	Abstract	76
4.2	Introduction	77
4.3	Methods	79
4.3.1	<i>Glider data collection</i> .....	79
4.3.2	<i>Mixed layer depth calculations</i> .....	81
4.3.3	<i>Palmer Station weather data</i> .....	82
4.3.4	<i>Phytoplankton division, accumulation, and loss rates</i> .....	82
4.3.5	<i>Station E data</i> .....	85
4.3.6	<i>Climatology calculations</i> .....	86
4.3.7	<i>Statistical analyses</i> .....	86
4.4	Results	86
4.4.1	<i>Modeled <math>C_{phyto}</math></i> .....	86
4.4.2	<i>Seasonal climatology</i> .....	87
4.5	Discussion	89
4.5.1	<i>Seasonal bloom phenology</i> .....	89

4.5.2	<i>Phytoplankton specific division and loss rates</i> .....	92
4.5.3	<i>Relationship between <math>C_{phyto}</math> and <math>b_{bp}(470)</math></i> .....	94
4.5.4	<i>Conclusion</i> .....	97
4.6	Acknowledgments	99
4.7	Tables	100
4.8	Figures	102
4.9	Supplementary Figures	109
<b>5.</b>	<b>Krill availability in adjacent Adélie and gentoo penguin foraging regions near Palmer Station, Antarctica.....</b>	<b>110</b>
5.1	Abstract	110
5.2	Introduction	111
5.3	Methods	114
5.3.1	<i>Survey design</i> .....	114
5.3.2	<i>Acoustic data collection</i> .....	115
5.3.3	<i>Krill net sampling</i> .....	115
5.3.4	<i>Acoustic data processing</i> .....	116
5.3.5	<i>Environmental data</i> .....	119
5.3.6	<i>Statistical analysis</i> .....	120
5.4	Results	123
5.4.1	<i>Krill population characteristics</i> .....	123
5.4.2	<i>Spatial variability</i> .....	123
5.4.3	<i>Spatiotemporal variability in krill density</i> .....	124
5.4.4	<i>Seasonal patterns</i> .....	125
5.5	Discussion	127
5.5.1	<i>Krill population characteristics</i> .....	127
5.5.2	<i>Spatial variability</i> .....	128
5.5.3	<i>Spatiotemporal variability in krill density</i> .....	130
5.5.4	<i>Seasonal patterns</i> .....	132
5.5.5	<i>Conclusions</i> .....	134
5.6	Acknowledgments	136
5.7	Tables	137
5.8	Figures	139
5.9	Supporting Information	146
<b>6.</b>	<b>Summary and Conclusions .....</b>	<b>150</b>
<b>7.</b>	<b>Acknowledgment of previous publications.....</b>	<b>154</b>
<b>8.</b>	<b>References.....</b>	<b>155</b>

## List of tables

### Chapter 2

Table 1: Confusion matrix for broad taxonomic groups.....	22
Table 2: Sea ice characterization.....	22

### Chapter 3

Table 1: Compiled size metrics for each taxonomic group.....	60
Table 2: Annual sea ice indices.....	60
Table 3: Interannual differences in environmental variables.....	61
Table 4: Interannual differences in phytoplankton variables.....	62
Supplementary table 1: Interannual differences in phytoplankton taxonomy.....	71

### Chapter 4

Table 1: Glider deployment information.....	100
---	-----

### Chapter 5

Table 1: Differences between Adélie and gentoo penguin foraging regions.....	137
Table 2: Differences in krill variables across survey legs in each foraging region.....	138
Table S1: Differences in environmental variables across survey legs in each foraging region.....	146
Table S2: Temporal change of variables inshore and offshore in the Adélie region.....	147
Table S3: Temporal change of variables inshore and offshore in the gentoo region.....	148
Table S4: Temporal change of variables within each foraging region.....	149

## List of figures

### **Chapter 2**

Figure 1: Methods comparison of phytoplankton seasonal succession.....	23
Figure 2: Diatom seasonal diversity.....	24
Figure 3: Percent sea ice coverage.....	25

### **Chapter 3**

Figure 1: Map of the West Antarctic Peninsula and Palmer region.....	63
Figure 2: Historical timeseries for number of sea ice days and chlorophyll- <i>a</i> .....	64
Figure 3: Seasonal HPLC-derived chlorophyll- <i>a</i> and IFCB-derived phytoplankton biovolume for each taxonomic group.....	65
Figure 4: Daily percent sea ice cover and percent sea ice melt.....	66
Figure 5: Seasonal timeseries of environmental variables.....	67
Figure 6: Seasonal timeseries of nutrient data.....	68
Figure 7: Seasonal timeseries of the Shannon Diversity Index.....	69
Figure 8: Diatom seasonal diversity.....	69
Figure 9: Seasonal decrease in phytoplankton median cell diameter.....	70
Supplementary figure 1: Comparison of live versus preserved IFCB samples.....	73
Supplementary figure 2: Phytoplankton successional phase divisions.....	74
Supplementary figure 3: Linear relationship between HPLC-derived chlorophyll- <i>a</i> and IFCB-derived phytoplankton biovolume.....	74
Supplementary figure 4: Linear relationship between HPLC-derived chlorophyll- <i>a</i> and IFCB-derived phytoplankton biovolume for each taxonomic group.....	75

### **Chapter 4**

Figure 1: Map of Palmer Deep region and all glider profiles.....	102
Figure 2: Seasonal coverage of glider deployments.....	103
Figure 3: Daily $b_{bp}(470)$ versus PaM-derived $C_{phyto}$ .....	104
Figure 4: Seasonal climatologies of environmental variables.....	105

Figure 5: Monthly differences in environmental climatologies.....	106
Figure 6: Seasonal climatologies of phytoplankton variables.....	107
Figure 7: Monthly differences in phytoplankton climatologies.....	108
Supplementary figure 1: Linear relationship between solar irradiance and PAR.....	109
Supplementary figure 2: Annual summer timeseries for chlorophyll- <i>a</i> , $C_{\text{phyto}}$ , and $b_{\text{bp}}(470)$ .....	109

## **Chapter 5**

Figure 1: Map of penguin foraging regions and acoustic surveys.....	139
Figure 2: <i>Euphausia superba</i> monthly length frequency distributions.....	140
Figure 3: Regional differences in environmental variables.....	141
Figure 4: Regional differences in krill variables.....	142
Figure 5: Krill variable differences across survey legs in the Adélie foraging region.....	143
Figure 6: Seasonal spatiotemporal trends in krill biomass.....	144
Figure 7: Summer timeseries of physical and biological properties in Adélie and gentoo penguin foraging regions.....	145

## 1. Introduction

The West Antarctic Peninsula (WAP) is a highly productive marine ecosystem characterized by large summer phytoplankton blooms that support abundant krill and top predator populations (Ross et al. 1996). A bathymetric gradient from the coast out to the continental slope, deep submarine canyons that cut across the shelf, and a network of coastal islands set up complex physical dynamics that drive the abundance and distribution of these organisms (Fraser and Trivelpiece 1996; Santora and Reiss 2011; Kavanaugh et al. 2015). In addition, the life histories of many marine species are highly synchronized with sea ice seasonality (Eicken 1992).

The WAP is one of the fastest warming regions on Earth, with winter air and surface ocean temperatures increasing by 6°C and >1°C, respectively, since 1951 (Meredith and King 2005; Turner et al. 2005; Cook et al. 2016). In response, >90% of marine glaciers are currently in retreat, and the annual ice season duration decreased by 3.3 months from 1979 to 2011 (Stammerjohn et al. 2012; Cook et al. 2016). Additionally, the Southern Annular Mode (SAM) has become more positive during austral summer, contracting the westerly wind band around Antarctica (Thompson and Solomon 2002). This strengthens warm westerly winds along the WAP, increases precipitation, and increases the amount of warm (~2°C) Upper Circumpolar Deep Water (UCDW) that is upwelled onto the continental shelf (Thomas et al. 2008; Martinson and McKee 2012). All of these factors set up a latitudinal climate gradient along the WAP, with warm, moist, sub-polar conditions propagating south to replace cold, dry, polar conditions (Ducklow et al. 2013). The Palmer Deep submarine canyon, located near the U.S.

research base Palmer Station on Anvers Island, is in the transition zone between polar and subpolar climates, making it an ideal location to study ecosystem changes.

Along the WAP, phytoplankton show strong interannual and regional variability timed with sea ice retreat and increased light availability (Vernet et al. 2008). Large diatom-dominated spring blooms are initiated when solar warming and sea ice melt stabilize the upper water column and nutrients are abundant (Mitchell and Holm-Hansen 1991; Prézelin et al. 2000; Venables et al. 2013). From 1978 to 2006, decreased sea ice extent and increased wind speeds north of Palmer Station in January led to deeper vertical mixing and increased light limitation, resulting in significant decreases in mean phytoplankton biomass (Montes-Hugo et al. 2009). From 2006 to 2015, the southern boundary of decreasing chlorophyll trends shifted roughly 400 km south, indicating that phytoplankton could be declining along the entire WAP by 2030 (Rogers et al. 2020). Decreases in biomass are accompanied by a shifts to a smaller fraction of large cells, including diatoms (Montes-Hugo et al. 2009). It is hypothesized that this is due to increased proportions of small-celled cryptophytes, concurrent with an increase in low salinity meltwater along the coast (Moline et al. 2004; Mendes et al. 2013; Schofield et al. 2017). Future expansion of low salinity surface waters are predicted to continue increasing the prevalence of smaller-celled phytoplankton communities along the WAP (Moline et al. 2004; Li et al. 2009; Hernando et al. 2015).

Antarctic krill (*Euphausia superba*) are the main trophic link between phytoplankton and top predators in this region, and interannual patterns in abundance and recruitment are tightly coupled to phytoplankton biomass (Atkinson et al. 2004; Saba et al. 2014). Krill feeding appendages filter particles >10 microns, thus grazing efficiencies

are higher when larger particles (e.g., diatoms) are present (McClatchie and Boyd 1983). Despite changes in the environment and phytoplankton community, krill abundance south of Palmer Station remained relatively stable from 1993 to 2013 (Steinberg et al. 2015). However, from 1976 to 2016 there was a krill abundance decline in the southwest Atlantic sector, and a southward range contraction that concentrated krill distribution along the WAP shelf (Atkinson et al. 2019). Further warming and melting could cause additional range contractions and decreased krill biomass further south along the WAP (Klein et al. 2018).

With sea ice loss and increased snowfall, polar, ice-obligate Adélie penguin (*Pygoscelis adeliae*) populations with well-established (hundreds to thousands of years; Emslie 2001) colonies near Palmer Station have declined by ~90% since the 1970s, while sub-Antarctic, ice-intolerant gentoo penguins (*Pygoscelis papua*) established colonies near Palmer Station in 1994 and have been increasing ever since (Fraser et al. 2020). Krill are the main food source for many predators along the WAP, including seabirds, whales, and seals. Reduced krill biomass and recruitment success could increase foraging efforts and decrease breeding success for these animals (Fraser and Hofmann 2003; Trathan et al. 2007; Chapman et al. 2011), causing further declines in Adélie penguin populations.

Understanding the seasonal dynamics of coastal Antarctic phytoplankton and krill is crucial for predicting how future environmental change will impact food web structure. Seasonal changes in the environment (e.g., solar irradiance, wind speed, sea ice retreat, meltwater inputs, depth of the surface mixed layer, nutrient availability) impact the timing and magnitude of phytoplankton blooms, patterns in phytoplankton species

succession, and cell size dynamics (Li et al. 2009; Hernando et al. 2015; Behrenfeld et al. 2017, 2021a). While environmental and phytoplankton dynamics impact krill recruitment on interannual scales (Saba et al. 2014), seasonal abundance and distribution of krill are primarily determined by their life cycles. From summer to autumn, adult krill migrate from the shelf break to inshore troughs and canyons, while juvenile krill remain in coastal waters (Siegel et al. 2013; Conroy et al. 2020). Adult krill also migrate deeper in the water column in autumn to utilize deep food sources (Cleary et al. 2016; Reiss et al. 2017), while larval and juvenile krill remain shallow to assess under-ice algae (Bernard et al. 2018; Walsh et al. 2020). Seasonal changes in lower trophic levels ripple up the food web to impact predators. For example, Adélie and gentoo penguins appear to time peak chick fledging with seasonal deepening of krill biomass (Nardelli et al. 2021a), likely because obtaining high krill yields during periods of peak chick growth is critical for chick survival and shallow krill mean reduced foraging efforts.

The overarching goal of this dissertation was to assess the austral summer seasonal dynamics of plankton ecology at Palmer Station and the resulting implications for predator foraging. Chapters 2 and 3 utilized new imaging technology to assess phytoplankton diversity and community dynamics. In Chapter 2, a convolutional neural network was built to automatically sort millions of collected phytoplankton images along the WAP, and in Chapter 3 this neural network was applied to data from Palmer Station to describe phytoplankton seasonal succession patterns and their environmental drivers. Chapter 4 builds on this understanding of seasonal phytoplankton trends using 12 years of autonomous underwater glider data from the Palmer region to model phytoplankton bloom phenology and determine connections to bottom-up and top-down ecological

drivers. Chapter 5 uses acoustic technology to evaluate seasonal changes in krill availability in the Palmer region and the foraging implications for local Adélie and gentoo penguin colonies. Finally, Chapter 6 summarizes the main findings of the dissertation and suggests directions for future research.

## **2. Developing a convolutional neural network to classify phytoplankton images collected with an Imaging FlowCytobot along the West Antarctic Peninsula**

### **2.1 Abstract**

High-resolution optical imaging systems are quickly becoming universal tools to characterize and quantify microbial diversity in marine ecosystems. Automated detection systems such as convolutional neural networks (CNN) are often developed to identify the immense number of images collected. The goal of our study was to develop a CNN to classify phytoplankton images collected with an Imaging FlowCytobot for the Palmer Antarctica Long-Term Ecological Research project. A medium complexity CNN was developed using a subset of manually-identified images, resulting in an overall accuracy, recall, and f1-score of 93.8%, 93.7%, and 93.7%, respectively. The f1-score dropped to 46.5% when tested on a new random subset of 10,269 images, likely due to highly imbalanced class distributions, high intraclass variance, and interclass morphological similarities of cells in naturally occurring phytoplankton assemblages. Our model was then used to predict taxonomic classifications of phytoplankton at Palmer Station, Antarctica over 2017-2018 and 2018-2019 summer field seasons. The CNN was generally able to capture important seasonal dynamics such as the shift from large centric diatoms to small pennate diatoms in both seasons, which is thought to be driven by increases in glacial meltwater from January to March. Moving forward, we hope to further increase the accuracy of our model to better characterize coastal phytoplankton communities threatened by rapidly changing environmental conditions.

## 2.2 Introduction

The West Antarctic Peninsula (WAP) is a highly productive marine ecosystem characterized by large summer phytoplankton blooms that support extensive krill and top predator populations (Ducklow et al. 2013). The WAP is experiencing significant environmental change, threatening this unique and productive ecosystem. One of the fastest warming regions on Earth, WAP winter air temperatures and surface ocean temperatures have increased by 6°C and >1°C, respectively, over the past 50 years (Meredith and King 2005; Turner et al. 2005; Cook et al. 2016). In response, 90% of marine glaciers are currently in retreat, the annual ice season has decreased by 92 days over the last 35 years, and there is no longer perennial sea ice in the northern WAP (Stammerjohn et al. 2012; Cook et al. 2016).

Ocean warming and melting sea ice have impacted the phytoplankton community, which has implications for the entire food web. Phytoplankton biomass has significantly decreased in the northern WAP, associated with a shift from large-celled diatoms to smaller-celled cryptophytes and mixed flagellates (Montes-Hugo et al. 2009). This shift is concurrent with an increase in low salinity meltwater (Moline et al. 2004; Mendes et al. 2013; Schofield et al. 2017). The increased spatial coverage of low salinity surface waters associated with continued glacial and sea ice melt is predicted to increase the prevalence of smaller-celled phytoplankton communities along the WAP, with important implications for food web structure and energy transfer efficiency (Sailley et al. 2013).

The Palmer Long-Term Ecological Research project (PAL-LTER) was established in 1991 to investigate how changes in sea ice structure the pelagic ecosystem and biogeochemistry along the WAP. The project has previously used High Performance

Liquid Chromatography (HPLC) analysis of pigment data to characterize the taxonomic composition of phytoplankton assemblages (Kozłowski et al. 2011). This technique uses marker pigments of phytoplankton groups to assess their contribution to the overall abundance. However, HPLC lacks more detailed taxonomic classification and cell size information that is critical to understanding how warming and melting impacts phytoplankton communities along the WAP.

To fill this knowledge gap, in 2017 the PAL-LTER acquired an Imaging FlowCytobot (IFCB; McLane Labs, Falmouth, MA, USA). The IFCB is an automated imaging-in-flow submersible cytometer that uses a combination of video and flow cytometric technology to collect images and measure chlorophyll fluorescence and scattered light for each particle (~10-150  $\mu\text{m}$ ) in a 5 mL water sample (Olson and Sosik 2007). These images can be analyzed to determine cell size dynamics, and sorted taxonomically to the genus or species level, thus providing much more detailed organismal information than HPLC methods.

However, the IFCB can generate more than 10,000 high-quality images every hour, which becomes an immense amount of data over the duration of a research cruise or field season. This volume of data makes manual image identification impractical, therefore, these imaging platforms are often complemented by automated detection systems that allow for rapid and precise classification of plankton communities. Currently, there are two typical machine learning approaches for IFCB images: (1) a support vector machine based on a feature selection algorithm (88% overall accuracy with 22 classes; Sosik and Olson 2007), and (2) random forest (RF) algorithms (~70% overall accuracy depending on the model and number of classes, e.g., Picheral et al. 2017). Following

advancements in the field of computer vision through deep learning (LeCun et al. 2015) the IFCB community is now transitioning to convolutional neural networks (CNNs) for improved accuracy in image classification. CNNs extract features directly from images. Starting with raw imagery and labels, semantically meaningful features are learned as the network trains on a set of images. In theory, extracted features correspond to components of the image relevant to the labels, which makes these models highly accurate and well-suited for image classification tasks.

Since 2017, the PAL-LTER has collected over 10 million images spanning four summer field seasons. The goal of our study was to develop a CNN to sort WAP phytoplankton into taxonomic groups. This would allow for taxonomic classification of entire seasons of collected phytoplankton data in a short amount of time. Additionally, the CNN could be used as a tool to characterize phytoplankton communities in the field in near-real time to inform opportunistic sampling strategies. The combination of the IFCB and a high-accuracy automated classification system would allow the PAL-LTER to learn more about shifts in phytoplankton community and size dynamics associated with rapidly changing environmental conditions.

## **2.3 Methods**

### *2.3.1 Phytoplankton image collection and processing*

IFCB data were collected along the West Antarctic Peninsula over three summer field seasons: 2017-2018, 2018-2019, and 2019-2020. Whole water samples were collected at various depths from both the January cruise along the WAP (Anvers Island in the north to Charcot Island in the south) and from seasonal (November-March) sampling

at Palmer Station, Antarctica. 5 mL from each sample was analyzed with the IFCB to acquire images for each phytoplankton cell in the sample. Samples were passed through a 150  $\mu\text{m}$  Nitrex screen prior to analysis to prevent large cells from clogging the IFCB's flow cell. Cells with a major axis length  $< 25$  pixels (7.35  $\mu\text{m}$ ) were eliminated from the analysis as the resolution of the images was insufficient to provide clear identification.

Images were processed using methods and software from (Sosik and Olson 2007) (<https://github.com/hsosik/ifcb-analysis/wiki>). Image processing results in a set of 233 features describing each image including fluorescence, scattering intensity, equivalent spherical diameter, area, volume, and other morphometric parameters such as image texture and histogram of oriented gradients.

### 2.3.2 *Model development*

Processed images, metadata, and their associated features were uploaded to the web application EcoTaxa (<https://ecotaxa.obs-vlfr.fr>) (Picheral et al. 2017). Using EcoTaxa, a subset of 18,699 images was visually inspected and manually classified into 38 living groups (taxonomic resolution ranging from genus to class) and 2 non-living groups (detritus and bubbles), with at least 100 images per group. Samples (images + features) were augmented to increase training sample size via image rotations, flips, gaussian noise, and contrast changes. Features were also randomly multiplied by a factor between 0.8 and 1.2.

After augmentation, a training dataset of 40,000 samples with 1,000 in each class was used to develop a medium complexity CNN (8 convolutional layers and 2 million parameters), and 3,740 unaugmented images, approximately evenly split across classes,

were used as a validation dataset. Model precision, recall, and f1-score were calculated for the unmerged data considering all included groups, and for merged data considering only 8 general taxonomic groupings (pennate and centric diatoms, cryptophytes, prasinophytes, mixed flagellates, haptophytes, microzooplankton, and other). The “other” group includes primarily detritus with some bubbles. Precision is defined as true positives divided by the sum of true positives and false positives; it is the proportion of positive identifications that are correct. Recall is defined as true positives divided by the sum of true positives and false negatives; it is the proportion of actual positives that are identified correctly. The f1-score is the harmonic mean of precision and recall. Confusion matrices were also generated showing the percent of manually validated images predicted in each category by the CNN.

### *2.3.3 Model validation*

We tested the model on a random subset of 10,269 new images filtered by cell major axis length  $> 25$  pixels. Additionally, we used EcoTaxa’s RF algorithm to predict on the same images, using a maximum of 500 images per group. Predictions from both models were compared to manual identification of the images. Model precision, recall, and f1-score were calculated for unmerged and merged data for both the CNN and RF models, and a confusion matrix was generated for the CNN.

### *2.3.4 Model application*

After training and evaluation, our model was used to predict taxonomic classifications of phytoplankton collected at 0 m from Station B near Palmer Station,

Antarctica over the 2017-2018 and 2018-2019 summer field seasons. CNN predictions were compared to manual validation of the images to determine the accuracy of the predicted seasonal trends.

### 2.3.5 *Sea ice characterization*

Sea ice data were calculated using version 3.1 of the GSFC Bootstrap sea ice concentrations. Sea ice duration is the time elapsed between day of advance and day of retreat. All sea ice metrics use the 200 km area south and west of Palmer Station. See (Stammerjohn et al. 2008a) for more information.

## 2.4 Results

### 2.4.1 *Model accuracy*

The overall precision, recall, and f1-score of the model were 93.8%, 93.7%, and 93.7%, respectively. After merging the initial set of 40 classes into the 8 broader taxonomic groups, the precision, recall, and f1-score of the model all increased to 96.5%. Accuracy per group was > 95% for all groups except for microzooplankton (> 80%), mixed flagellates (> 90%), and other (> 90%).

Using the model to predict on the 10,269 new images resulted in unmerged and merged f1-scores of 46.5% and 47.6%, respectively. This is a 12% increase in the unmerged f1-score over EcoTaxa's random forest model (46.5% vs. 41.5%, respectively; (Picheral et al. 2017)). The model predicted most accurately for pennate diatoms (92.9%), and performed moderately well for microzooplankton (66.7%), mixed flagellates (66.2%), cryptophytes (65.0%), and centric diatoms (64.3%; Table 1). Our model was least precise

predicting prasinophytes (39.6%) and other cells (14.9%; Table 1). Only one haptophyte was manually identified in the random dataset but was predicted correctly.

#### 2.4.2 *Phytoplankton seasonal succession at Palmer Station*

Overall, the CNN captured important seasonal trends in phytoplankton dynamics. In both the 2017-2018 and 2018-2019 seasons, peak phytoplankton biovolume occurred midsummer (1 January 2018 and 4 February 2019; Fig. 1). In 2017-2018, the peak was dominated by a mix of cryptophytes, prasinophytes, and mixed flagellates, while in 2017-2018 the peak was dominated by pennate diatoms. The CNN also captured spring and autumn peaks composed of centric diatoms in 2018-2019 (Fig. 1C-D).

However, there are several discrepancies between methods. In both field years, but particularly 2017-2018, there were many cells manually identified as “other” that were classified as both mixed flagellates and prasinophytes by the CNN (Fig. 1). In this manner, the CNN appears to overestimate the abundance of these groups. The CNN also underestimated the abundance of cryptophytes, especially during peak biovolume in both years. Importantly, this misclassification of “other” cells also greatly overestimates the phytoplankton biovolume compared to manual validation, causing the phytoplankton peak in 2017 to appear much higher than for manual validation (Fig. 1A-B).

The CNN also captured interesting seasonal trends in the diatom community. There was less total diatom biovolume in 2017-2018 compared to 2018-2019 (Fig. 2A, 2D). In both seasons, centric diatoms shifted from a dominance of  $> 20 \mu\text{m}$  cells in November and December, to a dominance of 10-15  $\mu\text{m}$  cells in February and March (Fig. 2B, 2E). Pennate diatoms were consistently dominated by cells  $< 10 \mu\text{m}$ , with an increase

in biovolume during February and March, especially in 2018-2019 (Fig. 2C, 2F). Both seasons were primarily dominated by centric diatoms, with the notable exception of a large peak in pennate diatom biovolume in 2018 (Fig. 2A, 2D).

### 2.4.3 *Sea ice dynamics*

2017 had lower maximum winter sea ice coverage and shorter sea ice duration than 2018, but a later sea ice retreat (Table 2 and Fig. 3). Sea ice cleared the region rapidly in 2017, dropping from 52% coverage in November, to 12% in December, and 3% in January (Fig. 3). In 2018, the sea ice retreated earlier but coverage stayed higher in the region into the summer, with 24% coverage in November, 17% coverage in December, and 10% coverage in January (Fig. 3).

## 2.5 Discussion

### 2.5.1 *Model development: successes and challenges*

Overall, we achieved the goal of our study: to create a CNN to accurately sort WAP phytoplankton into taxonomic categories. Our overall model achieved an f1-score of 93.7% with an increase to 96.5% for merged taxonomic groupings. This indicates that our phytoplankton imagery data can be successfully and accurately sorted with machine learning techniques, greatly reducing the time spent classifying these images manually. Absolute comparisons to classification algorithms from previous studies is challenging given different numbers of classes, data filtering schemes, and methods for determining what constitutes test data, but in general these metrics compare very favorably to other

models. The development of regional and global phytoplankton classifying CNNs presents an opportunity to greatly advance our understanding of plankton diversity and ecology.

However, our model f1-score dropped dramatically from 93.7% during model development to 46.5% during model validation on a new, random dataset with a class distribution representative of that found in natural waters. We believe that this large decrease in model accuracy is a key challenge rarely addressed in the literature. One reason for this decrease is the highly imbalanced class distributions of naturally occurring phytoplankton assemblages compared to our model testing dataset (e.g., see  $n$  values in Table 1). Model categories such as detritus are highly abundant in our dataset, often composing up to 50% of the biovolume in a sample, while other ecologically important groups, such as large, morphologically distinct diatoms including *Corethron penatum* and *Eucampia antarctica* are encountered sporadically in our dataset. A minor misclassification of detritus as a rare class can easily overwhelm that category.

Nearly all previous studies report accuracy for a balanced and curated test dataset rather than a random sample of natural waters. During model development a balanced class distribution is necessary to ensure the model equally weights each category during training. For example, if during model development a single class composed 90% of the training dataset, the model could classify every sample as that class, ignoring all others, and be 90% accurate. The gradient descent optimization algorithm would never learn any other classes. In the few studies that do report accuracy in natural samples, our drop-off is similar (See Table 2 in (Sosik and Olson 2007)).

The classes being naturally highly imbalanced creates several model development choices, including whether to exclude, up-sample, or augment low incidence classes, and

how specific model classifications should be (e.g., high level classes like diatoms, dinoflagellates, etc. or species level classes like *Thalassiosira* and *Gyrodinium*). We tried to strike a balance in our model setup by eliminating rare classes or merging them into broader groups while keeping groups morphologically distinct to prevent model confusion. However, there remains a degree of high intraclass variance and interclass similarity in morphology that was impossible to eliminate (e.g., 14.9% classification accuracy for “other”; Table 1). This challenge can be addressed on the other end of model development, by filtering samples where model uncertainty is high. The CNN outputs a confidence score (from the Softmax classification layer) for each prediction from 0 to 1 that can be used to filter samples below a certain threshold. While potentially increasing the model accuracy, this could also bias the system against certain classes that are challenging to classify, and thus was not implemented in this work.

Another potential cause of reduced model accuracy is data labelling errors. Theoretically, manual identification of images should be close to perfect, but unfortunately this is not the case. In this work and most others, there is often a bias for training and test data that is easily identifiable by manual validation, which prevents test metrics from translating exactly to the wild. There are also many images with conglomerations of cells including detritus and multiple living species. While these may be manually sorted into a category labelled “multiple” and discarded from the analysis, a CNN might sort these images into the most prominent class present within each image. Additionally, morphologically ambiguous cells may be sorted more accurately by a CNN than by manual identification, as a CNN can mathematically match image attributes to potential groups. One way we attempted to eliminate a portion of these ambiguous cells

was to exclude all cells with a major axis length less than 25 pixels (7.35  $\mu\text{m}$ ) prior to model training. These small cells are below the quantifiable limit of detection based on instrument resolution, and thus have a high probability of being incorrectly identified. Accurately classifying these smaller cells will likely require techniques other than imaging. The issues of class imbalance can also magnify labelling errors, especially when these errors are within abundant classes such as “detritus”.

### 2.5.2 *Phytoplankton seasonal succession at Palmer Station*

Like other studies, we found that following a winter with low sea ice (2017), the phytoplankton community had less diatoms, and more mixed flagellates and cryptophytes, and following a winter with high sea ice (2018), the community was dominated by diatoms (Figs. 1, 3, Table 2) (Saba et al. 2014; Schofield et al. 2017). Following trends found in previous years at Palmer Station (Schofield et al. 2017), we also saw diatoms dominate in the late spring and early autumn, and higher cryptophyte concentrations in peak summer (December and January).

Along the WAP, phytoplankton show strong interannual and regional variability timed with light availability and sea ice retreat. As day length increases in austral spring, solar warming and sea ice melt stabilize the upper water column allowing phytoplankton to remain near the surface in waters with high light availability [18-19]. These conditions initiate large diatom-dominated spring blooms, as we saw in 2018 [20-21]. In 2017, there was 52% sea ice coverage in November, likely inhibiting light penetration and subsequent phytoplankton growth. Dramatic reduction in sea ice coverage between November and December indicates that the ice was rapidly advected out of the region, reducing sea ice

melt near Palmer Station and potentially reducing the stability of the upper mixed layer. In 2018, although sea ice retreat is six days later than in 2017, November sea ice coverage is only 24%, allowing adequate light for phytoplankton growth. Additionally, the sea ice lingers into December and January (17% and 10%, respectively), providing a stable environment for growth well into the summer. Matching our results, (Annett et al. 2010) found that rapid sea ice retreat was associated with lower proportions of centric diatoms during the spring in Ryder Bay, Antarctica (Fig. 2). Sea ice can also hold populations of ice algae, which can seed coastal regions during melting in spring (Ackley and Sullivan 1994). It is possible that with rapid sea ice advection from the region in 2017, less ice algae were released to the coastal region near Palmer Station than in 2018 when sea ice lingered and contributed more meltwater.

Despite differences in phytoplankton abundance and community structure between the two years, there were similar trends in the diatom community. Late spring was dominated by large centric diatoms  $> 20 \mu\text{m}$  timed with sea ice retreat as described above. Progressing towards autumn, centric diatoms became smaller ( $< 20 \mu\text{m}$ ), and the abundance of pennate diatoms  $< 10 \mu\text{m}$  increased (Fig. 3). A explanation for this size shift is the increasing amount of glacial meltwater from January to March (Meredith et al. 2021). Stronger surface stratification due to increased ice melt can reduce nutrients in surface waters, giving an advantage to smaller phytoplankton with high surface-area-to-volume ratios and reduced sinking rates (Li et al. 2009). Additionally, (Hernando et al. 2015) experimentally exposed phytoplankton populations from Potter Cove, Antarctica to low salinity conditions (30 PSU) and found a decline in the abundance of large centric diatoms from  $\sim 90\%$  on day 2 to  $\sim 0\%$  on day 7, and an increase in abundance of small

pennate diatoms from ~0% on day 4 to ~95% on day 8. They attribute these changes to differing osmotic stress tolerances: in large centric diatoms, a decrease in salinity caused increases in individual cell size, compression of chloroplasts, granularization of the protoplasm, and retraction of the cytoplasm, while some small pennate diatoms (e.g., *Fragiliariopsis cylindrus*) may contain genes beneficial for adaptation to extreme environmental conditions in polar oceans and sea ice. Thus, increases in glacial meltwater in late summer could cause diatom communities to become smaller and increasingly dominated by pennate cells as we observed.

### 2.5.3 *Conclusions and next steps*

Our CNN is a step forward for understanding phytoplankton ecology along the WAP. However, there are still improvements to be made before it becomes a long-term tool for the community. As explained above, an important issue to address is class imbalance compounded with labelling errors of abundant classes. One potential way to better represent these undifferentiated classes (e.g., “detritus” or “multiple”) is to use unsupervised methods (e.g., non-linear dimensionality reduction, clustering, and manifold learning) to break these classes into several new groups. Defining classes purely via data rather than taxonomy could help models with potentially more easily separable decision boundaries. These techniques could also reduce manually labeled training data needs with semi-supervised classification, and in many cases unsupervised techniques may be sufficient for answering questions about phytoplankton dynamics without any need for supervised classification (Culhane et al. 2020). Another method could be to use a stage-wise approach, with a one-class-classifier or binary classification to exclude “detritus” and

“multiple” images up front to limit the spread of these issues into the full output range which is exacerbated by the prevalence of these classes. In tandem to improving the classification itself, per class uncertainty estimates (sensu (Sosik and Olson 2007)) will be critical to unbiased extrapolation from CNN output to ecological dynamics.

With further increases in model accuracy, we hope our model will become a helpful tool for phytoplankton research. Long-term warming and sea ice declines along the WAP are contributing to shifts to smaller and less abundant phytoplankton populations (Montes-Hugo et al. 2009), and these trends are likely to continue. Understanding the seasonal and spatial dynamics of phytoplankton diversity is integral to contextualizing how communities will change in the future. Beyond the CNN’s ability to rapidly classify entire seasons of collected phytoplankton imagery, it can also be used to characterize phytoplankton communities in near-real time. Getting a snapshot of species and cell size dynamics soon after collecting a sample would aid in opportunistic sampling while still in the field. This would be invaluable, as research time in Antarctica is both limited and expensive.

Lastly, the PAL-LTER is not the only group experiencing these challenges: there is a broad IFCB user community searching for methods to automate sample classification to reduce the need for manual image validation. Various groups are independently creating phytoplankton CNNs and other models for their study sites of interest. We implore the community to begin reporting their model metrics on data with distributions representative of the natural environment, sharing labeled data openly on freely accessible platforms (e.g., EcoTaxa, IFCB Dashboard), and sharing open and reproducible code for processing and model development. As models improve, the community may be able to develop a

series of regional models, freely available to download and classify a worker's data, or even a single generalizable model usable for the world oceans. Moving forward towards this vision, it will be critical for oceanographers to collaborate with computer scientists and modelers, incorporating the best computer vision and classification techniques to these datasets ultimately to better understand phytoplankton dynamics in a changing ocean.

## **2.6 Acknowledgments**

This work was supported by the National Science Foundation Antarctic Organisms and Ecosystems Program (PLR-1440435) as part of the PAL-LTER program. Thank you to Alison Chase and Sasha Kramer for help with taxonomic identifications, and to Emmett Culhane for helpful discussions regarding the challenges of building a CNN for IFCB data. This work would not be possible without the PAL-LTER field teams who aided in data collection and the Palmer Station and Laurence M. Gould personnel who provided logistical support.

## 2.7 Tables

**Table 1.** Confusion matrix for broad taxonomic groups using 10,269 new, random images.

True label	<b>Pennate diatoms</b> ( <i>n</i> =1577)	<b>92.9</b>	0.8	0.3	0.6	4.8	0.0	0.0	0.7
	<b>Centric diatoms</b> ( <i>n</i> =249)	2.8	<b>64.3</b>	5.2	2.4	15.3	0.0	0.0	10.0
	<b>Cryptophytes</b> ( <i>n</i> =2565)	9.4	1.0	<b>65.0</b>	4.4	19.8	0.0	0.0	0.5
	<b>Prasinophytes</b> ( <i>n</i> =493)	2.6	1.6	0.4	<b>39.6</b>	28.0	0.0	0.0	27.8
	<b>Mixed flagellates</b> ( <i>n</i> =1085)	11.6	1.5	3.9	7.4	<b>66.2</b>	0.0	0.3	9.2
	<b>Haptophytes</b> ( <i>n</i> =1)	0.0	0.0	0.0	0.0	0.0	<b>100</b>	0.0	0.0
	<b>Microzooplankton</b> ( <i>n</i> =6)	0.0	16.7	0.0	0.0	16.7	0.0	<b>66.7</b>	0.0
	<b>Other</b> ( <i>n</i> =3475)	26.9	10.9	4.9	18.4	23.8	0.0	0.3	<b>14.9</b>
		<b>Pennate diatoms</b> ( <i>n</i> =2788)	<b>Centric diatoms</b> ( <i>n</i> =601)	<b>Cryptophytes</b> ( <i>n</i> =1898)	<b>Prasinophytes</b> ( <i>n</i> =1040)	<b>Mixed flagellates</b> ( <i>n</i> =2304)	<b>Haptophytes</b> ( <i>n</i> =1)	<b>Microzooplankton</b> ( <i>n</i> =16)	<b>Other</b> ( <i>n</i> =803)
		<b>Predicted label</b>							

**Table 2.** Sea ice characterization.

<b>Year</b>	<b>Sea Ice Duration (days)</b>	<b>Date of Sea Ice Retreat</b>
2017	132	December 3
2018	153	November 27

## 2.8 Figures

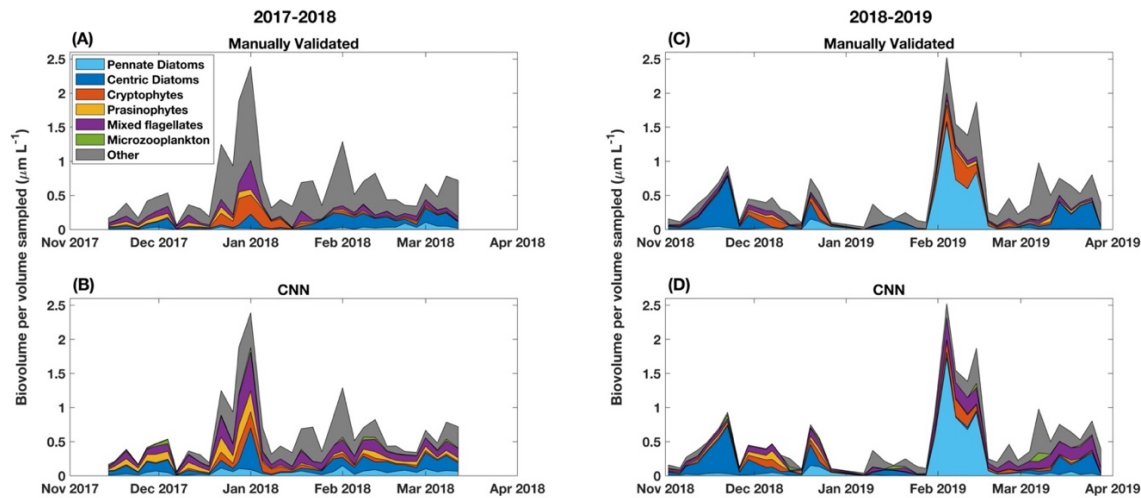


**Figure 1.** Methods comparison of phytoplankton seasonal succession for the (A-B) 2017-2018 and (C-D) 2018-2019 summer field seasons, showing biovolume data from (A and C) manual validation and (B and D) CNN predictions.

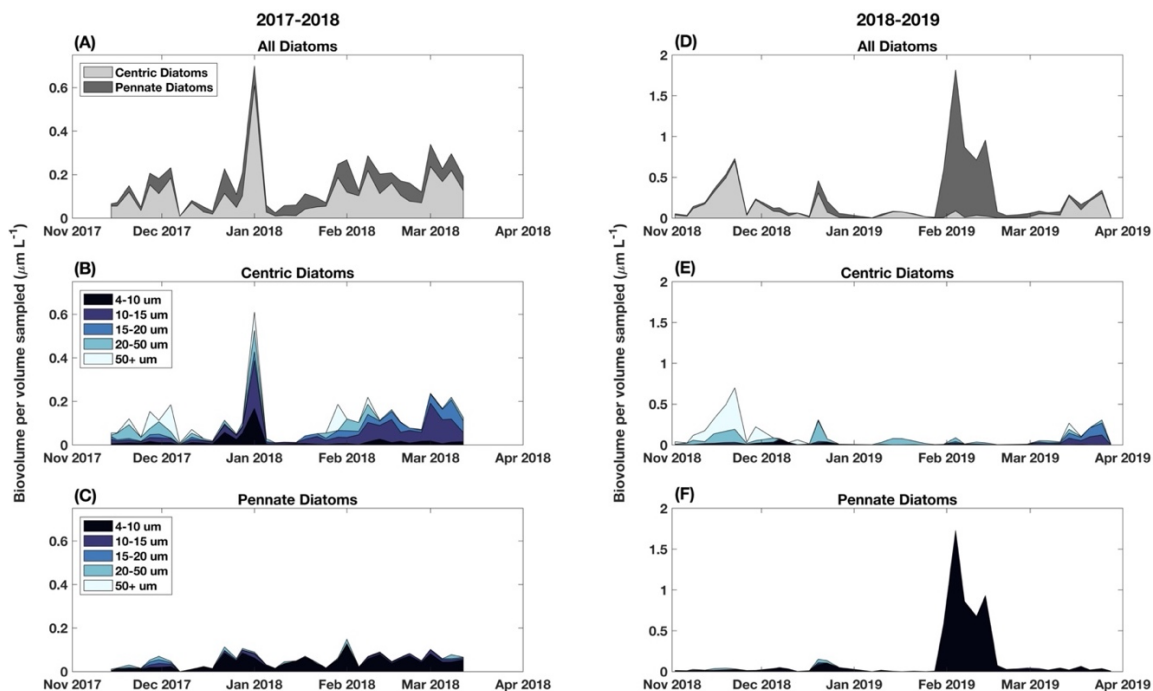


**Figure 2.** Diatom seasonal diversity as predicted with the CNN for the (A-C) 2017-2018 and (D-F) 2018-2019 summer field seasons. (A and D) Total biovolume attributed to pennate and centric diatoms. (B and E) Total biovolume attributed to different size classes of centric diatoms. (C and F) Total biovolume attributed to different size classes of pennate diatoms.

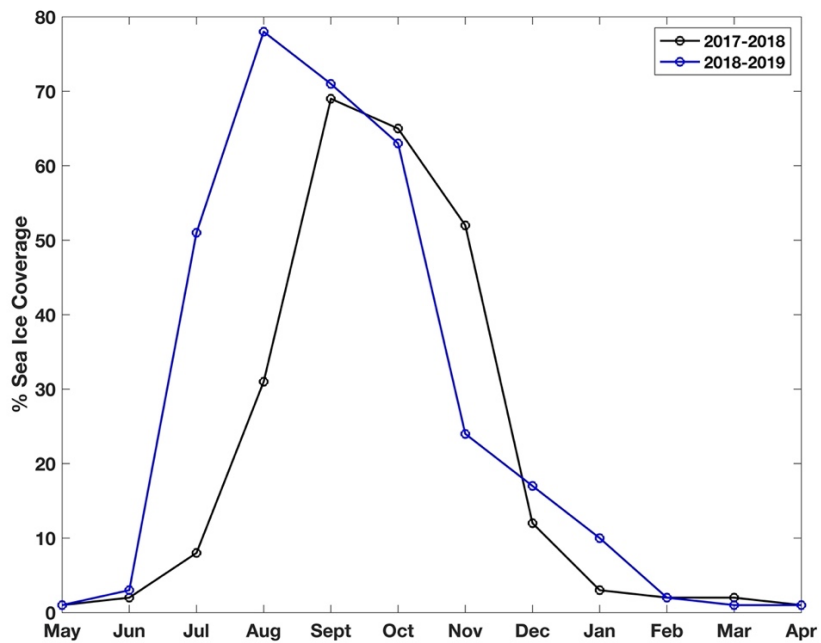


**Figure 3.** Percent sea ice coverage in the 200 km area south and west of Palmer Station during the 2017-2018 season (black) and the 2018-2019 season (blue).

### **3. Coastal phytoplankton seasonal succession and diversity on the West Antarctic Peninsula**

#### **3.1 Abstract**

In coastal West Antarctic Peninsula (WAP) waters, large phytoplankton blooms in late austral spring fuel a highly productive marine ecosystem. However, WAP atmospheric and oceanic temperatures are rising, winter sea ice extent and duration are decreasing, and phytoplankton biomass in the northern WAP has decreased and shifted towards smaller cells. To better understand these relationships, an Imaging FlowCytobot was used to characterize seasonal (November to March) phytoplankton community composition and cell size during a low (2017-2018) and high (2018-2019) chlorophyll year in relation to physical drivers (e.g., sea ice and glacial meltwater) at Palmer Station, Antarctica. A shorter sea ice season with early rapid spring retreat resulted in low phytoplankton biomass with a low proportion of diatoms (2017-2018), while a longer sea ice season with late protracted spring retreat resulted in the opposite (2018-2019). Despite these differences, phytoplankton seasonal succession was similar in both years: (1) a large-celled centric diatom bloom during spring sea ice retreat; (2) a peak-summer phase to mixotrophic cryptophytes with increases in light and post-bloom organic matter; and (3) a late-summer phase to small ( $< 20 \mu\text{m}$ ) diatoms and mixed flagellates with increases in wind-driven nutrient resuspension. Additionally, cell diameter decreased through both seasons with increases in meteoric meltwater input. The tight coupling between sea ice, meltwater, and phytoplankton species composition suggests that continued warming in the WAP will affect phytoplankton seasonal dynamics which will impact seasonal food web dynamics.

### 3.2 Introduction

Coastal waters along the West Antarctic Peninsula (WAP) host a highly productive, ice-dependent marine ecosystem fueled by large, seasonal phytoplankton blooms reaching concentrations  $> 20 \text{ mg chlorophyll-}a \text{ m}^{-3}$  (Vernet et al. 2008; Ducklow et al. 2013; Kim et al. 2018). Average primary productivity in the WAP is  $\sim 182 \text{ g C m}^{-2} \text{ y}^{-1}$ , which is similar to other continental shelf areas in Antarctica (Arrigo et al. 2008), but four times lower than other productive coastal regions in the world's oceans (Vernet and Smith 2006). WAP phytoplankton blooms initiate in the austral spring when increased solar irradiance alleviates light limitation, and sea ice melt stratifies the upper water column and confines phytoplankton in well-lit surface waters (Vernet et al. 2008; Venables et al. 2013). Macronutrients and micronutrients are generally replete in the nearshore coastal WAP waters (Ducklow et al. 2012; Kim et al. 2016; Sherrell et al. 2018; Carvalho et al. 2019), thus upper water column stratification is considered the primary driver of phytoplankton productivity (Garibotti et al. 2005; Vernet et al. 2008; Carvalho et al. 2019). Seasonal phytoplankton dynamics are tightly coupled to krill recruitment (Saba et al. 2014), and krill in turn are the main food source for penguins, seals, whales, and other predators (Pikitch et al. 2014), suggesting a strong bottom-up control of the ecosystem. Thus, studying how coastal phytoplankton communities respond to physical drivers is imperative for understanding ecosystem structure and function.

The coastal WAP phytoplankton community is comprised of diatoms, cryptophytes, mixed flagellates, prasinophytes, and haptophytes, with diatoms making up the highest percentage of annual biomass (Garibotti et al. 2005; Gonçalves-Araujo et al.

2015; Schofield et al. 2017). However, different phytoplankton species require specific abiotic conditions for optimal growth, causing both seasonal and interannual variability in species composition. Earlier studies have tried to reconstruct seasonal succession along the WAP (Garibotti et al. 2005; Schofield et al. 2017; van Leeuwe et al. 2019); however, validation of these hypotheses is still an open question as the results are largely based on phytoplankton accessory pigments which are only capable of resolving general taxa. In general, there are three phases of phytoplankton seasonal succession from austral spring to autumn in the coastal WAP: (1) a diatom-dominated bloom comprised primarily of large centric diatoms associated with sea ice retreat and upper water column stratification in November/December, (2) a cryptophyte-dominated community associated with low chlorophyll-*a*, decreased nutrient stocks, and shallow mixed layer depths (MLD) in December/January, and (3) a diatom-enriched assemblage associated with low chlorophyll-*a* including small diatoms, haptophytes, and unidentified flagellates in February/March (Garibotti et al. 2005; Schofield et al. 2017; van Leeuwe et al. 2019).

The productive WAP ecosystem is being subject to significant environmental change. One of the fastest warming regions on Earth, WAP winter air temperatures and surface ocean temperatures have increased by 6°C and >1°C, respectively, since 1951 (Meredith and King 2005; Turner et al. 2005). In response, 90% of marine glaciers were in retreat as of 2016, the annual ice season has decreased by > 92 days since 1979, and there is no longer perennial sea ice in the northern WAP (Stammerjohn et al. 2012; Cook et al. 2016). Ocean warming, sea ice and glacial retreat, and glacial melt have in turn impacted the phytoplankton community, with significant decreases in mean phytoplankton biomass in January along the northern WAP associated with a shift from large (> 20 µm) to small-

celled ( $< 20 \mu\text{m}$ ) phytoplankton (Montes-Hugo et al. 2009). It is hypothesized that this size shift is driven by increasing cryptophyte (cell diameters of  $\sim 6.5\text{-}9 \mu\text{m}$ ) abundance in coastal regions that are often associated with low salinity meltwater (Moline et al. 2004; Mendes et al. 2013; Schofield et al. 2017). The reasons why cryptophytes might outcompete diatoms in low-salinity waters are not well understood, but are hypothesized to be related to an advanced light-adaptation system that allows them to thrive in stratified surface waters with high irradiances (Kaňa et al. 2012; Mendes et al. 2017). The increased spatial extent of low salinity surface waters is predicted to increase the prevalence of smaller-celled phytoplankton communities along the WAP (Moline et al. 2004), with important implications for food web structure and trophic energy transfer efficiency (Sailley et al. 2013).

The Palmer Long-Term Ecological Research Project (PAL-LTER) was established in 1991 to investigate how warming and sea ice loss will change the structure of the pelagic ecosystem and biogeochemistry along the WAP. The project has previously used High Performance Liquid Chromatography (HPLC) analysis of pigment data to characterize the taxonomic composition of phytoplankton assemblages (e.g., Schofield et al. 2017). This technique uses marker pigments of phytoplankton groups to assess their contribution to the overall abundance. Few studies have looked at higher taxonomic resolution and cell size distributions over seasonal scales along the WAP.

Our study utilized an imaging-in-flow cytometer to characterize seasonal and interannual phytoplankton diversity at Palmer Station, Antarctica, with a focus on local sea ice and meltwater impacts. We sampled during a high and low chlorophyll year to investigate (1) interannual differences in the physical environment and corresponding

differences in phytoplankton communities, and (2) potential mechanisms driving phytoplankton seasonal succession between years. Results showed that despite significant differences in sea ice dynamics and phytoplankton biomass between years, there were consistent seasonal succession patterns that matched the broader successional framework developed by Behrenfeld et al. (2021), which is an updated version of Margalef (1978)'s original mandala that incorporates phytoplankton cell size, division rates, and loss rates. Additionally, environmental disturbances (e.g., spring sea ice retreat, wind-driven mixing, glacial and sea ice melt) throughout the season drove changes in phytoplankton community composition that could not be described using HPLC alone. These findings provide insights into regulation of seasonal phytoplankton dynamics and help us hypothesize how ongoing warming and melting along the WAP might impact future coastal phytoplankton communities.

### **3.3 Methods**

#### *3.3.1 Sample collection*

Annual sample collection at Palmer Station, Antarctica (Fig. 1) has been conducted by the PAL-LTER since 1991 at two locations: an inshore station (B, bottom depth of ~75 m) and an offshore station (E; bottom depth of ~200 m). These stations are sampled twice a week from when the sea ice breaks out (~ mid-October/November) to late March. Inclement weather and heavy sea ice can limit sampling in this region, leading to occasional gaps in the dataset.

For this study, we focused on two summer field seasons: 2017-2018 (16 November to 26 March), which had lower than average chlorophyll-*a* and shorter than

average winter sea ice duration, and 2018-2019 (2 November to 28 March), which had higher than average chlorophyll-*a* and longer than average winter sea ice duration (Fig. 2). Because our study focused on the impacts of meltwater on inshore phytoplankton communities, our analysis exclusively used surface samples from Station B, which is adjacent to the Marr Glacier (Fig. 1).

For each sampling event, a SeaBird Electronics Seacat SBE 19plus sensor (measuring salinity, temperature, depth) was profiled down to 60 m. These data were averaged into 1-m depth bins. In addition, surface seawater samples were collected with a 4 L niskin bottle and stored in a cold, dark environment until sample processing on return to Palmer Station.

### 3.3.2 *Phytoplankton pigment analysis*

Concentrations of chlorophyll-*a* and accessory pigments were measured via HPLC. 1-2 L of whole seawater was filtered onto GF/F filters (pore size = 0.7  $\mu\text{m}$ , diameter = 25 mm), flash-frozen in liquid nitrogen, and stored at  $-80^{\circ}\text{C}$  for post-season analysis. The samples were shipped to Rutgers University (New Brunswick, NJ), where they were extracted in 90% methanol and 2% aqueous ammonium acetate, ultrasonicated for 30 sec (while kept cold in ice water), stored at  $-20^{\circ}\text{C}$  for at least 2 h, ultrasonicated again for 10 sec, and then centrifuged to separate the extract from the filter. The extract was run on the HPLC system (Agilent 1100/1200 series with a Diode Array Detector (Model G1315C, scanning wavelengths 275-800 nm) and a Zorbax Eclipse Plus C18 column, 4.6 x 250 mm, 5  $\mu\text{m}$ ) to separate the pigments. HPLC Grade phase eluents were used following Wright et al. (1991): Solvent A = 80% methanol and 20% aqueous

ammonium acetate with pH = 7.2; Solvent B = 90% acetonitrile and 10% water; and Solvent C = 100% ethyl acetate. Agilent software quantified peaks at 440 nm and identified pigments based on retention time and spectral shape. These values were manually checked and any mistakes corrected. Using the output HPLC pigment data, phytoplankton taxonomic composition was quantitatively determined in CHEMTAX V1.95 using pigment ratios derived from WAP phytoplankton (Kozłowski et al. 2011). Output phytoplankton groups include diatoms, cryptophytes, prasinophytes, haptophytes and mixed flagellates (including both dinoflagellates and other phytoflagellates).

### 3.3.3 *Phytoplankton species and size analysis*

For species identification and cell size distributions, 5 mL of each surface sample was analyzed with an Imaging FlowCytobot (IFCB; McLane Labs, Falmouth, MA, USA). The IFCB is an imaging-in-flow cytometer that uses a combination of video and flow cytometric technology to collect images and measure chlorophyll fluorescence and scattered light for each particle (~10-150  $\mu\text{m}$ ) in each water sample (Olson and Sosik 2007). Samples were passed through a 150  $\mu\text{m}$  Nitrex screen prior to analysis to prevent large cells from clogging the IFCB's flow cell. Cells with major axis length < 20 pixels (5.88  $\mu\text{m}$ ) were eliminated from the analysis as the resolution of the images was insufficient to provide clear identification.

Images were extracted from IFCB files and processed using methods and software from Sosik and Olson (2007; <https://github.com/hsosik/ifcb-analysis/wiki>). Image processing results in a set of 233 features describing each image including equivalent spherical diameter, area, and biovolume of each cell. Processed images were then sorted

into 40 taxonomic groups using a medium complexity convolutional neural network (~2,000,000 parameters) that was created and validated using WAP phytoplankton (Nardelli et al. 2021; [https://github.com/patrickcgray/deep\\_ifcb](https://github.com/patrickcgray/deep_ifcb)). Processed images, along with their predicted identifications, associated features, and metadata were uploaded to the web application EcoTaxa (Picheral et al. 2017; <https://ecotaxa.obs-vlfr.fr>), where predicted images were manually validated or resorted into their correct taxonomic group.

Identification of individual cells was performed to the lowest possible taxonomic level, e.g., most diatoms were identified to species level and most phytoflagellates were identified to class level (cryptophyte, prymnesiophyte, and prasinophyte; see Table 1), with guidance from Hasle et al. (1997) and Scott et al. (2005). Mixed flagellates included dinoflagellates (e.g., *Gymnodinium spp.*, *Gyrodinium spp.* and others), silicoflagellates (e.g., *Dictyochales spp.*), and other unidentified phytoflagellates. Prasinophytes primarily included *Pyramimonas spp.* and *Pterosperma spp.*, and haptophytes primarily included *Phaeocystis antarctica*. Diatoms were divided into centric and pennate groups (see Table 1). Unidentified centric discoid cells included *Thalassiosira spp.*, *Coscinodiscus spp.*, *Minidiscus chilensis*, *Porosira spp.*, *Actinocyclus actinochilus*, *Asteromphalus hookeri*, and *Stellarima microtrias*, among others. Unidentified pennate cells included *Banquisia belgicae*, *Membraneis spp.*, *Navicula spp.*, *Fragilariopsis spp.*, and *Nitzschia spp.*, among others. Chains of unidentified centric and pennate diatom species were included in the > 20  $\mu\text{m}$  category.

In addition, aggregated metrics for all phytoplankton cells and for the six broad taxonomic groups (centric diatoms, pennate diatoms, cryptophytes, mixed flagellates,

haptophytes, and prasinophytes) were calculated for each sample. These include total biovolume (sum of biovolume of all cells in a sample divided by the mL of water sampled), total abundance (number of all cells in a sample, divided by the mL of water sampled), and median cell diameter.

Since IFCB-derived phytoplankton cell biovolume and HPLC-derived chlorophyll-*a* concentrations were both estimates of total phytoplankton biomass for each method, we compared the two using Kendall rank correlation to confirm general agreement. To validate taxonomic precision, IFCB data were separated into broad taxonomic groups matching those derived from HPLC (diatoms, cryptophytes, prasinophytes, haptophytes, mixed flagellates). Then, the methods were compared for each taxonomic group by evaluating the Kendall rank correlation between percent taxa in each sample for both methods.

In both years, preserved samples (5 mL whole seawater in 50% glutaraldehyde) were collected during times when the IFCB was not available (i.e., undergoing maintenance or aboard the vessel on the annual 1-month WAP cruise). Fixed samples were flash-frozen in liquid nitrogen and stored at -80°C for post-season analysis. In 2017-2018, samples were preserved from 5 January to 5 February, and in 2018-2019, samples were preserved on 13 December and from 7 January to 28 March. On 22, 26, and 28 December 2017, live samples were collected alongside preserved samples. On average, total biovolume and cell abundance of preserved samples were underestimated by 48.07% and 36.36%, respectively, when compared to live samples (Supplementary Fig. 1A-B). However, changes in the relative magnitudes between the three samples is similar (Supplementary Fig. 1A-B), as are the taxonomic proportions of different taxa groups

(Supplementary Fig. 1C-E). Cryptophytes and prasinophytes were consistently found at higher percentages in preserved versus live samples, indicating a potential preservation bias towards these groups (on average 17.38% more cryptophytes and 32.86% more prasinophytes in preserved samples; Supplementary Fig. 1C-E).

To quantify phytoplankton diversity from IFCB data, the Shannon diversity index ( $H$ ) was used, which describes the number and richness of groups sampled:

$$H = - \sum_{i=1}^R p_i \ln p_i$$

Where  $p_i$  is the proportion of individuals in the  $i$ th group identified in the data set and  $R$  is the total number of groups identified in the data set. Higher values of  $H$  suggest that there are both more groups represented in the data set and more members of each of those groups. An  $H$  value of zero indicates only one group present in the data set.

#### 3.3.4 *Defining phytoplankton seasonal succession phases*

Seasonal succession phases were defined using relative species compositions from IFCB data. Data were divided into phases following those hypothesized in Garibotti et al. (2005). The first successional phase (“Ice Retreat Phase”) was a diatom bloom associated with the sea-ice edge. The start of the Ice Retreat Phase was defined as the first sampling day of the season, occurring just as sea ice began to break up to allow small boat activity. The second successional phase (“Peak Summer Phase”) was an assemblage dominated by cryptophytes. The start of the Peak Summer Phase was defined as the first of three consecutive sampling days when cryptophyte percent composition rose above 15% and ends once cryptophyte composition drops back below 15% for three

consecutive sampling days (Supplementary Fig. 2). A threshold of three sampling days was chosen to confirm the composition shift was steady and not driven by variability within a given week. The third successional bloom phase (“Late Summer Phase”) was a diatom-rich assemblage in ice-free conditions. The Late Summer Phase begins when the Peak Summer Phase ends and corresponds to a rise in diatom percent composition to the highest values of the season (Supplementary Fig. 2). In 2018-2019, however, there is a fourth successional phase (“Late Summer Phase B”) characterized by an initial drop in diatom percent composition below 35% and a simultaneous increase in mixed flagellate percent composition above 30%, after which diatom percent composition increased again (Supplementary Fig. 2).

### 3.3.5 *Nutrient analyses*

Surface samples were analyzed for nitrate plus nitrite ( $\text{NO}_3^- + \text{NO}_2^-$ ; hereafter called nitrate due to the very low concentration of nitrite), phosphate ( $\text{PO}_4^{3-}$ ), and silicate ( $\text{Si}(\text{OH})_4^-$ ) following methods from The Joint Global Ocean Flux Study (1994). 1 L from each surface sample was filtered through GF/F filters (pore size = 0.7  $\mu\text{m}$ , diameter = 25 mm) and stored at  $-20^\circ\text{C}$  in 15 mL acid-rinsed Falcon centrifuge tubes for post-season analysis. The samples were shipped to Lamont Doherty Earth Observatory at Columbia University (New York, NY), where they were analyzed using a SEAL Analytical AutoAnalyzer AA3 HR, Software version 6.10 (Mequon, WI), G-297-03 Rev 4 (Multitest MT19 for phosphate), G-172-96 Rev 16 (Multitest MT 19 for nitrate), and G-177-96 Rev 11 (Multitest MT19 for silicate), using the following standards: potassium

dihydrogen phosphate for phosphate, potassium nitrate and sodium nitrite for nitrate, and sodium metasilicate nonahydrate for silicate analyses.

### 3.3.6 *Meltwater composition*

Water from each surface sample was drawn into 50 mL glass vials, sealed with stoppers and aluminum crimps, and stored in a dark, +4°C box. Samples were transported to the National Environmental Isotope Facility at the British Geological Survey (Keyworth, Nottinghamshire, UK). There, an Isoprime 100 mass spectrometer plus Aquaprep device were used to analyze oxygen isotope composition ( $\delta^{18}\text{O}$ ) using the  $\text{CO}_2$  equilibration method. Measurements were calibrated against the internal and international standards (e.g., VSMOW2 and VSLAP2). An analytical reproducibility of +/- 0.02‰ was obtained with duplicate analysis.

Using  $\delta^{18}\text{O}$  and surface salinity data, we quantitatively separated sea ice melt from meteoric water (glacial melt and precipitation) by solving a three-endmember mass balance equation (see methods in Meredith et al. (2021); endmember values are listed in their Table 1). Using this mass balance equation, negative values for sea ice melt are possible and are indicative of net sea ice formation from the preceding winter.

### 3.3.7 *Water column stability*

Mixed layer depths could not be confidently predicted ( $\text{QI} < 0.5$ ; Lorbacher et al. 2006) at Station B due to the shallow water depth (~60 m). Thus, average Brunt–Väisälä Frequency ( $N^2$ ) values were calculated for the top 25 m using methods from Carvalho et

al. (2017) to quantify and compare upper water-column stability within and between our two sampling seasons.

### 3.3.8 *Weather data*

Wind speed ( $\text{m s}^{-1}$ ; RM Young, Model 05108-45) and photosynthetically active radiation ( $\mu\text{mol sec}^{-1} \text{m}^{-2}$ ; Licor, Model LI 190) measurements were obtained from an automated weather station located just behind Palmer Station. 5-day averages of wind speed (current day and the 4 previous days) and daily-averaged PAR were calculated from 2-minute data.

### 3.3.9 *Sea ice data*

Sea ice metrics were calculated from satellite-derived daily sea ice concentration (%) data determined using the GSFC Bootstrap algorithm version 3.1 and extracted for the 25 km x 25 km satellite pixel closest to Palmer Station. Following methods in Stammerjohn et al. (2008), day of ice-edge advance was calculated as the first day when sea ice concentration exceeded a 15% threshold for at least 5 consecutive days; day of ice-edge retreat was calculated as the last day before sea ice concentration dropped below a 15% threshold after being above 15% for at least 5 consecutive days; sea ice duration is the number of days between the day of advance and the day of retreat, and number of sea ice days are the number of days between the day of advance and day of retreat where sea ice concentration is  $>15\%$ .

### 3.3.10 Statistical analyses

To assess interannual differences, one-way ANOVAs with Kruskal-Wallis post-hoc tests were conducted for each environmental variable (sea ice concentration, PAR, surface temperature, surface salinity, percent meteoric meltwater, percent sea ice meltwater,  $N^2$ , wind speed, nitrate, phosphate, and silicate) and phytoplankton variable (chlorophyll-*a* concentration, H, and IFCB-derived phytoplankton biovolume, abundance, and median diameter), to determine whether values were significantly different between the two field seasons. To assess relationships between environmental and phytoplankton variables within each season, Kendall rank correlation tests were used. Non-parametric statistics were used due to the non-normal data distributions for most variables.

## 3.4 Results

### 3.4.1 HPLC versus IFCB taxonomy comparison

HPLC-derived chlorophyll-*a* concentrations were significantly positively correlated to IFCB-derived biovolume concentrations (Kendall  $p = 1.5 \times 10^{-9}$ ,  $\tau = 0.47$ ; Supplementary Fig. 3). Peaks in biomass were generally similar relative to other peaks within each season between the two methods, with notable differences including much lower peaks for IFCB-derived biovolume on 19 November 2018 and 21 January 2019 compared to HPLC-derived chlorophyll-*a* (Fig. 3).

Additionally, there were significant, positive correlations between percent taxa calculated with each method for diatoms, cryptophytes, prasinophytes, and mixed flagellates (Kendall  $p < 0.0001$ ,  $\tau = 0.34-0.52$ ; Supplementary Fig. 4A-D), and a non-

significant, positive correlation for haptophytes (Kendall  $p = 0.49$ ,  $\tau = 0.05$ ; Supplementary Fig. 4E). Despite a significant positive correlation, IFCB classification overpredicted mixed flagellates compared to HPLC classification, illustrated by the skew of points above the 1:1 line in Supplementary Fig. 4D, and by the greater annual total percent of mixed flagellates using IFCB classification compared to HPLC classification (by 23% in 2017-2018 and by 7% in 2018-2019; Fig. 3). Similarly, IFCB classification underpredicted diatoms compared to HPLC classification, illustrated by the skew of points below the 1:1 line in Supplementary Fig. 4A, and by the lesser annual total percent of IFCB-classified diatoms compared to HPLC-classified diatoms (by 24% difference in 2017-2018 and by 8% difference in 2018-2019; Fig. 3). Despite discrepancies between methods, IFCB data provided information that HPLC data could not, including cell size and species composition within taxonomic groups (Table 1).

### 3.4.2 *Interannual differences*

Compared to the winter of 2018, the winter of 2017 had a later autumn sea ice advance date (16 day difference), an earlier spring sea ice retreat date (24 day difference), shorter sea ice duration (40 day difference), and less total ice days (52 day difference; Table 2, Fig. 4A-B). Sea ice was rapidly advected from the region in 2017, dropping from 49% on 27 November to 0% on 3 December (Fig. 4A). In 2018, there was an initial drop in sea ice concentration from 96% on 2 November to 29% on 5 November, but then sea ice lingered into January remaining steady at an average of 34.8% until it retreated on 26 December, with intermittent advection in and out of the region until 16 January (Fig. 4B). Consistent with these trends, there were no positive sea ice melt contributions to

coastal surface waters in 2017 (Fig. 4C), while there were significant positive contributions in November and December in 2018 (Fig. 4D).  $\delta^{18}\text{O}$ -derived freshwater sources (sea ice melt and meteoric water) reflect the net seasonal freshwater balance, so negative values of percent sea ice melt indicate that seasonally, there was net sea ice growth in the Palmer region (i.e., more sea ice grew here than melted here). Thus, negative values in November and December 2017 likely indicate that sea ice was grown in the Palmer region the previous autumn and melted elsewhere in spring, whereas positive values in December and January 2018 indicate local spring melting that exceeds the previous autumn's local growth. During the sampling period (1 November to 31 March), sea ice concentrations were significantly higher in 2018-2019 than in 2017-2018 (Kruskal-Wallis  $p = 0.05$ ; Table 3). Aside from interannual differences in sea ice due to wind-driven advection, the physical and biogeochemical environment were relatively similar between the two years (Table 3, Fig. 5; Kruskal-Wallis  $p > 0.05$ ), except for nitrate and silicate which both had higher concentrations in 2018-2019 (Kruskal-Wallis  $p = 0.04$  and  $9.72 \times 10^{-14}$ , respectively; Table 3, Figs. 6A, B, E, F).

Phytoplankton data showed significantly higher chlorophyll-*a* concentrations in 2018-2019, but significantly lower H values (Kruskal-Wallis  $p = 0.03$  and  $0.05$ , respectively; Table 4, Fig. 7). Taxonomically, there were greater percent diatom and haptophyte biovolumes in 2018-2019 (Kruskal-Wallis  $p = 0.02$  and  $0.04$ , respectively), and greater percent mixed flagellate and prasinophyte biovolumes in 2017-2018 (Kruskal-Wallis  $p = 0.001$  and  $0.01$ , respectively; Supplementary Table 1, Fig. 3 pie charts).

### 3.4.3 Spring-autumn environmental trends

In both seasons, surface PAR was variable but showed a parabolic pattern, rising to a peak in late December/early January, then decreasing to the lowest values at the end of March (Fig. 5A-B). Surface temperature reflected seasonal warming, with the coldest temperatures in November, rising to a plateau in late January (Fig. 5C-D). Surface salinity, percent meteoric meltwater, and upper water-column stability were tightly linked in both seasons, with low salinity corresponding to high percent meteoric meltwater (Kendall; 2017-2018:  $p = 2.38 \times 10^{-5}$  and  $\tau = -0.66$ ; 2018-2019:  $p = 1.88 \times 10^{-5}$  and  $\tau = -0.62$ ) and high  $N^2$  values (Kendall; 2017-2018:  $p = 4.61 \times 10^{-12}$  and  $\tau = -0.70$ ; 2018-2019:  $p = 2.75 \times 10^{-12}$  and  $\tau = -0.67$ ). Higher  $N^2$  values were also correlated with lower wind speeds (Kendall; 2017-2018:  $p = 3.83 \times 10^{-4}$  and  $\tau = -0.39$ ; 2018-2019:  $p = 4.93 \times 10^{-6}$  and  $\tau = -0.47$ ). In general, salinity decreased through both seasons (Kendall; 2017-2018:  $p = 0.03$  and  $\tau = -0.24$ ; 2018-2019:  $p = 0.007$  and  $\tau = -0.28$ ) as percent meteoric meltwater increased (Kendall; 2017-2018:  $p = 0.02$  and  $\tau = 0.39$ ; 2018-2019:  $p = 0.001$  and  $\tau = 0.49$ ), however  $N^2$  was a bit more variable due to its relationship with wind speed (Fig. 5E-J). Wind speeds were generally higher in the early (beginning of November) and late (end of March) periods of the sampling season (Fig. 5K-L). Nutrients were variable throughout both seasons, with reductions in nitrate, phosphate, and often silicate co-occurring with peaks in chlorophyll-*a* (Fig. 6). Nitrate was also positively correlated to wind speed (Kendall; 2017-2018:  $p = 0.03$  and  $\tau = 0.24$ ; 2018-2019:  $p = 0.01$  and  $\tau = 0.30$ ).

Additionally, there was a notable series of events from late January to early February in 2019. A wind event from 25 January to 28 January (mean  $5.34 \text{ m s}^{-1}$ ) co-

occurred with a drop in  $N^2$ , a peak in salinity, a drop in percent meteoric meltwater, and a peak in nutrients (Fig. 5F, H, J, L and 6B, D, F). Just after this wind event, surface PAR increased dramatically and wind speeds dropped, causing percent meteoric meltwater to peak on 4 February corresponding with a dramatic dip in surface temperature, the lowest salinity of the season, the highest  $N^2$  value of the season, the highest chlorophyll-*a* value of the season, and the lowest nutrient concentrations of the season (Fig. 5B, D, F, H, J, L and 6B, D, F).

#### 3.4.4 *Spring-autumn phytoplankton succession patterns*

Both years mostly followed the seasonal succession phases found in previous local studies (Garibotti et al. 2005; Schofield et al. 2017). As sea ice concentration dropped below ~50% in November during the Ice Retreat Phase, the first phytoplankton bloom of the season occurred: a diatom-dominated ice edge bloom (Figs. 3, 4A-B, 8). In 2017-2018, the Ice Retreat Phase occurred from 14 November to 18 December with peak biovolume on 4 December ( $0.38 \mu\text{L L}^{-1}$ ), and in 2018-2019, the Ice Retreat Phase occurred from 2 November to 29 November with peak biovolume on 22 November ( $0.86 \mu\text{L L}^{-1}$ ) and a subsequent small peak on 29 November ( $0.39 \mu\text{L L}^{-1}$ ; Fig. 3C-D). In both years, the Ice Retreat Phase was dominated by centric diatoms (35.6% in 2017-2018 and 72.5% in 2018-2019; Fig. 8A-B) and these centric diatoms were mostly unidentified discoid cells with diameters  $> 20 \mu\text{m}$  (38.1% in 2017-2018 and 86.1% in 2018-2019), likely consisting of a mix of large, chain-forming diatoms including *Thalassiosira spp.* (Fig. 8C-D).

The Peak Summer Phase was characterized by cryptophytes and mixed flagellates. In 2017-2018, the Peak Summer Phase occurred from 22 December to 18 January and included the season's highest biovolume on 1 January ( $1.01 \mu\text{L L}^{-1}$ ), while in 2018-2019, the Peak Summer Phase occurred from 5 December to 3 January with a small peak on 20 December ( $0.60 \mu\text{L L}^{-1}$ ; Fig. 3C-D). In 2017-2018, cryptophytes and mixed flagellates dominated species composition, with 38.9% and 31.0%, respectively (Fig. 3C). In 2018-2019, cryptophytes and mixed flagellates increased in abundance from the initial bloom (5.1-29.7% and 12.0-20.4%, respectively), but diatoms also continued to dominate total composition (24.0% centric and 19.1% pennate; Fig. 3D, 8B).

The Late Summer Phase was enriched in smaller diatoms. In 2017-2018, the Late Summer Phase occurred from 22 January to the end of IFCB sampling (12 March) with a relatively constant biovolume (mean of  $0.31 \mu\text{L L}^{-1}$ ) and was dominated by 45.1% centric diatoms and 33.8% mixed flagellates (Fig. 3C, 8A). Of the centric diatoms, 59.3% were unidentified discoid cells with a diameter between 10-15  $\mu\text{m}$  and 27.5% were unidentified cells with a diameter between 15-20  $\mu\text{m}$  (Fig. 8C). In 2018-2019, however, the Late Summer Phase can be split into two distinct sub-phases: a water column stability-induced pennate diatom bloom (Late Summer Phase A) from 7 January to 14 February (peak biovolume of  $2.43 \mu\text{L L}^{-1}$  on 4 February, environmental conditions described in previous section), and a centric diatom-enriched late summer bloom (Late Summer Phase B) from 18 February to the end of IFCB sampling on (28 March; mean  $0.53 \mu\text{L L}^{-1}$  peak biovolume from 14 March to 25 March) more like the late summer community seen in 2017-2018 (Fig. 3D). Late Summer Phase A had 41.8% pennate diatoms (95.9% comprised of unidentified cells with diameters  $< 10 \mu\text{m}$ ) and 27.0%

centric diatoms (88.9% comprised of unidentified discoid cells with diameters  $> 20 \mu\text{m}$ ) (Fig. 8B, D, F). Late Summer Phase B had 50.5% centric diatoms (50.5% comprised of unidentified discoid cells with diameters  $10\text{-}15 \mu\text{m}$  and 33.7% comprised of unidentified cells with diameters  $15\text{-}20 \mu\text{m}$ ) and 29.8% mixed flagellates (Fig. 3D, 8D). The  $< 10 \mu\text{m}$  unidentified pennate diatoms likely included *Fragilariopsis spp.* and *Nitzschia spp.*, and the  $10\text{-}20 \mu\text{m}$  unidentified centric diatoms likely included smaller *Thalassiosira spp.* and *M. chilensis*.

Matching seasonal succession patterns, phytoplankton median cell size decreased through both years (Kendall; 2017-2018:  $p = 0.008$  and  $\tau = -0.31$ ; 2018-2019:  $p = 7.96 \times 10^{-5}$  and  $\tau = -0.42$ ; Fig. 9). This trend was positively correlated to a seasonal decrease in salinity in both years (Kendall; 2017-2018:  $p = 9.45 \times 10^{-4}$  and  $\tau = 0.38$ ; 2018-2019:  $p = 0.04$  and  $\tau = 0.22$ ), suggesting increasing freshwater might be responsible for the decrease in cell size.

### 3.5 Discussion

This work reveals the mechanisms of winter sea ice dynamics influencing interannual phytoplankton biomass and diatom abundance, as well as the importance of meteoric meltwater in structuring water column stability later in the summer season in tandem with a shift towards smaller phytoplankton cell sizes (e.g., pennate diatoms  $< 10 \mu\text{m}$ ). Despite significant differences in sea ice extent and total phytoplankton biomass between years, phytoplankton successional patterns were remarkably similar and driven by consistent seasonal drivers (e.g., solar irradiance, temperature, and meltwater), while storm/wind events drove more ephemeral differences between years (e.g., the late

January/early February 2019 event). Phytoplankton species composition and cell size information collected by the IFCB was invaluable for gaining this more in-depth understanding of seasonal and interannual phytoplankton dynamics at Palmer Station.

### *3.5.1 Drivers of interannual differences in phytoplankton biomass and composition*

Along the WAP, phytoplankton demonstrate strong interannual and regional variability seasonally-timed with light availability and spring sea ice retreat. As day length increases in austral spring, solar warming and sea ice melt help to stabilize the upper water column allowing phytoplankton to remain near the surface in waters with high light availability (Vernet et al. 2008; Venables et al. 2013). These conditions initiate large diatom-dominated spring blooms as we saw in both field years (Mitchell and Holm-Hansen 1991; Prézelin et al. 2000). Similar to other studies, we found that both longer winter sea ice durations (Saba et al. 2014; Rozema et al. 2017; Schofield et al. 2017) and a slower rate of sea ice retreat in spring-early summer (Garibotti et al. 2005; Annett et al. 2010; Gonçalves-Araujo et al. 2015) contributed to high phytoplankton abundance and a diatom-dominated phytoplankton community.

Winter sea ice duration was much shorter (40 days) in 2017 than in 2018, and the phytoplankton community had less diatoms and more mixed flagellates. Wind speed and direction in early spring (September to October) can precondition the water column due to its effect on sea ice and consequently percent sea ice melt, which in turn could either serve to enhance (as in 2018-2019) or dampen (2017-2018) surface freshening and stratification in sync with percent meteoric meltwater, influencing phytoplankton biomass and species composition. Although the spring ice edge retreated later in 2018-2019 than

in 2017-2018 (26 December versus 3 December), the initial phytoplankton bloom occurred earlier due to relatively low (~30%) sea ice coverage starting in early November, allowing adequate light for phytoplankton growth. Sea ice then slowly melted through mid-January, further enhancing meltwater stratification and stabilizing the upper water column, conditions optimal for phytoplankton growth that in turn contributed to significantly higher chlorophyll-*a* concentrations in 2018-2019 (Rozema et al. 2017). In contrast, in 2017, there was > 50% sea ice coverage through most of November, likely inhibiting light penetration and subsequent phytoplankton growth. Dramatic reduction in sea ice coverage at the end of November indicates rapid, wind-driven advection of sea ice from the region, leading to negative sea ice meltwater values near Palmer Station and allowing high variability in  $N^2$ , likely contributing to the significantly lower chlorophyll-*a* concentrations seen during this season (Rozema et al. 2017).

It is possible that with rapid wind-driven advection of sea ice from the region in 2017, less sea ice algae were released to seed the coastal region near Palmer Station. This can be compared to 2018 when sea ice lingered and contributed more meltwater and potentially more seed populations, with higher associated chlorophyll-*a* concentrations in 2018-2019 than in 2017-2018 (Ackley and Sullivan 1994; Van Leeuwe et al. 2018). Earlier sea ice advance in the autumn is expected to entrain higher concentrations of algae, therefore, the 16 day-earlier sea ice advance in autumn 2018 might also have contributed to increased phytoplankton concentrations in 2018-2019 (Garrison et al. 1983).

Silicate and nitrate were found at significantly higher concentrations in 2018-2019 than in 2017-2018. Typically, years with reduced sea ice and higher wind-driven mixing

lead to higher nutrient injection into surface waters from deeper, nutrient-rich waters (Annett et al. 2010). Following this logic, we would expect to see higher nutrient concentrations in 2017-2018. However, there were faster wind speeds at the start of the growing season in 2018 (Ice Retreat Phase mean =  $6.7 \text{ m s}^{-1}$ ) than in 2017 (Ice Retreat Phase mean =  $4.3 \text{ m s}^{-1}$ ) that could have contributed to higher initial concentrations. Additionally, there were much larger nutrient drawdown events by high biomass blooms in 2018-2019 than in 2017-2018 that would be expected to lower seasonal nutrient concentrations, emphasizing that wind-driven mixing must have more than compensated for the larger nutrient drawdown in 2018-2019.

Taxonomically, there were proportionally more mixed flagellates and prasinophytes in 2017-2018 and proportionally more diatoms and haptophytes in 2018-2019. Dominance of diatoms and haptophytes (e.g., *P. antarctica*) has been associated with the marginal sea ice zone where the water column is highly stratified and cells have ample light (Garibotti et al. 2005), which could explain why we saw higher proportions of both in 2018-2019. Low light environments (e.g., deep mixed layer depths) have been found to favor mixed flagellates, thus a significantly higher proportion of mixed flagellates in 2017-2018 may be related to variable  $\text{N}^2$  during that year (Schofield et al. 2017; Carvalho et al. 2019). Additionally, there was higher overall community diversity in 2017-2018, as large diatom blooms in 2018-2019 were dominated by only a few taxonomic groups.

### 3.5.2 *Drivers of phytoplankton seasonal succession*

Following phytoplankton trends found in previous years at Palmer Station (Garibotti et al. 2005; Schofield et al. 2017), we confirmed three distinct successional phases in both years despite variability in the environmental drivers: a large diatom-dominated Ice Retreat Phase, followed by a cryptophyte-dominated Peak Summer Phase, followed by a small diatom-enriched Late Summer Phase. This pattern matches the conceptual mandala developed by Behrenfeld et al. (2021). Community changes are driven by increases in the availability of limiting resources and subsequently overall growth conditions, and consider phytoplankton size, division rates, and loss rates (e.g., predation and sinking). Increases in available resources via mechanisms such as wind-driven mixing, changes in solar irradiance, coastal upwelling, etc. improve growing conditions that favor large phytoplankton species (e.g., diatoms) and allow phytoplankton division rates to accelerate, increasing phytoplankton concentrations. Bloom conditions deteriorate as resources are depleted, or as loss rates (e.g., predation, sinking) begin to exceed division rates.

The phytoplankton growing season initiates as limiting resources become less limiting – in the case of the WAP, this is primarily driven by seasonal increases in solar irradiance during spring sea ice retreat (Venables et al. 2013). Initial modest resource increases favor medium-sized species (e.g., small bloom-forming diatoms) that can rapidly accelerate division rates to achieve high maximum growth rates often before resources are depleted (Behrenfeld et al. 2021b), with eventual bloom termination as loss rates catch up to division rates. With sustained resources, larger species with slower acceleration of division rates and larger predator-prey lags begin to flourish (Behrenfeld

et al. 2021a), resulting in the large, centric diatom bloom seen during the Ice Retreat Phase. Overall growth conditions are maximized in years with protracted sea ice retreat (Annett et al. 2010), illustrated by higher peak phytoplankton biomass and a higher proportion of large, centric diatoms in 2018 compared to 2017. This late spring large, centric diatom bloom composed of species such as *Thalassiosira spp.* is also present in the Arctic, driven by upper water column stratification and seasonal increases in light availability (Lafond et al. 2019; Ardyna et al. 2020). This bloom terminates as inorganic nutrients are depleted and/or loss rates begin to exceed division rates.

Due to reduced nutrient concentrations from the large diatom bloom in the Ice Retreat Phase, the next successional phase (Peak Summer Phase) favors mixotrophic phytoplankton such as WAP cryptophytes (Gast et al. 2014; Trefault et al. 2021), that can both photosynthesize and consume particulate organic matter amassed over earlier bloom phases (Edwards 2019; Behrenfeld et al. 2021a). Cryptophytes are often found in deeper, low-light conditions where they can supplement photosynthesis with phagotrophy (Goes et al. 2014), however, we saw an increase in surface water biomass during the Peak Summer Phase when PAR was highest. High-light environments could give mixotrophs a competitive advantage over heterotrophs, as they can supplement their carbon supply with photosynthesis (Edwards 2019). In addition, cryptophytes are especially well-adapted to high-light environments due to specialized protective pigments (Mendes et al. 2017). Contrary to other WAP studies (Moline et al. 2004; Mendes et al. 2017; Schofield et al. 2017; Pan et al. 2020), we did not find significant correlations between cryptophytes and low salinity glacial meltwater or high temperature. In fact, percent meteoric water during the Peak Summer Phase was below the seasonal mean in both

years (range = 3.5-4.6% and mean = 5.03% in 2017-2018; range = 2.6-3.9% and mean = 4.52% in 2018-2019), surface temperatures did not reach seasonal maxima until the Late Summer Phase (mean Peak Summer Phase surface temperatures were 1.07°C and -0.06°C compared to maximums of 1.74°C and 2.52°C for 2017-2018 and 2018-2019, respectively), and in 2018 the Peak Summer Phase occurred while there was still ~30% sea ice coverage. Thus, it is likely that biotic successional patterns drove this rise in cryptophytes rather than specific abiotic environmental drivers. This bloom terminates as resources are depleted, or losses begin to exceed division rates (Behrenfeld et al. 2021a).

In the Late Summer Phase, we saw Behrenfeld et al. (2021a)'s cycle begin again, with increases in wind-driven mixing that replenished nutrients (e.g., iron) to surface waters and allowed for small diatoms (typically 10-20  $\mu\text{m}$  centric diatoms) to bloom. Iron concentrations have been found to be important for shifting phytoplankton composition from a phytoflagellate-dominated community to a diatom-dominated community (Boyd et al. 2000). In the Palmer region, iron supply primarily comes from shallow sediments delivered to the surface waters by wind-driven vertical mixing (Sherrell et al. 2018). We did not sample iron in this study, but previously collected seasonal data in the Palmer region showed a 6-fold increase from late-January to mid-February with increases in wind speed and a deepened mixed layer depth (Carvalho et al. 2016), which matches the start time of this phase. The Last Summer Phase is characterized by variable mixed layer depths (as inferred from 25 m-averaged Brunt Vaisala Frequency,  $N^2$ ), driven by contrasting increases in wind speed and glacial meltwater inputs. These variable conditions may limit the duration and magnitude of this small diatom bloom and prevent the progression to larger species. Instead, we saw an increased proportion of mixed

flagellates, which could be the result of higher wind-mixing and decreasing daylength in late summer that selects for species that do well in wind-mixed low-light environments (Schofield et al. 2017; Carvalho et al. 2019).

In 2018-2019, the first half of the Late Summer Phase was characterized by a very large, stability-induced pennate diatom bloom (Late Summer Phase A). This bloom had almost twice as much biomass as any other bloom seen over both years, possibly because smaller diatoms have fast growth acceleration rates that allow them to reach high maximum growth rates quickly (Behrenfeld et al. 2021b), and because the wind event that preceded the bloom likely resuspended iron as well as macronutrients. This bloom also co-occurred with a pulse of glacial meltwater and increased stratification (i.e., very high  $N^2$ ), which has been seen in other field studies (Beans et al. 2008; Höfer et al. 2019; Pan et al. 2020). Additionally, Hernando et al. (2015) experimentally exposed phytoplankton populations from Potter Cove, Antarctica to low salinity conditions (30 PSU) and found a decline in the abundance of large centric diatoms from ~90% on day 2 to ~0% on day 7, and an increase in abundance of small pennate diatoms from ~0% on day 4 to ~95% on day 8. They attribute these changes to differing osmotic stress tolerances: in large centric diatoms, a decrease in salinity caused cell size increases, compression of chloroplasts, granularization of the protoplasm, and retraction of the cytoplasm, while some small pennate diatoms (e.g., *Fragilariopsis cylindrus*) may contain genes beneficial for adaptation to extreme environmental conditions in polar oceans and sea ice. Thus, high glacial meltwater during this bloom could select for small pennate diatoms.

Over the course of the season, we observed a decreasing trend in median cell diameter in association with increasing percent meteoric water and decreased salinity. Stronger surface stratification due to increased ice melt can reduce nutrients in surface waters, giving an advantage to smaller phytoplankton with high surface-area-to-volume ratios and reduced sinking rates (Li et al. 2009). However, macronutrients do not appear to be limiting in either year, and  $\text{Si:N} > 2$  also suggests no significant limitation by iron or other micronutrients (Clarke et al. 2008). As mentioned above, increased meteoric meltwater inputs could cause cell size and composition shifts associated with different species' tolerances to osmotic stress, especially for diatoms (Hernando et al. 2015). Since diatoms contributed the highest annual percent composition to the population in low (44% in 2017-2018) and high (66% in 2018-2019) chlorophyll years, cell size shifts in diatoms are large contributors to the decreasing seasonal trend seen in overall phytoplankton cell size.

### 3.5.3 *HPLC versus IFCB-derived abundance and taxonomy*

In general, HPLC and IFCB-derived biomass and percent taxa estimates agreed. There were positive, significant correlations between overall biomass for the two methods and for all taxonomic groups except haptophytes. Similar to other WAP studies (Kozłowski et al. 2011), the strongest relationships between HPLC and imaging (e.g., IFCB and microscopy) methods were seen in cryptophyte and diatom percent compositions, and weaker relationships were found for prasinophytes and mixed flagellates. Our results showed that HPLC methods underpredicted mixed flagellates relative to IFCB methods, in agreement with Kozłowski et al. (2011), who suggests this

is due to misclassifications of other cells within this group during microscopic analysis. Alternatively, pigment ratios derived by Kozłowski et al. (2011) for mixed flagellates could be missing a fraction of the population, which would suggest that IFCB and microscopy might be more reliable for methods for quantifying mixed flagellate abundance.

In our IFCB samples, we excluded all cells with a major axis length less than 20 pixels (5.88  $\mu\text{m}$ ) prior to analysis, as these small cells are below the quantifiable limit of detection based on our instrument resolution, and thus have a high probability of being misclassified. *P. antarctica* is mostly found in the flagellate stage in the summer in the WAP region below 64° S, with cell diameters < 5  $\mu\text{m}$  (Kozłowski et al. 2011; Biggs et al. 2019). Since *P. antarctica* is the dominant haptophyte in our region (Annett et al. 2010), IFCB methods likely underestimated haptophyte abundances as many cells were likely excluded by our 5.88  $\mu\text{m}$  screen, leading to the non-significant relationship found between IFCB and HPLC-estimated haptophyte percent composition. This also could be the reason for the slight overprediction of prasinophytes using HPLC compared to IFCB, and thus the weaker correlation between the two methods.

There were a few notable discrepancies in overall abundance between the two methods, particularly on 19 November 2018 and 21 January 2019, where HPLC showed peaks in chlorophyll-*a* that were absent or lessened when portrayed by IFCB biovolume. This discrepancy may not be an error in methodology and could instead reflect high chlorophyll-*a* to biovolume ratios during these two days. However, a potential source of error could be classification within “detritus” and “multiple” categories. Phytoplankton cells were commonly seen attached to detritus particles, or in large conglomerations.

These images were eliminated from the analysis as they could not be reliably sorted into a single taxonomic group. Although it is possible that excluding these groups reduced the biovolume in some samples, this does not seem to be the case for the days in question, as total biovolume including non-phytoplankton particles was still very low (see Fig. 1 in Nardelli et al. 2021). Although both peaks were dominated by centric diatoms which typically have diameters greater than 10  $\mu\text{m}$  in this region (Annett et al. 2010), there are some species with diameters less than 5.88  $\mu\text{m}$  (e.g., *Minidiscus chilensis*), therefore the size cut-off could be responsible for this difference between methods. The absent 21 January 2019 peak could also be the result of preservation bias in the IFCB analysis, as preserved samples were found to have 48% less biovolume than live samples.

#### 3.5.4 *Future implications*

Despite significantly different sea ice conditions and phytoplankton biomass between these two years, phytoplankton biomass began to increase when local sea ice concentration dropped below  $\sim 50\%$ . The tight coupling between spring sea ice retreat and the start of the phytoplankton growing season leaves this ecosystem vulnerable to climate change-induced phenology shifts. From 1992-2015, spring sea retreat near Palmer Station shifted earlier by 1.28 days per year (Schofield et al. 2017), and this trend is expected to continue. Earlier sea ice retreat and subsequent water column stratification could shift the start of the growing season earlier: Henson et al. (2018) found that the Southern Ocean spring bloom advances by  $\sim 5$ -10 days per decade, which would result in a  $\sim 50$ -100 day advance by 2100. An advance in the spring phytoplankton bloom associated with earlier thermal stratification has already been seen in other systems, including high-altitude and

temperate lakes (Winder and Schindler 2004; Maeda et al. 2019) and temperate coastal oceans (Hunter-Cevera et al. 2016). This could lead to a mismatch between the timing of the spring bloom and optimal seasonal light levels, and to predator-prey mismatches where spring predators are unable to alter their phenology to match the changes in interannual spring phytoplankton bloom timing (Cushing 1990; Edwards and Richardson 2004; Ardyna et al. 2014).

Additionally, our results suggested protracted sea ice melt in the coastal region could be important for algal seeding, leading to high chlorophyll-*a* years dominated by diatoms. With increased frequency of stronger wind events along the WAP associated with increases in the positive phase of the Southern Annular Mode during austral summer (Thompson and Solomon 2002), it is possible that there may be more years like 2017 when the sea ice was rapidly advected from the coastal region. The phytoplankton community seen in 2017-2018 may be representative of future phytoplankton communities without sea ice algal seeding, either because high intensity wind events clear the sea ice before local melting can occur, or if eventually there is no longer persistent winter sea ice. Although 2017-2018 held higher species diversity than 2018-2019, years with low chlorophyll-*a* concentrations lead to less successful Antarctic krill recruitment (Saba et al. 2014), which has negative consequences for higher trophic levels (Constable et al. 2014). However, more frequent high intensity wind events throughout the summer could also lead to increased iron concentrations in surface waters due to increased sediment resuspension (Sherrell et al. 2018), leading to heightened primary production and a diatom-dominated community (Boyd et al. 2000), and therefore more successful krill recruitment.

Finally, the connection between increasing seasonal meltwater and decreasing phytoplankton cell size could be indicative of changes we might see with further warming and melting along the WAP. A shift to smaller phytoplankton could cause a shift in zooplankton from krill to smaller zooplankton species (e.g., microzooplankton), as krill are unable to capture particles  $< 10 \mu\text{m}$  due to the filter size of their feeding apparatus (McClatchie and Boyd 1983), and microzooplankton selectively feed on smaller phytoplankton (Garzio and Steinberg 2013). A predominance of microzooplankton in coastal waters near glaciers with high proportions of small cells has been seen in other studies (Beans et al. 2008; Garcia et al. 2019). Thus, a meltwater-induced shift to smaller phytoplankton cells could cause the rise of a microbial food web, with microzooplankton grazing small phytoplankton cells, and krill consuming microzooplankton (Bernard et al. 2012). A longer food web could have important implications for carbon cycling (Sailley et al. 2013) and for krill lipid content (Ruck et al. 2014), which in turn could negatively impact top predator populations.

Although coastal WAP phytoplankton are tightly linked to ice-related physical dynamics (e.g., sea ice duration and concentration, sea ice and meteoric meltwater, mixed layer depth and strength of stratification/ $N^2$ ), they seem to be adaptable to year-to-year variation in environmental conditions as evidenced by the consistent seasonal succession between years in this study. Yet, there will likely be tipping points where changes in climate (e.g., warming, decreased sea ice, increased glacial meltwater) fundamentally change phytoplankton bloom phenology, total biomass, and community composition, with important implications for carbon export, food web structure, and energy transfer efficiency (Sailley et al. 2013). Further work is needed to assess whether the tendency

towards an earlier spring ice-edge retreat since 1992 (Schofield et al. 2017) has driven an earlier spring bloom timing along the coastal WAP, and how this might affect higher trophic levels via predator-prey mismatches. Seasonal zooplankton phenology studies in the coastal WAP would also be helpful for determining if there are interannual and seasonal community shifts that match the trends seen in our study. Additionally, collecting more seasonal iron measurements concurrent with phytoplankton biomass and species composition data would help to confirm whether a late summer pennate diatom bloom is driven by wind-driven iron resuspension or a higher tolerance to late-summer increases in glacial meltwater inputs in the Palmer region. However, our study is an important step towards defining the environmental drivers of seasonal and interannual phytoplankton community changes in coastal polar regions.

### **3.6 Acknowledgments**

This work was supported by the National Science Foundation Antarctic Organisms and Ecosystems Program (PLR-1440435) as part of the PAL-LTER program, and by NASA (19-IDS19-0085). Additionally, S.N. acknowledges support from the Rutgers Institute of Earth, Ocean, and Atmospheric Sciences graduate fellowship. HPLC data was provided by Nicole Waite,  $\delta^{18}\text{O}$  data for meltwater calculations was provided by Michael Meredith, and nutrient data was provided by Naomi Manahan. Frank McQuarrie, Taylor Dodge, Marie Zahn, Anna Bashkirova, and Hailey Conrad helped with data collection in the field. Thank you to Alison Chase and Sasha Kramer for help with taxonomic identifications. This work would not have been possible without Palmer

Station personnel, particularly the marine technicians, lab manager, and instrument technicians from the 2017-2018 and 2018-2019 field seasons.

### 3.7 Tables

**Table 1.** Compiled cell size ( $\mu\text{m}$ ) metrics from both field seasons for each taxonomic group using Imaging FlowCytobot data.

<b>Taxonomic Groups</b>	<b>n</b>	<b>Min</b>	<b>Max</b>	<b>Median</b>	<b>Std</b>
Cryptophytes	22161	4.11	19.77	8.61	1.39
Mixed Flagellates	67870	4.08	60.94	5.65	2.03
Haptophytes	11221	4.21	51.87	5.97	1.47
Prasinophytes	5319	4.09	44.60	8.30	1.73
Diatoms	75540	4.08	122.03	5.87	3.85
Centric Diatoms	15184	4.08	122.03	7.86	6.84
<i>Chaetoceros spp.</i>	659	4.11	57.16	6.56	9.78
<i>Corethron pennatum</i>	109	8.92	92.25	31.08	18.07
<i>Eucampia antarctica</i>	31	33.32	84.45	43.90	18.01
<i>Dactyliosolen spp.</i>	12	7.95	40.47	12.14	10.19
<i>Odontella weissflogii</i>	1	NA	NA	53.29	NA
<i>Proboscia spp.</i>	12	16.72	73.57	45.47	16.26
Unidentified discoid diatoms 0-10 $\mu\text{m}$	8256	4.08	9.99	6.95	0.92
Unidentified discoid diatoms 10-15 $\mu\text{m}$	4183	10.00	15.00	12.93	1.29
Unidentified discoid diatoms 15-20 $\mu\text{m}$	1241	15.00	19.98	15.94	1.06
Unidentified discoid diatoms > 20 $\mu\text{m}$	680	20.00	122.03	35.91	19.52
Pennate Diatoms	60356	4.08	51.91	5.67	1.87
<i>Amphiprora spp.</i>	46	8.16	27.84	16.98	4.51
<i>Cocconeis spp.</i>	42	4.44	31.92	12.91	4.95
<i>Cylindrotheca spp.</i>	235	4.43	17.52	9.77	2.12
<i>Licmophora spp.</i>	42	5.55	38.41	15.32	5.96
<i>Pseudo-Nitzschia spp.</i> chains	499	5.15	30.76	14.53	3.87
Unidentified pennate diatoms 0-10 $\mu\text{m}$	58169	4.08	9.99	5.64	0.90
Unidentified pennate diatoms 10-15 $\mu\text{m}$	1093	10.00	14.97	11.05	1.16
Unidentified pennate diatoms 15-20 $\mu\text{m}$	105	15.05	19.97	17.50	1.46
Unidentified pennate diatoms > 20 $\mu\text{m}$	125	20.02	51.91	24.77	6.13

**Table 2.** Annual sea ice indices for 2017-2018 and 2018-2019.

	<b>Advance</b>	<b>Retreat</b>	<b>Duration</b>	<b># Ice Days</b>
2017-2018	July 17, 2017	December 2, 2017	138 days	125 days
2018-2019	July 1, 2018	December 26, 2018	178 days	177 days

**Table 3.** Interannual differences in environmental variables. Bold *p*-values indicate significant differences between years.

Variable	2017-2018					2018-2019					Kruskal-Wallis Test	
	n	Mean	Min	Max	Std	n	Mean	Min	Max	Std	Chi <sup>2</sup>	<i>p</i>
SIC	77	22.16	0	65.00	25.03	77	32.57	0	96.00	14.86	3.97	<b>0.05</b>
PAR	39	348.94	95.44	729.22	181.03	39	352.29	52.66	776.62	181.62	0.007	0.93
Temp	38	0.65	-1.11	1.74	0.83	38	0.46	-1.03	2.52	0.84	1.71	0.19
Sal	38	33.30	32.40	33.93	0.34	43	33.35	32.26	33.88	0.30	0.40	0.53
% met	39	5.03	3.27	8.24	1.31	43	4.52	2.55	8.08	1.53	2.38	0.12
% sim	39	-1.32	-2.89	-0.02	0.79	43	-0.95	-4.41	0.69	1.22	3.16	0.08
N <sup>2</sup>	38	0.0001	-2.1x10 <sup>-5</sup>	0.0004	0.0001	43	0.0002	1.3x10 <sup>-5</sup>	0.0004	9.0x10 <sup>-5</sup>	0.06	0.81
WS	39	4.65	2.19	13.22	2.11	39	4.51	1.80	8.86	1.85	0.01	0.92
NO <sub>3</sub>	39	21.23	15.51	25.65	2.55	43	22.49	12.20	29.57	3.79	4.25	<b>0.04</b>
PO <sub>4</sub>	39	1.58	1.21	1.96	0.16	43	1.64	0.96	2.14	0.28	2.74	0.10
SiO <sub>4</sub>	39	54.60	37.33	62.35	4.58	43	74.08	63.85	82.50	4.22	55.42	<b>9.7x10<sup>-14</sup></b>

\* SIC = Sea Ice Concentration (%), PAR = photosynthetically active radiation ( $\mu\text{mol sec}^{-1} \text{m}^{-1}$ ), Temp = surface temperature ( $^{\circ} \text{C}$ ), Sal = surface salinity (PSU), % met = percent meteoric meltwater, % sim = percent sea ice melt, N<sup>2</sup> = buoyancy frequency, WS = wind speed ( $\text{m s}^{-1}$ ), and nitrate (NO<sub>3</sub>), phosphate (PO<sub>4</sub>), and silicate (SiO<sub>4</sub>) have units of  $\mu\text{mol L}^{-1}$ .

**Table 4.** Interannual differences in phytoplankton variables. Bold *p*-values indicate significant differences between years.

Variable	2017-2018					2018-2019					Kruskal-Wallis Test	
	n	Mean	Min	Max	Std	n	Mean	Min	Max	Std	Chi <sup>2</sup>	<i>p</i>
Chl- <i>a</i>	39	2.03	0.41	6.85	1.40	43	3.93	0.03	19.09	3.88	4.90	<b>0.03</b>
H	35	2.22	1.21	2.83	0.36	35	1.97	0.64	2.65	0.53	3.69	<b>0.05</b>
Biovolume	35	0.29	0.05	1.01	0.19	35	0.40	0.005	2.43	0.51	0.47	0.49
Abundance	35	1341.84	55.36	3568.83	868.75	35	3937.79	7.59	36702.26	7778.31	0.01	0.91
Median Diameter	35	6.71	4.98	11.48	1.43	35	6.27	5.24	12.73	1.26	2.76	0.10

\* Chl-*a* = HPLC-derived chlorophyll-*a* concentration (mg m<sup>-3</sup>), H = Shannon Diversity Index, Biovolume = IFCB-derived phytoplankton biovolume (μL L<sup>-1</sup>), Abundance = IFCB-derived phytoplankton cell abundance (cells mL<sup>-1</sup>), and Median Diameter has units of μm.

### 3.8 Figures

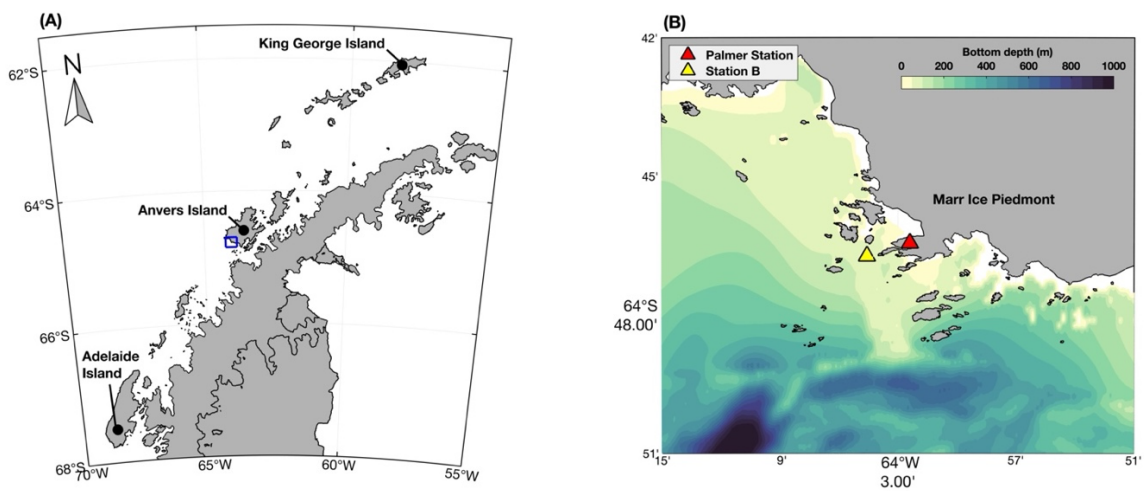


**Figure 1.** (A) Map of West Antarctic Peninsula with blue box indicating the extents of the Palmer region shown in (B).

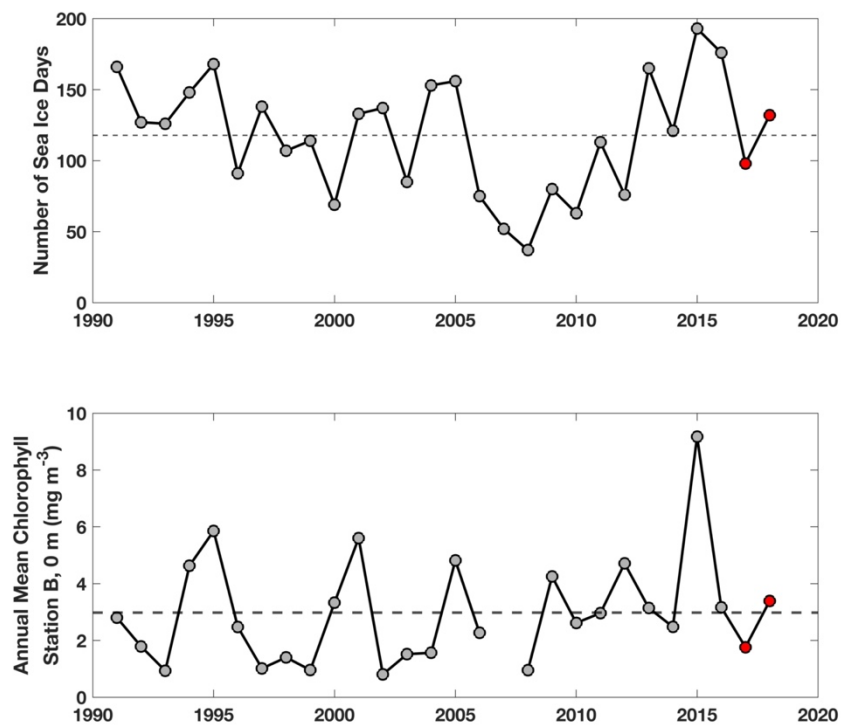


**Figure 2.** Historical timeseries for **(A)** number of sea ice days in the 50 km Palmer region and **(B)** annual mean surface chlorophyll-*a* at Station B. Red dots indicate 2017-2018 and 2018-2019, and the dashed vertical line indicates the mean value for the displayed timeseries.

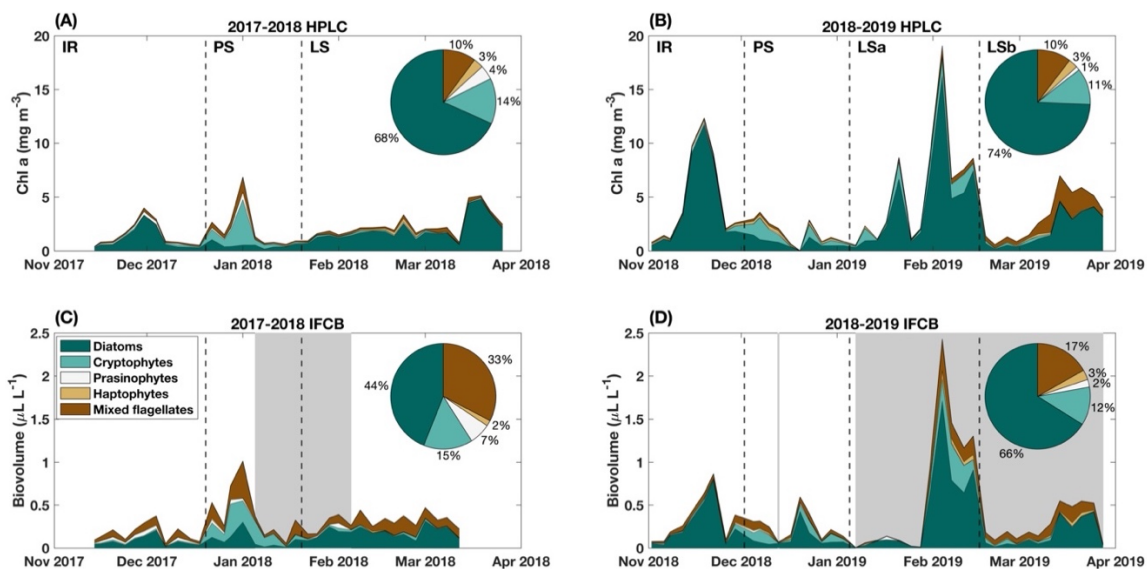


**Figure 3.** Seasonal (**A and B**) HPLC-derived chlorophyll-*a* and (**C and D**) IFCB-derived biovolume for each phytoplankton group. Pie chart insets show annual total percent (**A and B**) chlorophyll-*a* or (**C and D**) biovolume for each group. Grey areas in plots C and D indicate periods when IFCB results are based on preserved IFCB samples. Vertical dashed lines indicate divisions of seasonal succession phases (IR = Ice Retreat Phase, PS = Peak Summer Phase, and LS = Late Summer Phase).

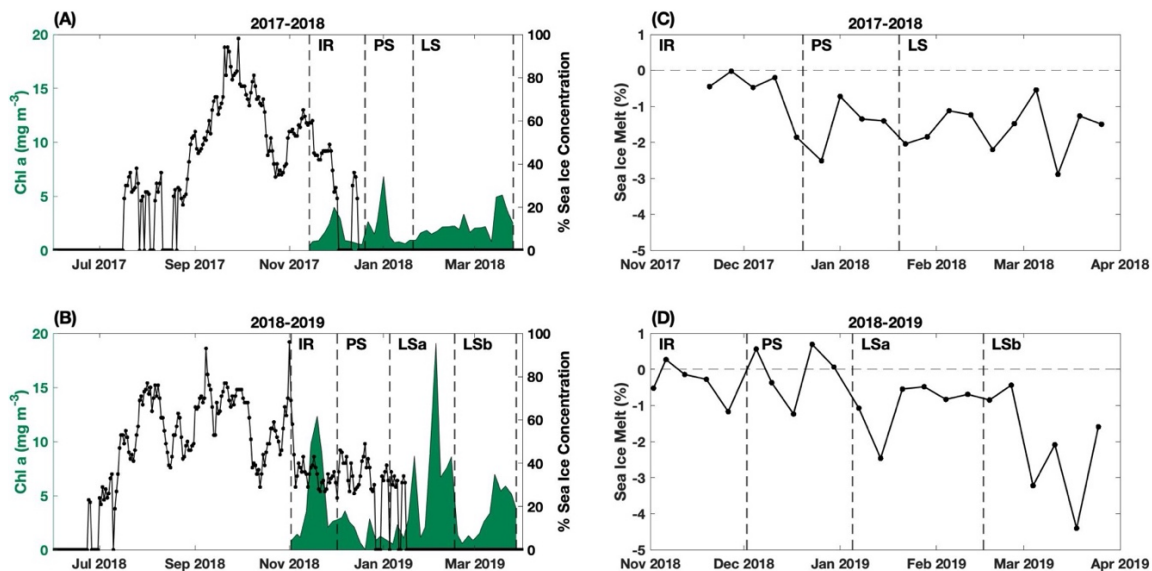


**Figure 4.** (A and B) Seasonal chlorophyll-*a* concentration (green) overlaid with daily percent sea ice concentration (black line) for (A) 2017-2018 and (B) 2018-2019. Percent sea ice melt for (C) 2017-2018 and (D) 2018-2019, where positive values indicate sea ice melt, negative values indicate sea ice formation. Vertical dashed lines indicate divisions of seasonal succession phases (IR = Ice Retreat Phase, PS = Peak Summer Phase, and LS = Late Summer Phase).

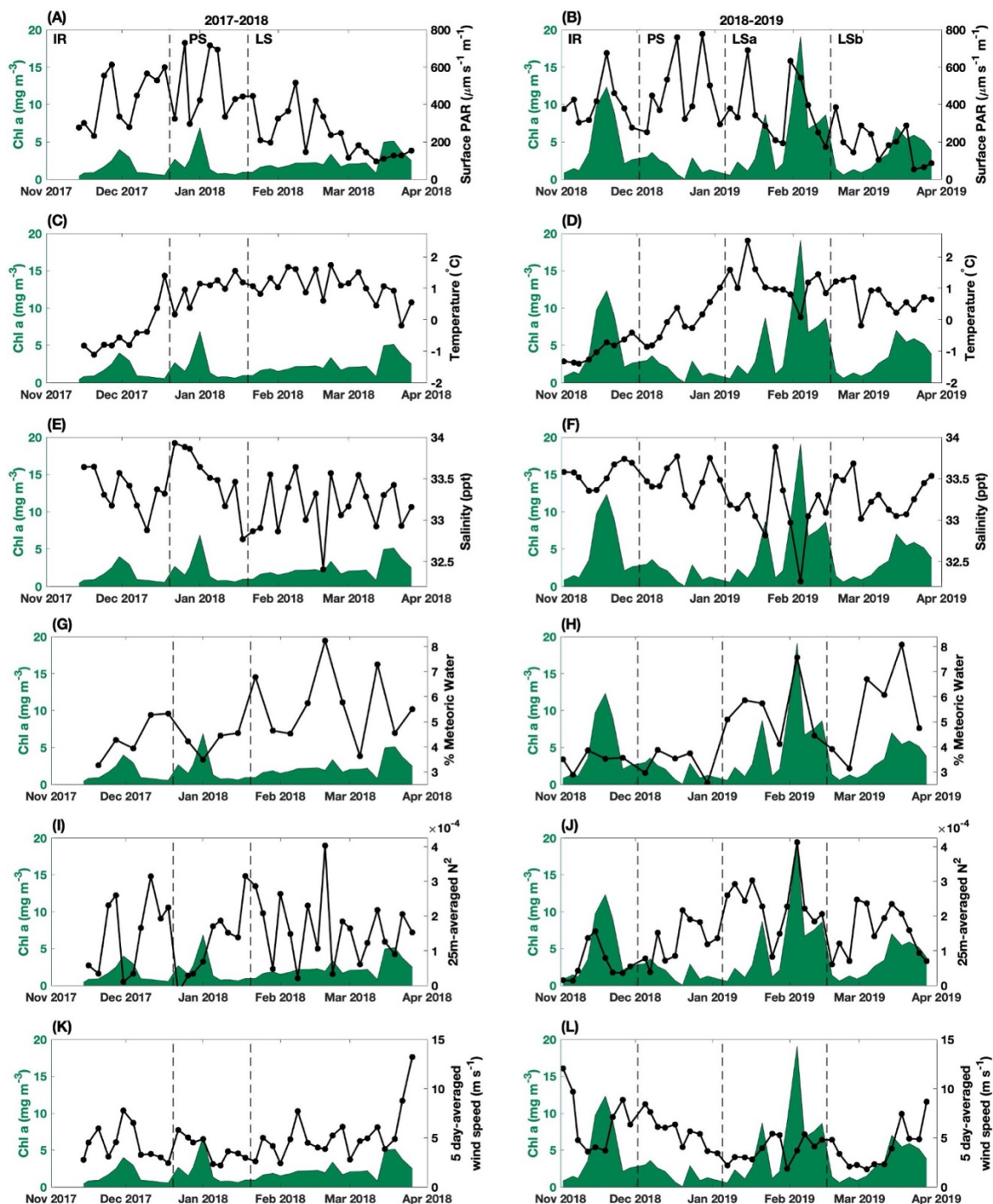


**Figure 5.** Seasonal chlorophyll-*a* concentrations (green) for 2017-2018 (left column) and 2018-2019 (right column) overlaid with environmental variables (black lines): **(A and B)** Surface PAR, **(C and D)** temperature, **(E and F)** salinity, **(G and H)** percent meteoric water, **(I and J)** 25 m-averaged N<sup>2</sup>, and **(K and L)** 5 day-averaged wind speed. Vertical

dashed lines indicate divisions of seasonal succession phases (IR = Ice Retreat Phase, PS = Peak Summer Phase, and LS = Late Summer Phase).

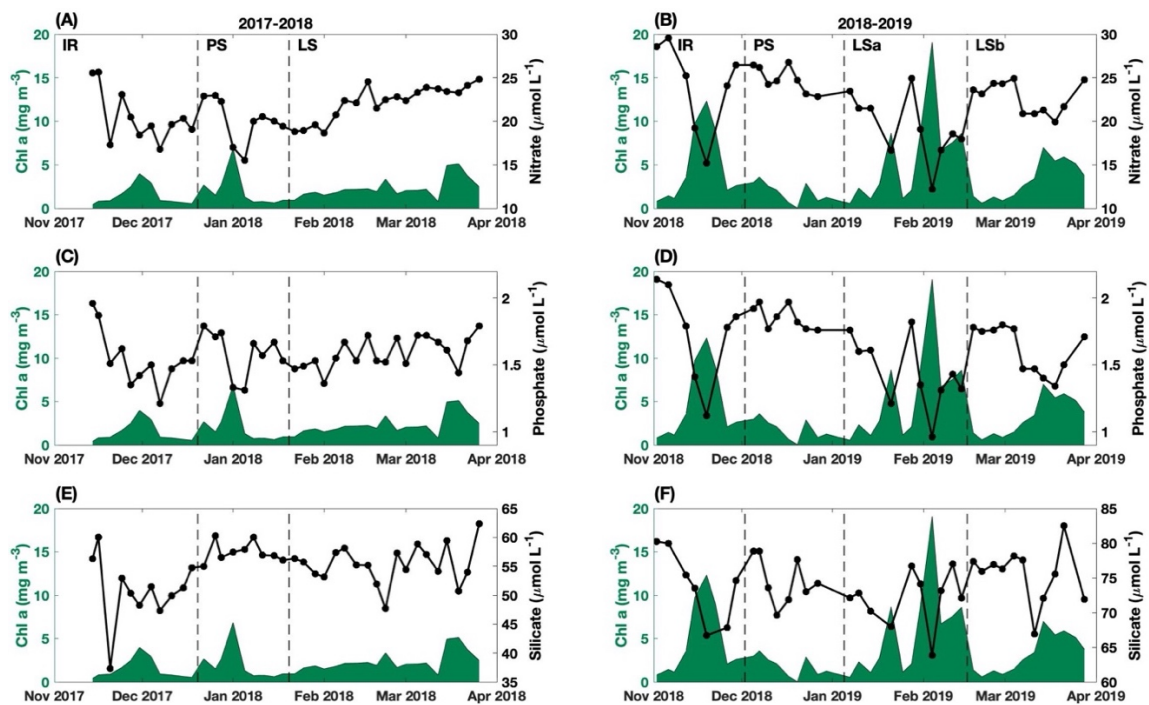


**Figure 6.** Seasonal chlorophyll-*a* concentrations (green) for 2017-2018 (left column) and 2018-2019 (right column) overlaid with nutrient data (black lines): **(A and B)** nitrate, **(C and D)** phosphate, and **(E and F)** silicate (note that the two years are showing different scales). Vertical dashed lines indicate divisions of seasonal succession phases (IR = Ice Retreat Phase, PS = Peak Summer Phase, and LS = Late Summer Phase).

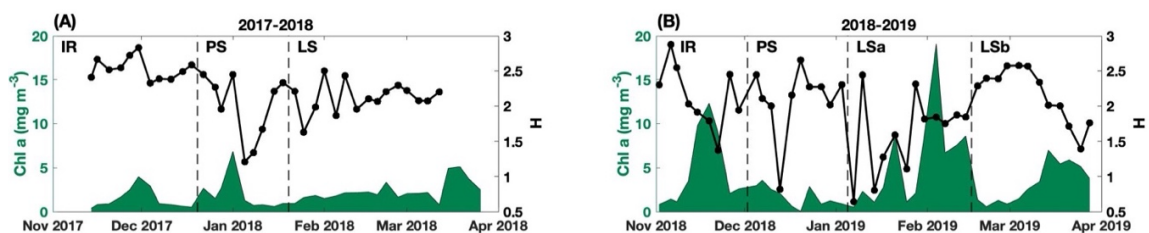


**Figure 7.** Seasonal chlorophyll-*a* concentrations (green) for (A) 2017-2018 and (B) 2018-2019 overlaid with H diversity values. Vertical dashed lines indicate divisions of seasonal succession phases (IR = Ice Retreat Phase, PS = Peak Summer Phase, and LS = Late Summer Phase).

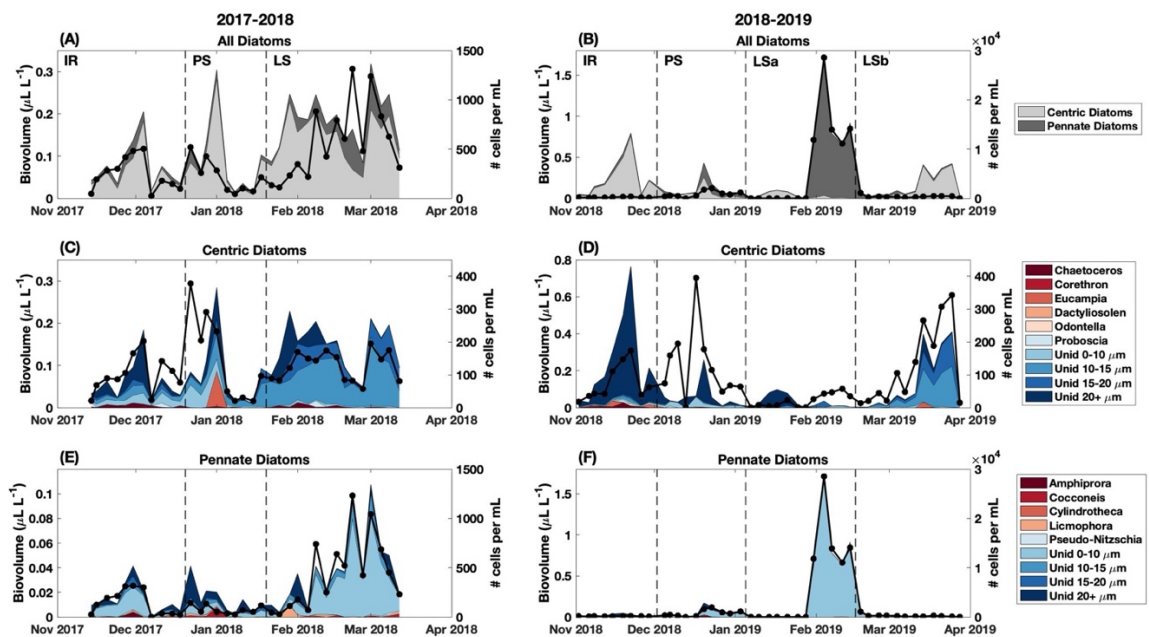


**Figure 8.** Diatom seasonal diversity for 2017-2018 (left column) and 2018-2019 (right column) for: (A and B) all diatoms, (C and D) centric diatoms, and (E and F) pennate diatoms. Solid black line indicates cell abundance, and vertical dashed lines indicate divisions of seasonal succession phases (IR = Ice Retreat Phase, PS = Peak Summer Phase, and LS = Late Summer Phase). Unid = unidentified.

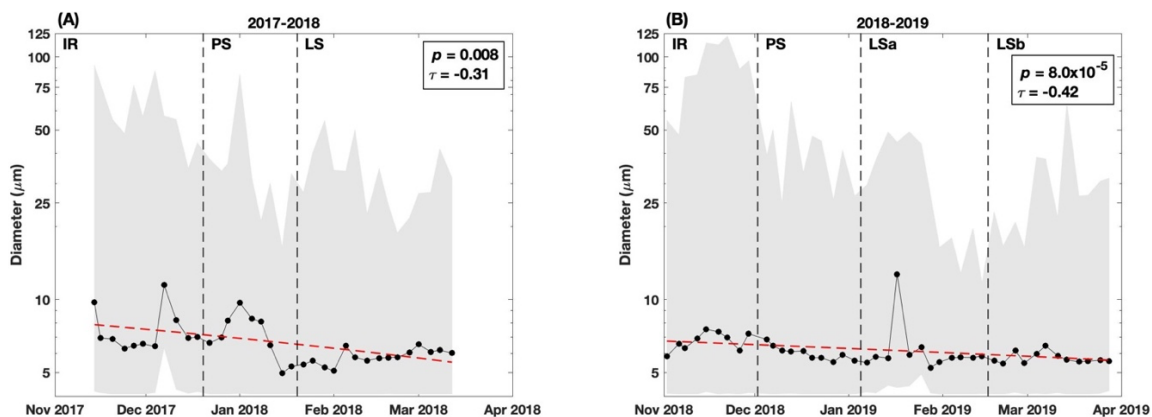


**Figure 9.** Seasonal decrease in median cell diameter for **(A)** 2017-2018 and **(B)** 2018-2019. Grey region shows range of diameters for each sampling day. Red dashed line shows linear decreasing trend in median diameter, with Kendall rank correlation metrics displayed in the textbox in the top right corner of each subplot. Vertical dashed lines indicate divisions of seasonal succession phases (IR = Ice Retreat Phase, PS = Peak Summer Phase, and LS = Late Summer Phase).

### 3.9 Supplementary tables

**Supplementary Table 1.** Interannual differences in phytoplankton taxonomy. Bold *p*-values indicate significant differences between years.

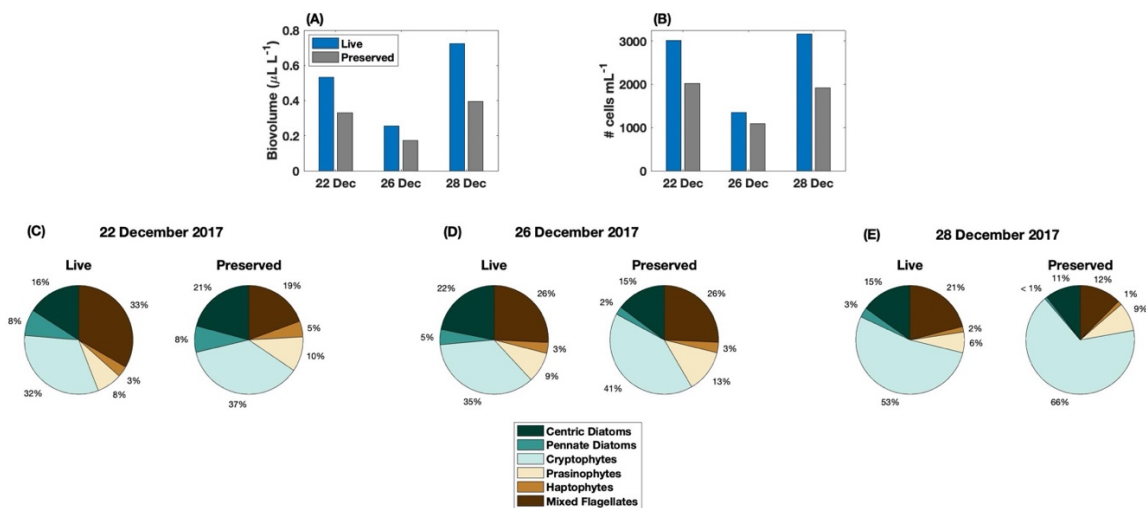
Taxa	Variable	2017-2018					2018-2019					Kruskal-Wallis Test	
		n	Mean	Min	Max	Std	n	Mean	Min	Max	Std	Chi <sup>2</sup>	p
Diat	Chl	39	1.38	0.20	4.80	1.13	43	2.92	0.01	16.36	3.50	2.45	0.12
	% Chl	39	67.60	8.17	93.55	20.94	43	64.79	29.75	95.19	19.71	0.50	0.48
	Biovol	35	0.13	0.01	0.32	0.08	35	0.25	0.005	1.72	0.36	0.01	0.91
	% Biovol	35	43.76	10.00	73.45	17.98	35	56.36	18.18	96.88	23.63	5.38	<b>0.02</b>
Crypt	Chl	39	0.28	0	4.24	0.71	43	0.45	0.01	2.02	0.56	3.10	0.08
	% Chl	39	13.33	0	61.79	16.48	43	14.85	0.28	56.14	14.77	0.66	0.42
	Biovol	35	0.05	0.003	0.39	0.09	35	0.07	0	0.42	0.10	0.34	0.56
	% Biovol	35	15.70	1.00	73.90	19.73	35	15.48	0	46.69	13.59	0.52	0.47
MF	Chl	39	0.20	0	1.37	0.22	43	0.41	0	2.43	0.62	0.13	0.72
	% Chl	39	10.10	0	20.07	4.99	43	12.60	0	49.44	14.56	2.23	0.13
	Biovol	35	0.09	0.02	0.43	0.08	35	0.07	0.0004	0.36	0.07	3.60	0.06
	% Biovol	35	32.18	11.60	57.86	12.14	35	22.03	1.14	58.45	14.97	10.17	<b>0.001</b>
Pras	Chl	39	0.09	0.03	0.69	0.12	43	0.05	0	0.24	0.05	7.48	<b>0.006</b>
	% Chl	39	4.78	1.21	14.05	3.31	43	1.83	0	7.43	1.73	21.60	<b>3.35x10<sup>-6</sup></b>
	Biovol	35	0.02	0.0004	0.06	0.02	35	0.006	0	0.04	0.008	5.94	<b>0.01</b>
	% Biovol	35	6.33	0.16	19.05	6.50	35	2.65	0	27.00	5.05	6.65	<b>0.01</b>

Hapto	Chl	39	0.06	0	0.32	0.06	43	0.11	0	0.27	0.08	12.98	<b>0.0003</b>
	% Chl	39	4.18	0	13.33	3.61	43	5.93	0	18.90	5.12	1.81	0.18
	Biovol	35	0.005	9.41x10 <sup>-5</sup>	0.02	0.004	35	0.01	0	0.09	0.02	4.25	<b>0.04</b>
	% Biovol	35	2.03	0.10	8.47	1.80	35	3.48	0	13.87	3.13	4.35	<b>0.04</b>

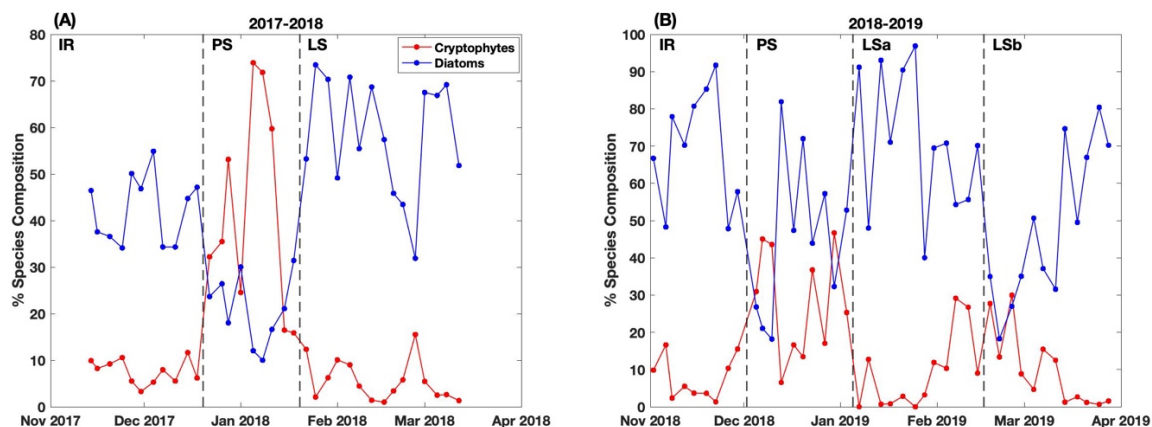
\* Diat = Diatoms, Crypt = Cryptophytes, MF = Mixed Flagellates, Pras = Prasinophytes, and Hapto = Haptophytes.

\* Chl = Total HPLC-derived chlorophyll-*a* concentration (mg m<sup>-3</sup>) attributed to each taxa, % Chl = percent total HPLC-derived chlorophyll-*a* attributed to each taxa, Biovol = Total IFCB-derived biovolume (μL L<sup>-1</sup>) attributed to each taxa, and % Biovol = percent total IFCB-derived biovolume attributed to each taxa.

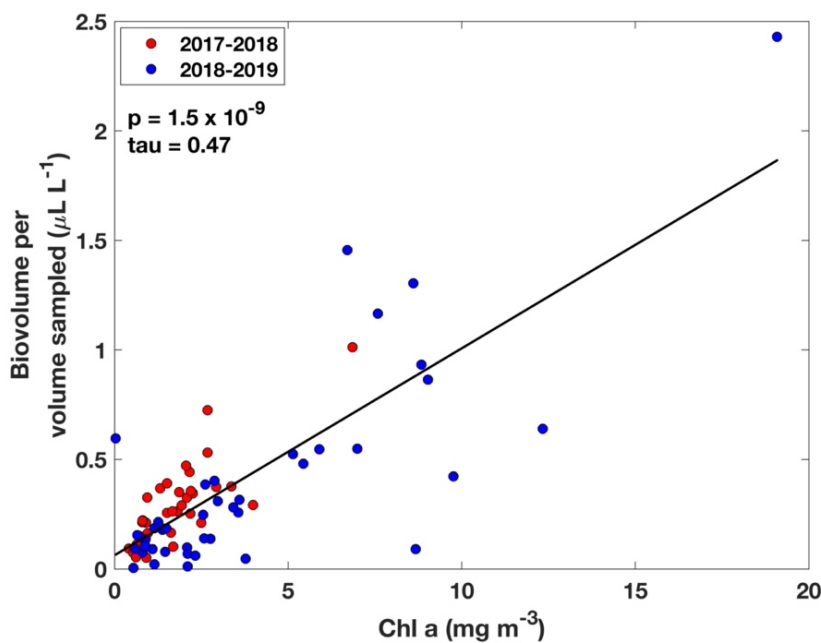
### 3.10 Supplementary figures



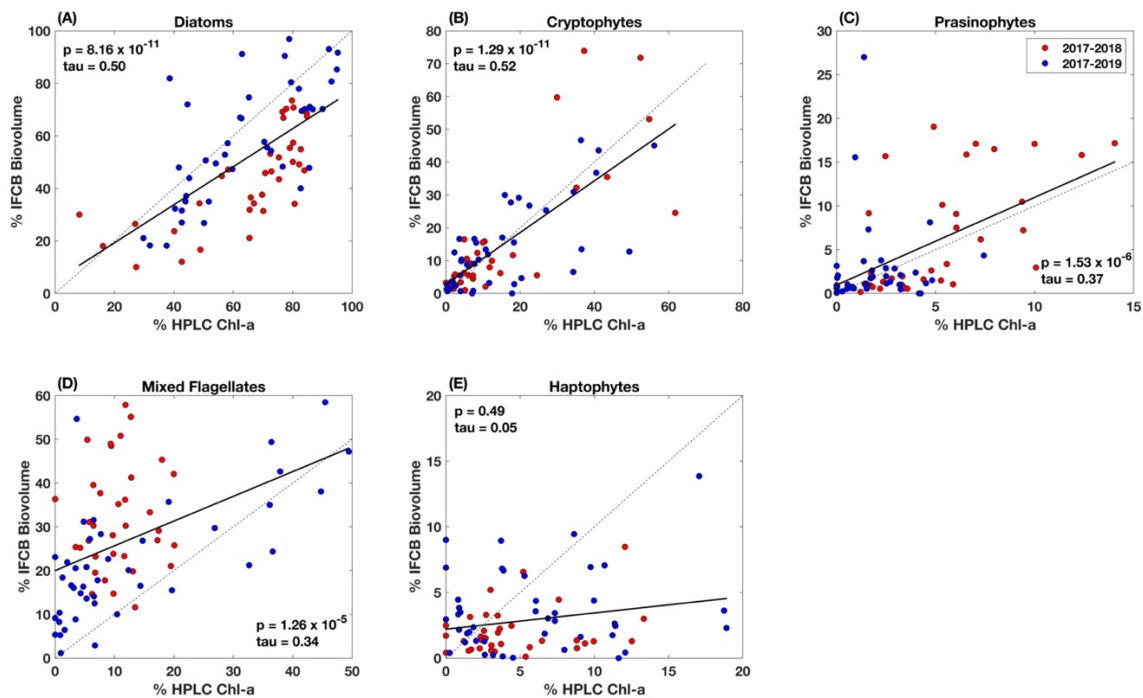
**Supplementary Figure 1.** Comparison of live versus preserved IFCB samples for (A) total biovolume, (B) total cell density, and (C-E) percent biovolume for each broad taxonomic group for (C) 22 December 2017, (D) 26 December 2017, and (E) 28 December 2017. Comparisons were conducted using surface samples at Station B.



**Supplementary Figure 2.** Seasonal percent composition derived from the IFCB for cryptophytes and diatoms in **(A)** 2017-2018 and **(B)** 2018-2019, showing seasonal phytoplankton successional phase divisions (vertical dashed lines; IR = Ice Retreat Phase, PS = Peak Summer Phase, and LS = Late Summer Phase).



**Supplementary Figure 3.** HPLC-derived chlorophyll-*a* concentration compared to IFCB-derived phytoplankton biovolume for each sampling day in each season. The black line indicates the linear fit between the two variables, and the Kendall  $p$  and  $\tau$  values for that fit are indicated on the figure.



**Supplementary Figure 4.** Percent of total HPLC-derived chlorophyll-*a* compared to percent of total IFCB-derived phytoplankton biovolume in each sample for broad taxonomic groups: (A) diatoms, (B) cryptophytes, (C) prasinophytes, (D) mixed flagellates, and (E) haptophytes. For each subplot, the black dashed line shows the 1:1 relationship and the black solid line indicates the linear fit between the two variables. Kendall  $p$  and  $\tau$  values for each linear fit are also indicated on each subplot.

## **4. Assessing ecological drivers of phytoplankton bloom phenology in coastal Antarctica**

### **4.1 Abstract**

West Antarctic Peninsula (WAP) coastal waters are characterized by large phytoplankton blooms that support a productive ecosystem and impact regional carbon biogeochemistry. Bloom phenology is driven by bottom-up processes that impact division rates and top-down processes including grazing that impact loss rates. Quantifying seasonal phytoplankton division and loss rates is important for understanding changes in lower trophic level dynamics. Autonomous underwater glider deployments from 2008-2020 were used to model summer phytoplankton bloom dynamics near Palmer Station, Antarctica. Climatologies were calculated for phytoplankton accumulation, division, and loss rates, which were compared to bottom-up (light and nutrients) and top-down (grazing) controls to identify ecological drivers. Two distinct seasonal phases were detected: (1) December and January were characterized by high light and shallow mixed layers that concentrated phytoplankton allowing grazers to keep pace with phytoplankton division rates and resulting in generally stable biomass with a small mixotrophic cryptophyte bloom; (2) February and March were characterized by decreasing light and increasing wind speeds that deepened the surface mixed layer and resuspended sedimentary iron to fuel a large, autumn bloom. Our results indicate that environmental changes along the WAP (e.g., warming temperatures, melting sea ice and glaciers, increased cloudiness, and more frequent storms) are likely to impact both bottom-up and top-down controls of bloom phenology, shifting the species composition and timing of these blooms and thereby altering food web structure and function.

## 4.2 Introduction

Southern Ocean phytoplankton play an important role in regulating global climate, and are responsible for 43% of global ocean sequestration of anthropogenic CO<sub>2</sub> (Frölicher et al. 2015). Around 10% of this sequestered CO<sub>2</sub> makes it to the deep ocean (>1000 m) via vertical transport (the biological pump) to be stored for thousands of years (Eppley and Peterson 1979; Passow and Carlson 2012). Changes in phytoplankton bloom dynamics and community structure have important implications for biological pump efficiency (Brown et al. 2019).

The coastal waters of the West Antarctic Peninsula (WAP) are characterized by large, seasonal phytoplankton blooms that support a productive ecosystem (Ross et al. 1996). The WAP is currently undergoing significant change, with air and ocean temperatures increasing by >5°C and >1°C since 1951, respectively (Meredith and King 2005; Turner et al. 2005), and concurrent decreases in sea ice extent and duration (Stammerjohn et al. 2008b). In addition, the northern WAP has experienced increased wind speeds and cloudiness, and decreased phytoplankton biomass associated with a shift to smaller cells (Montes-Hugo et al. 2009).

Understanding how these environmental changes impact phytoplankton bloom phenology is critical for assessing future health and productivity of coastal WAP ecosystems.

Phytoplankton bloom dynamics are balanced by bottom-up controls (e.g., nutrients and light) that impact division rates, and top-down (e.g., grazing) and other processes (e.g., sinking, advection) that impact loss rates (Behrenfeld 2010). Light limitation is the primary control of phytoplankton growth rates in the Southern Ocean, explaining 66% of growth rate variability (Arteaga et al. 2020). The light conditions that

phytoplankton experience are a combination of incoming solar radiation (e.g., seasonal variation in daylength and weather), how deep into the water column the incoming radiation penetrates (e.g., changes in the diffuse attenuation coefficient), and the depth of the surface mixed layer (driven by wind-mixing, water mass properties, surface warming and freshening, etc.). Phytoplankton adapt to changing light conditions (photoacclimation) via changes in cellular physiology in an attempt to balance photosynthetic electron transport with metabolic demands (i.e., nutrient uptake; Kana et al. 1997). Physiological changes include altering the size of the light harvesting antenna of reaction centers, or changing the total number of reaction centers (Falkowski and Laroche 1991). The result is a change in cellular chlorophyll concentration— high light results in a decrease in chlorophyll synthesis, and low light results in an increase in chlorophyll synthesis. Increasing light and nutrients lead to higher cell division rates until they saturate, and decreasing light and nutrients decrease division rates (Geider and La Roche 1994; Arteaga et al. 2016; Behrenfeld et al. 2016).

Loss rates can include grazing, advection, and sinking. Overall grazing rates along the WAP vary interannually and seasonally with shifts in zooplankton communities. In nearshore and shelf waters, dominant macrozooplankton taxa (krill *Euphausia superba*, *Thyanoessa macrura*, *Euphausia crystallorophias*; the salp *Salpa thompsoni*; and the pteropod *Limacina helicina*) remove <1% of primary production when salps are not blooming, and up to 169% of primary productivity during salp blooms (Bernard et al. 2012). In comparison, copepods remove <1 to 11% of primary production (Gleiber et al. 2016), and microzooplankton usually remove between 30 to 70% of primary production (Garzio et al. 2013). Advection rates vary depending on location, however in the Palmer

Deep canyon region (located at the southern end of Anvers Island in the northern WAP), surface residence times are correlated to wind strength, with higher wind speeds associated with lower residence times (Kohut et al. 2018). Surface residence times reach a maximum of 5 days (Kohut et al. 2018), while models show that shallow residence times (< 20 m) reach a maximum of 20 days, and residence times at 50 m reach a maximum of 30 days (Hudson et al. 2021).

The goals of our study were to model summer phytoplankton bloom phenology in the coastal WAP and identify the ecological drivers of seasonal rate changes. To do this, we used 12 years of autonomous underwater glider data collected in the Palmer Deep canyon over various periods of the austral summer to calculate high-resolution (1-day) climatologies of phytoplankton accumulation, division, and loss rates. These were compared to bottom-up and top-down forcings. Results showed a transition in phytoplankton photophysiology between January and February driven by decreases in the light regime, wind-driven mixing, and decreased zooplankton grazing pressure. These results suggest that long-term environmental changes along the WAP (e.g., increased cloudiness, increased wind speeds, increased surface warming and ice melt) are likely to impact the timing, species composition, and cell size dynamics of seasonal phytoplankton blooms, in turn altering food web structure and carbon biogeochemistry.

## **4.3 Methods**

### *4.3.1 Glider data collection*

Data was collected using Slocum gliders deployed from Palmer Station, Antarctica during austral summer field seasons from 2008-2020 (Table 1 and Fig. 1),

encompassing 13,071 profiles collected over 436 days during 30 deployments. These deployments were part of the Palmer Antarctica Long-Term Ecological Research Project (PAL-LTER; 2010-2019), Project CONVERGE (2014-2015) and Project SWARM (2019-2020). Gliders are buoyancy-driven, autonomous underwater vehicles that provide high-resolution measurements of physical and bio-optical properties in the water column. Our analysis includes all available concurrent physical and biological glider profiles in the Palmer Deep canyon. Each glider was equipped with a Sea-Bird Conductivity-Temperature-Depth (CTD) sensor and a WET Labs Inc. Environmental Characterization Optics (ECO) puck, which measured chlorophyll-*a* fluorescence and optical backscatter ( $\beta$ ; see Table 1 for backscatter wavelengths of each puck), and data was binned into 1 m-depth increments prior to analysis. Glider CTD measurements were compared with a calibrated ship CTD sensor on deployment and recovery to ensure data quality, as well as with a calibrated laboratory CTD prior to deployment. Glider chlorophyll-*a* fluorescence and  $\beta$  were converted from raw counts using the factory calibration scale factor and dark counts. If >1% of chlorophyll-*a* fluorescence or  $\beta$  values were negative, the dark count was iteratively decreased until <1% of computed values were negative (Woo and Gourcuff 2021). Chlorophyll-*a* fluorescence values were corrected for non-photochemical quenching using methods in Xing et al. (2012).

Particulate spikes in  $\beta$  profiles were removed using a 7-point running median filter (Briggs et al. 2011). Values were then converted to particulate backscattering coefficients using the equation in Boss and Pegau (2001):

$$b_{bp} = 2\pi\chi\beta_p(\theta) ,$$

where  $\beta_p$  is total measured  $\beta$  minus the filtered sea water contribution (Zhang and Hu 2009) for the given sensor centroid angle indicated in Table 1, and  $\chi$  is the particulate conversion value for that angle (Sullivan et al. 2013). Depending on the backscatter sensor,  $\beta$  was measured at either 470 nm or 700 nm (Table 1), so an additional step was used to convert  $b_{bp}(700)$  to  $b_{bp}(470)$  for uniformity in our analysis:

$$b_{bp}(470) = b_{bp}(700) \times \frac{470^{-0.78}}{700},$$

where -0.78 is a global estimate of particle size index ( $\gamma$ ) by Boss et al. (2013).

#### 4.3.2 *Mixed layer depth calculations*

The seasonal mixed layer depth (MLD) was calculated from profiles of temperature and salinity according to Carvalho et al. (2017) and is based on the depth of the maximum buoyancy frequency ( $\max(N^2)$ ). A quality index value (QI; Lorbacher et al. 2006) was calculated for each vertical profile and was used to filter out profiles without a well-defined surface mixed layer above the calculated MLD ( $QI < 0.5$ ). Chlorophyll-*a* was averaged and integrated over the MLD ( $Chl_{avg}$  ( $mg\ m^{-3}$ ) and  $Chl_{int}$  ( $mg\ m^{-2}$ ), respectively), and daily averages of MLD,  $Chl_{avg}$ , and  $Chl_{int}$ , were computed prior to calculating phytoplankton growth, loss, and accumulation rates to reduce spatial variation.

### 4.3.3 *Palmer Station weather data*

Wind speed ( $\text{m s}^{-1}$ ; RM Young, Model 05108-45) and surface photosynthetically available radiation (PAR) measurements for 400-700 nm ( $\text{mol photons m}^{-2} \text{ h}^{-1}$ ; LI-COR model LI-190SA quantum sensor) were obtained from an automated weather station located just behind Palmer Station. Daily averages were calculated from 2-minute data for both variables. There were no PAR data collected from 1 March 2019 to the end of our sampling period (31 March 2020) due to a wiring issue; however, the weather station also collected total incoming solar irradiance ( $\text{W m}^{-2}$ ) collected by a LI-COR model LI-200SA pyranometer during the entire sample period (1 October 2010 – 31 March 2020). Therefore, the linear relationship between PAR and solar irradiance for the period of overlap (1 October 2010 – 1 March 2019;  $y = 0.01x + 0.06$ ,  $R^2 = 0.94$ ,  $p < 0.0001$ ; see Supplementary Fig. 1) was used to fill in missing PAR values.

### 4.3.4 *Phytoplankton division, accumulation, and loss rates*

The WAP undergoes dramatic seasonal changes in sunlight, and phytoplankton acclimate via physiological responses. Decreases in light (e.g., a deepening mixed layer depth) often lead to an increase in cellular chlorophyll concentrations and a concurrent decrease in division rates, and increases in light (e.g., a shallowing mixed layer depth) often lead to decreases in cellular chlorophyll due to high-light acclimation (Fox et al. 2020). Thus, photoacclimation should be taken into consideration when calculating phytoplankton division rates in our region. We used a photoacclimation model (PaM) from Behrenfeld et al. (2016), which takes into account deep and shallow mixing

scenarios to calculate phytoplankton carbon biomass ( $C_{\text{phyto}}$ ) to chlorophyll-*a* ratios ( $\theta_{PaM}$ ):

$$\theta_{PaM} = \theta_{DM} \Delta\theta_{SM}, \text{ whereby}$$

$$\theta_{DM} = 19 \cdot e^{(0.038 \cdot \frac{PAR^{0.45}}{k(490)})} \text{ and } \Delta\theta_{SM} = \frac{1 + e^{(-0.15 \cdot PAR)}}{1 + e^{(-3 \cdot I_g)}},$$

$k(490)$  is the diffuse attenuation coefficient at 490 nm ( $\text{m}^{-1}$ ) calculated as (Morel et al. 2007):

$$k(490) = 0.0166 + 0.0773 \cdot Chl_{avg}^{0.6715},$$

and  $I_g$  is the daily mixed layer median light level ( $\text{mol photons m}^{-2} \text{h}^{-1}$ ) calculated as (Behrenfeld et al. 2005):

$$I_g = PAR \cdot \exp^{-k(490) \cdot \frac{MLD}{2}}.$$

Phytoplankton specific division rates,  $\mu$  ( $\text{d}^{-1}$ ) for the mixed layer were then calculated for each day (Fox et al. 2020):

$$\mu = \left[ \left( \frac{1}{\theta_{DM}} \cdot (-16.80) + 1.57 \right) \cdot \left( \frac{1}{\theta_{PaM}} \cdot (47.03) + 0.0125 \right) \right] \cdot [1 - e^{(-5 \cdot PAR)}],$$

and MLD-averaged and -integrated  $C_{\text{phyto}}$  ( $C_{\text{avg}}$  and  $C_{\text{int}}$ , respectively) were subsequently calculated by multiplying  $\theta_{\text{PaM}}$  by  $\text{Chl}_{\text{avg}}$  or  $\text{Chl}_{\text{int}}$ , respectively.

Phytoplankton specific net accumulation rates,  $r$  ( $\text{d}^{-1}$ ), were calculated for the mixed layer depth from temporal changes in  $C_{\text{phyto}}$  between two time points (Behrenfeld et al. 2013):

$$r = \frac{1}{\Delta t} \cdot \ln \left( \frac{C_{\text{int},t1}}{C_{\text{int},t2}} \right), \text{ when MLD is deepening and } > Z(0.415)$$

$$r = \frac{1}{\Delta t} \cdot \ln \left( \frac{C_{\text{avg},t1}}{C_{\text{avg},t2}} \right), \text{ when MLD is shoaling or } < Z(0.415).$$

$Z(0.415)$  is the isolume depth (m), below which light is insufficient for photosynthesis ( $I = 0.415 \text{ mol photon m}^{-2} \text{ d}^{-1}$ ; Letelier et al. 2004), and is calculated as (Boss and Behrenfeld 2010):

$$Z(0.415) = \log \left( \frac{0.415}{0.98 \times PAR} \right) \cdot \left( \frac{Z_{eu}}{\log(0.01)} \right),$$

and  $z_{eu}$  is the depth at which light is 1% of its surface value and is calculated from the equation in Morel et al. (2007):

$$\log_{10}(Z_{eu}) = 1.524 - 0.436x - 0.0145x^2 + 0.0186x^3, \text{ where } x = \log_{10}(\text{Chl}_{\text{surface}}).$$

$\Delta t$  was typically 1 since we used daily-averaged measurements, but there were occasional gaps in measurements that increased this value to 2 or 3. Finally, phytoplankton specific

loss rates,  $l$  ( $\text{d}^{-1}$ ) for the mixed layer were calculated by subtracting  $r$  from  $\mu$ , because  $r = \mu - l$ .

#### 4.3.5 Station E data

Annual sample collection at Palmer Station, Antarctica (Fig. 1) has been conducted by the PAL-LTER since 1991 at two locations: an inshore station (B, bottom depth of  $\sim 75$  m) and an offshore station (E; bottom depth of  $\sim 200$  m). These stations are sampled twice a week from when the sea ice breaks up enough to allow small boat activity ( $\sim$ mid-October/November) to late March. Inclement weather and heavy sea ice can limit sampling in this region, leading to occasional gaps in our dataset. Glider deployments begin a bit later ( $\sim$ December) because open water conditions (minimal to no sea ice) are necessary for successful remote piloting.

Because the gliders over the Palmer Deep Canyon sampled closer to the offshore station, nutrient and pigment data collected at Station E were used in our analysis, obtained from the Palmer LTER web portal (<http://pallter-data.marine.rutgers.edu/erddap/index.html>). Methods for nutrient analysis can be found in Kim et al. (2016), and methods for pigment analysis can be found in Schofield et al. (2017). Nitrate, phosphate, and silicate concentrations were integrated over the surface 50 m for each sampling day. Output taxa proportions for each pigment-derived phytoplankton group (diatoms, cryptophytes, prasinophytes, haptophytes and mixed flagellates including both dinoflagellates and other phytoflagellates) were averaged over the surface 50 m for each sampling day.

#### 4.3.6 *Climatology calculations*

Seasonal climatologies from 1 December to 15 March were created using all available glider data from 2008 to 2020, excluding one January 2014 deployment (ru01-403) due to anomalously high chlorophyll-*a* concentrations (Supplementary Fig. 2). First, daily averages were calculated for all variables (wind speed, MLD, PAR,  $I_g$ ,  $Chl_{avg}$ ,  $C_{avg}$ ,  $b_{bp}(470)$ , and phytoplankton division, loss, and accumulation rates) for each year, then, these annual daily averages were averaged across all years. Because Station E was sampled bi-weekly, weekly averages of nutrients and phytoplankton pigments were calculated for each year before averaging across all years. All climatologies were smoothed with a 3-point moving mean.

#### 4.3.7 *Statistical analyses*

To compare monthly climatological differences, seasonal climatology values were binned by month (December through March, with March only including 1 March – 15 March due to glider data coverage) for each variable. One-way analysis of variance (ANOVA) tests were used to determine if there were significant differences between months, and Tukey-Kramer post-hoc tests were subsequently used to show which months had significantly different means.

## 4.4 Results

### 4.4.1 *Modeled $C_{phyto}$*

PaM-derived  $C_{phyto}$  values (ranging from 38.75 to 241.75 mg m<sup>-3</sup>) were much higher than widely used optical models that calculate  $C_{phyto}$  from linear relationships with

$b_{bp}$  obtained from global satellite (Behrenfeld et al. 2005) and cruise (Graff et al. 2015) measurements (ranging from 19.48 to 101.80 mg m<sup>-3</sup>; Fig. 3). Additionally, there were seasonal patterns in the slope of our  $b_{bp}(470)$  and  $C_{phyto}$  relationship, with the steepest slope found in February, followed by December and January, and no significant relationship found in March (Fig. 3).

#### 4.4.2 *Seasonal climatology*

We saw distinct seasonal shifts in our environmental climatologies from the early (December and January) to late (February and March) summer. Wind speeds decreased from a maximum of 5.19 m s<sup>-1</sup> in early December to values < 3 m s<sup>-1</sup> in early January, then rose to significantly higher values in February and March (maximum wind speeds > 5 m s<sup>-1</sup>; Fig. 4A and 5A). In response, MLDs were variable but shallow (~10 to 30 m) in December and January, significantly deepening to 30 to 40 m in February, and significantly shallowing to ~20 to 30 m in March with increased glacial meltwater inputs (Fig. 4B and 5B; Carvalho et al. 2016). PAR and  $I_g$  were high and variable throughout December and January (mean = 1.39 mol photons m<sup>-2</sup> h<sup>-1</sup> and 0.35 mol photons m<sup>-2</sup> h<sup>-1</sup>, respectively), and decreased significantly in February and March (mean = 0.90 mol photons m<sup>-2</sup> h<sup>-1</sup> and 0.11 mol photons m<sup>-2</sup> h<sup>-1</sup>, respectively; Fig. 4C and 5C). Nitrate, phosphate, and silicate all decreased from December to February (from 1547.41 to 1058.92, 89.40 to 74.99, and 3848.69 to 3003.60, respectively), and then increased slightly from February to mid-March (up to 1170.50, 78.76, and 3068.47, respectively; Fig. 4D-F and 5D-F).

Similar shifts were observed in phytoplankton seasonal dynamics. MLD-averaged chlorophyll-*a* and  $C_{\text{phyto}}$  closely mirrored each other, with a moderate bloom in late December reaching maximum concentrations of 7.84 mg Chl-*a* m<sup>-3</sup> and 195.88 mg C m<sup>-3</sup>, respectively, and a large bloom in February with significantly higher chlorophyll-*a* and  $C_{\text{phyto}}$  concentrations than other months, reaching 9.77 mg Chl-*a* m<sup>-3</sup> and 205.24 mg C m<sup>-3</sup>, respectively (Fig. 6A and 7A-B). Chlorophyll-*a*:b<sub>bp</sub>(470) ratios showed significant increases from December to January (December mean = 863.61, January mean = 1171.18) and January to February (January mean = 1171.18, February mean = 1923.84; Fig. 6B and 7C). These dynamics reflected shifts in phytoplankton species composition, primarily between relative diatoms and cryptophyte abundance as the relative proportion of mixed flagellates and Type 4 Haptophytes remained consistent over time. In early December, diatoms and cryptophytes comprised approximately 77% and 8% of the chlorophyll-*a* biomass, respectively, shifting to 41% diatoms and 35% cryptophytes in mid-January, and back to 77% diatoms and 3% cryptophytes by early March (Fig. 6C).

Phytoplankton specific division and loss rates were low and variable in December and January (mean = 1.42 d<sup>-1</sup> and 1.40 d<sup>-1</sup>, respectively), increasing significantly in February with the bloom (mean = 1.56 d<sup>-1</sup> and 1.58 d<sup>-1</sup>, respectively), and decreasing again in March (mean = 1.40 d<sup>-1</sup> and 1.38 d<sup>-1</sup>, respectively; Fig. 6D and 7D-E). Accumulation rates showed no significant monthly differences (ANOVA  $p = 0.82$ ) but showed both a decrease in variability over time (December range = 1.29, January range = 0.84, February range = 0.57, and March range = 0.53; Fig. 6E), and a significant increase in the cumulative sum of accumulation rates from December to January (Fig 6F and 7F).

## 4.5 Discussion

### 4.5.1 Seasonal bloom phenology

The Disturbance and Recovery Hypothesis (Behrenfeld et al. 2013) states that blooms form when an environmental disturbance disrupts the balance between the phytoplankton specific growth and loss rates, and blooms terminate as ecosystem feedbacks recouple predators and prey. This hypothesis describes seasonal phytoplankton dynamics in four phases (Behrenfeld et al. 2019): (1) the Accumulation Phase in spring when the mixed layer shoals, light levels increase, and phytoplankton division rates exceed loss rates leading to positive biomass accumulation rates; (2) the Equilibrium Phase in summer, when a shallow mixed layer concentrates predators, allowing loss rates to catch up to division rates and stabilizing phytoplankton biomass; (3) the Depletion Phase in late summer into autumn, when the mixed layer deepens, light levels decrease, and division and accumulation rates decline; and (4) the Dilution Phase in winter, when deep mixing reduces the encounter rate between phytoplankton and grazers, allowing division rates to exceed loss rates and initiating a bloom. Because we only have summer climatologies of division and loss rates, we cannot fully assess the validity of this hypothesis in our study region, however, our data appear to capture parts of both the Equilibrium Phase in December and January, and the Depletion Phase in February and March.

In the austral spring (October to November), increasing solar irradiance and sea ice retreat alleviates light limitation and stabilizes the upper water column, shoaling the MLD and restricting phytoplankton to well-lit and nutrient replete surface waters (Vernet et al. 2008; Ducklow et al. 2013; Venables et al. 2013; Kim et al. 2016). These conditions

allow for phytoplankton division rates to increase significantly, outpacing loss rates and leading to a huge, large-celled diatom bloom that reflects the culmination of the Accumulation Phase (Chapter 3; Behrenfeld et al. 2013). Unfortunately, we are missing this phase in our analysis due to difficulties navigating gliders in icy waters.

However, austral summer (December and January) reveals post-bloom conditions that match the Equilibrium Phase, where continued stratification with decreasing wind speeds and high PAR correspond with increases in grazers, allowing loss rates to catch up to growth rates (Behrenfeld et al. 2013). This is reflected in the net losses seen in December (negative cumulative sum of accumulation rates; Fig. 6F and 7F), and the shallower slope in the  $C_{\text{phyto}}:b_{\text{bp}}(470)$  relationship that indicates the presence of non-algal scatters like zooplankton, bacteria, detritus, etc. (Fig. 3). The bloom we see in late December also has a high proportion of cryptophytes (Fig. 6C), which are mixotrophs and likely flourish with post-bloom detritus (Gast et al. 2014; Trefault et al. 2021). Additionally, WAP cryptophytes are well-suited to high light levels due to specialized protective pigments (Mendes et al. 2017), and high PAR conditions allow mixotrophs to supplement their carbon supply with photosynthesis, driving prey to low densities and outcompeting heterotrophs (Edwards 2019).

In February and March, the system switches to the Depletion Phase, where increasing winds deepen the MLD and decrease  $I_g$  levels, often corresponding with decreased phytoplankton specific division and loss rates (Behrenfeld et al. 2013). However, autumn blooms can occur during this phase, as seen in our study, if there are increases in the nutrient supply or a dilution effect that decreases grazing pressure (Behrenfeld et al. 2013). In February, we saw a large bloom and concurrent increases in

division rates (Fig. 6A and 6D). This bloom is likely dominated by small pennate diatoms (Fig. 6C; Chapter 3), which are known to have very fast growth rates (Behrenfeld et al. 2021b). Since  $I_g$  is low, these increases in division rates are likely spurred by increases in nutrients. In the Palmer Deep canyon, iron supply primarily comes from shallow sediments delivered to the surface waters by wind-driven vertical mixing (Sherrell et al. 2018). In the one summer of iron data that was collected in the region (January to March 2015), surface iron concentrations spike from  $\sim 1 \text{ nmol kg}^{-1}$  to  $7 \text{ nmol kg}^{-1}$  in early February corresponding with increasing wind speeds and MLD deepening (Carvalho et al. 2016). We see a slight increase in macronutrient data from February to March that could support this hypothesis (Fig. 5D-5F). The increase in Chl:b<sub>bp</sub>(470) is likely driven by both photoacclimation, where decreases in light increase chlorophyll synthesis (Kana et al. 1997), and nutrient-driven increases in growth rates, resulting in the synthesis of chlorophyll to help with ATP and NADPH production (Behrenfeld et al. 2016). The termination of the February bloom, decreasing growth rates, and decreases in the cumulative sum of accumulation rates co-occur with the shoaling of the MLD, indicating reduced wind-driven mixing of iron to surface waters, and increased concentrations of grazers within the MLD.

Previous work has shown a decreasing trend in phytoplankton cell size throughout the summer growing season (Chapter 3). This matches seasonal decreases in light and nutrient availability. Larger cells are less susceptible to photoinactivation due to excessive light energy, and therefore are better suited to deal with short-term exposure to high light conditions than small cells (Key et al. 2010). On the other hand, small cells have larger effective optical cross-sections, which makes them better suited for low light

conditions (Key et al. 2010). Smaller cells also have a greater surface area to volume ratio allowing more efficient nutrient uptake in nutrient-poor environments (Finkel et al. 2010). Thus, as PAR and nutrients decrease from December through March, cell size is likely to decrease as well. Smaller cells typically exhibit faster growth rates (Finkel et al. 2010), however this could be counteracted by declining light and nutrient availability in the late summer.

#### 4.5.2 *Phytoplankton specific division and loss rates*

There are limited estimates of phytoplankton division rates along the WAP that we can compare our results to. Moline (1996) found rates of 0.01-0.1 d<sup>-1</sup>, while Garzio et al. (2013) found rates up to 0.99 d<sup>-1</sup>. These are both lower than the division rates in our study that ranged from 1.01 to 1.73 d<sup>-1</sup>. However, our results fall within the range of other Antarctic studies, which found division rates ranging from 0.11 to 2.6 d<sup>-1</sup> (See Table 2 in Garzio et al. (2013) and references therein). It is possible that our division rates are skewed high due to potential biases in the models we used. The equations to calculate  $\theta_{PaM}$  and our division rates both depend on global estimates and laboratory experiments that may not be representative of productive, coastal regions (Behrenfeld et al. 2016; Fox et al. 2020). Regional comparisons of PaM-derived and satellite-derived  $C_{phyto}:Chl$  ratios found lower PaM-derived ratios for the South Pacific (the closest region to Antarctica tested; Behrenfeld et al. 2016). In the equation used to calculate division rates (Fox et al. 2020), PaM-derived  $C_{phyto}:Chl$  ratios are in the denominator, so an underestimate of  $C_{phyto}:Chl$  could overestimate phytoplankton division rates. In the future, the model could be adapted to reflect the conditions of coastal Antarctica, but for the purposes of this

study, these models provide reasonable estimates of division rates that reflect important seasonal trends.

While bottom-up drivers of phytoplankton growth rates (e.g., light and nutrients) have been consistently measured by PAL-LTER in our region, loss rates such as grazing and advection have received far less attention. Only a few studies have looked at grazing rates along the WAP (see Introduction), and the total grazing rate is variable depending on the species that are present at a particular time and location. The highest grazing rates (up to 169% of primary production; Bernard et al. 2012) occur during salp blooms, which are not present in the Palmer region in every year and whose grazing impact is likely averaged out in our loss rate climatology. In years without salps, macrozooplankton graze <1% of primary production (Bernard et al. 2012), copepods graze up to 11% (Gleiber et al. 2016), and microzooplankton graze ~30 to 70% (Garzio et al. 2013), resulting in a remaining ~20% of primary production that could be put towards phytoplankton biomass accumulation.

Life cycle dynamics of zooplankton species also play a role in grazing rates. In summer, *E. superba* krill adult populations concentrate near the shelf break, while juveniles are most abundant inshore (Siegel et al. 2013; Conroy et al. 2020). In early autumn, adult krill move inshore and deeper in the water column to utilize deep food resources in troughs and canyons during the winter (Cleary et al. 2016; Reiss et al. 2017; Nardelli et al. 2021a), while juvenile and larval krill remain shallow to feed on under-ice algae (Bernard et al. 2018; Walsh et al. 2020). Juvenile krill have higher grazing rates than adult krill due to higher metabolic rates and lower lipid stores (Schmidt and Atkinson 2016). Therefore, following strong recruitment years, coastal regions may have

higher summertime krill grazing rates. As adult krill move inshore in autumn, this could add to coastal grazing pressures, however, their deeper location in the water column and more diverse diet (e.g., copepods and seabed phytodetritus) might lessen this impact (Polito et al. 2013; Schmidt et al. 2014).

The other main sources of loss (advection and sinking) are physical processes. Based on studies from the Palmer Deep canyon, particle residence times within the mixed layer are between 2 and 30 days (Kohut et al. 2018; Hudson et al. 2021). This means that ~3% to 20% of phytoplankton biomass is lost from the canyon via advection each day. Based on our growth rates of 1.01 to 1.73 d<sup>-1</sup>, doubling times are between 0.40 to 0.68 days, which means phytoplankton biomass can double at least 7.35 to 12.5 times before the phytoplankton particles are advected out of the Palmer Deep canyon (assuming a residence time of 5 days). Loss rates due to sinking will vary over the field season, with faster rates in the late spring when large phytoplankton species are present, and slower rates in the late summer when smaller species are present (Finkel et al. 2010), unless facilitated by repackaging of cells through zooplankton ingestion/egestion. However, sinking rates are complicated further by the strength of vertical mixing, and strong stratification in the late spring could impede sinking, while increases in wind-mixing in late summer could accelerate sinking.

#### 4.5.3 *Relationship between $C_{phyto}$ and $b_{bp}(470)$*

$C_{phyto}$  values derived from optical algorithms using  $b_{bp}$  do not appear to work well in coastal Antarctica (Fig. 3). The high productivity of this region, with large, seasonal and sometimes episodic blooms during austral summer, led to chlorophyll and backscatter values much higher than those used in previous optical algorithms.

Behrenfeld et al. (2005) and Graff et al. (2015)'s models use chlorophyll-*a* values ranging from 0.14 to 0.80 mg m<sup>-3</sup> and 0.026 to 1.13 mg m<sup>-3</sup>, respectively, while our study's values ranged from 1.21 to 10.03 mg m<sup>-3</sup>. Similarly, Behrenfeld et al. (2005) and Graff et al. (2015)'s models use  $b_{bp}(470)$  values ranging from 0.0012 to 0.005 m<sup>-1</sup> and 0.00046 to 0.0038 m<sup>-1</sup>, respectively, while our study's values ranged from 0.0016 to 0.0083 m<sup>-1</sup>. This discrepancy could account for the underestimation of  $C_{phyto}$  values provided by their algorithms relative to the PaM-derived  $C_{phyto}$ .

Seasonality was another important component in our  $C_{phyto}$  model choice. Optical models, such as in Behrenfeld et al. (2005) and Graff et al. (2015), assume a stable non-algal background component based on global observations. However, the algal contribution to particulate organic carbon (POC), and to  $b_{bp}$ , varies spatially and temporally.  $C_{phyto}$ :POC ratios have been found to be inversely related to productivity (Bellacicco et al. 2016), with algal contributions to total POC ranging from 30-70% in tropical oligotrophic regions and ~10-30% in polar regions and the equatorial Pacific (Arteaga et al. 2016). Backscatter due to non-algal scatters was also found to vary more than one order of magnitude over the course of a year, often closely related to changes in overall phytoplankton biomass (Bellacicco et al. 2016).

A potential cause of reduced  $C_{phyto}$ :POC ratios at high latitudes is the increased ratio of zooplankton to phytoplankton in these productive regions (Ward et al. 2014). At high latitudes, significant decoupling is seen between phytoplankton and zooplankton, where zooplankton abundance lags rapid phytoplankton growth (Ward et al. 2014). Thus, during a phytoplankton boom, a large proportion of the scattering particles is phytoplankton that increases the ratio of  $C_{phyto}$ :POC, and post-bloom, there is an

increased proportion of non-algal scatterers (detritus, zooplankton, bacteria, viruses, etc.) that decrease the  $C_{\text{phyto}}:\text{POC}$  ratio. These dynamics likely drive the observed seasonal patterns in the  $C_{\text{phyto}}:b_{\text{bp}}(470)$  relationship we saw in the Palmer region (Fig. 3), with the steepest slope in February, which contained blooming conditions for over half the month, the next steepest slope in December, which had a bloom at the very end of the month, and the shallowest slope for January, which did not experience a bloom. The high productivity and dynamic seasonal conditions in coastal Antarctica call for a  $C_{\text{phyto}}$  model that relies on local mechanistic drivers of phytoplankton physiology rather than global optical relationships, and Behrenfeld et al. (2016)'s photoacclimation model seemed to produce reasonable  $C_{\text{phyto}}$  estimates that provided useful insight into phytoplankton bloom phenology.

Because we looked at  $b_{\text{bp}}$  rather than POC, coastal  $b_{\text{bp}}$  values could be influenced by non-organic scatterers as well, such as glacial flour. Glacial meltwater is found to increase by 2-8% from November to March (Meredith et al. 2021), releasing particles that have been concentrated within the ice and increasing the turbidity of coastal waters (Dierssen et al. 2002). These particles could increase the non-algal backscattering contribution, reducing  $C_{\text{phyto}}:b_{\text{bp}}$  ratios. However, meltwater particles sink out rapidly as they are transported from shore, with radiance reflectance decreasing by half from Station B to Station E (3.7 km offshore; Dierssen et al. 2002), so glacial flour is unlikely to have a large contribution to  $b_{\text{bp}}$  values beyond the immediate coastal region (e.g., in the Palmer Deep canyon).

#### 4.5.4 Conclusion

Using high resolution glider data, we were able to create climatologies that highlighted persistent seasonal patterns in phytoplankton physiology and bloom phenology. Understanding these seasonal baselines is critical to predicting the impacts of future environmental changes. Following the large spring bloom associated with sea ice retreat, we observed net losses in December and shallow  $C_{\text{phyto}}:b_{\text{bp}}(470)$  slopes in December and January that were indicative of an increased presence of grazers. This suggests a link between the timing of the spring phytoplankton bloom and the rise in heterotrophic and mixotrophic organisms that take advantage of post-bloom conditions. There is a tight coupling between sea ice retreat and the start of the phytoplankton growing season (Chapter 3), and sea ice retreat is trending earlier near Palmer Station (1.28 days per year from 1992-2015; Schofield et al. 2017), which could advance the spring bloom as seen in the broader Southern Ocean (~5-10 days per decade; Henson et al. 2018). This could lead to predator-prey mismatches, where zooplankton grazers may not be able to shift their phenology earlier in response to advancing phytoplankton blooms (Cushing 1990; Edwards and Richardson 2004; Ardyna et al. 2014).

Our results showed phytoplankton physiological responses to changes in light and nutrient availability. In February, the MLD deepened and PAR decreased, yet we saw a surprising increase in phytoplankton biomass, growth rates, and  $\text{Chl}:b_{\text{bp}}(470)$ , likely due to increases in wind-driven iron resuspension (Sherrell et al. 2018). Stronger wind events are predicted to increase in frequency as a result of trends in the Southern Annular Mode and El Niño/La Niña (Hall and Visbeck 2002), which could lead to more frequent iron resuspension events during the summer and subsequent increases in phytoplankton

growth rates and bloom events. The increase in Chl:b<sub>bp</sub>(470) ratios are also indicative of photoacclimation as PAR levels decrease. Wind speeds and cloud cover have increased in the northern WAP from 1978-2006 (Montes-Hugo et al. 2009), which would deepen the MLD and decrease PAR. Long-term changes in light availability could impact phytoplankton species composition and cell size, favoring smaller species with faster growth rates that are better suited to photoacclimation in low light conditions (Key et al. 2010). On the other hand, salp blooms along the WAP have become more frequent (Atkinson et al. 2004), and shifts to smaller phytoplankton cells could increase microzooplankton abundance (Ducklow et al. 2012), both increasing grazing impacts, trophic coupling, and phytoplankton loss rates. Increased grazing potential could curb phytoplankton bloom development, emphasizing the importance of the balance between bottom-up and top-down controls of bloom phenology.

The Antarctic continental shelf comprises a small portion of the Southern Ocean (1.28 million km<sup>2</sup>), yet has disproportionately high primary production rates (mean = 460 mg C m<sup>-2</sup> d<sup>-1</sup>; Arrigo et al. 2008). Phytoplankton blooms along the shelf and coast not only fuel productive coastal ecosystems, but also have outsized impacts on atmospheric carbon sequestration and export. To fully understand these impacts, future studies should focus on capturing a full annual bloom cycle, using technology such as profiling floats or moorings to avoid ice and battery concerns associated with long-term glider deployments, and quantifying loss terms including grazing and advection directly throughout the productive period.

## 4.6 Acknowledgments

Funding for this research came from the NSF Antarctic Organisms and Ecosystems Program (PLR-1440435) as part of the PAL-LTER program, and from NASA (19-IDS19-0085). We appreciate Palmer-based SWARM and CONVERGE projects sharing glider data for this project. Additional thanks to the field teams who helped deploy and recover the gliders and collect Station E timeseries data, and to Palmer Station personnel for supporting data collection and maintaining the weather station.

## 4.7 Tables

**Table 1.** Information on the 30 glider deployments used in analysis. Start and end dates represent dates when the glider was in the Palmer Deep region. Shading indicates deployments within the same summer field season.

Deployment Name	Project	Start Date	End Date	Duration	Backscatter Sensor	Backscatter Wavelength	Backscatter Sensor Angle
ru05-086	LTER	12/13/08	12/22/08	9	BB3	470	124°
ru06-063	LTER	12/02/09	12/17/09	15	BB3	470	124°
ru05-195	LTER	01/08/11	01/12/11	4	BB3	470	124°
ud134-197	LTER	01/10/11	01/14/11	4	FLBBCD	700	124°
ud134-200	LTER	01/16/11	01/31/11	15	FLBBCD	700	124°
ru05-248	LTER	12/14/11	12/28/11	14	BB3	470	124°
ud134-256	LTER	12/21/11	01/02/12	12	FLBBCD	700	124°
ru05-276	LTER	02/16/12	03/01/12	14	BB3	470	124°
ru06-370	LTER	12/07/12	12/09/12	2	BB3	470	124°
ru25d-372	LTER	12/18/12	12/21/12	3	BB2FL	470	124°
ru26d-373	LTER	12/23/12	12/25/12	2	BB2FL	470	124°
ru01-403	LTER	01/04/14	01/16/14	12	BB3	470	124°
ru26d-439	LTER	12/25/14	12/27/14	2	BB2FL	470	124°
ud134-443	CONVERGE	01/05/15	01/21/15	16	FLBBCD	700	124°
unit191-440	CONVERGE	01/05/15	02/26/15	52	FLBBCD	700	124°
ru05-442	CONVERGE	01/06/15	01/14/15	8	BB3	470	124°
ru05-444	CONVERGE	01/15/15	02/01/15	17	BB3	470	124°

ud134-445	CONVERGE	01/22/15	02/15/15	24	FLBBCD	700	124°
ru05-447	CONVERGE	02/01/15	02/08/15	7	BB3	470	124°
ru05-471	LTER	02/02/16	02/17/16	15	BB3	470	124°
ru24-494	LTER	01/17/17	01/30/17	13	BB3	470	124°
ru26d-528	LTER	12/11/17	12/13/17	2	FLBBCD	700	124°
ru25d-530	LTER	12/22/17	12/24/17	2	FLBBCD	700	124°
ru32-555	LTER	01/02/19	01/18/19	16	FLBBCD	700	124°
ud476-594	SWARM	01/05/20	01/25/20	20	FLBB	700	142°
unit507-593	SWARM	01/09/20	02/20/20	42	FLBBCD	700	124°
ru32-595	SWARM	01/11/20	03/11/20	60	FLBBCD	700	124°
ud476-596	SWARM	01/30/20	02/01/20	2	FLBB	700	142°
ud476-598	SWARM	02/04/20	02/10/20	6	FLBB	700	142°
ud476-601	SWARM	02/14/20	03/11/20	26	FLBB	700	142°

## 4.8 Figures

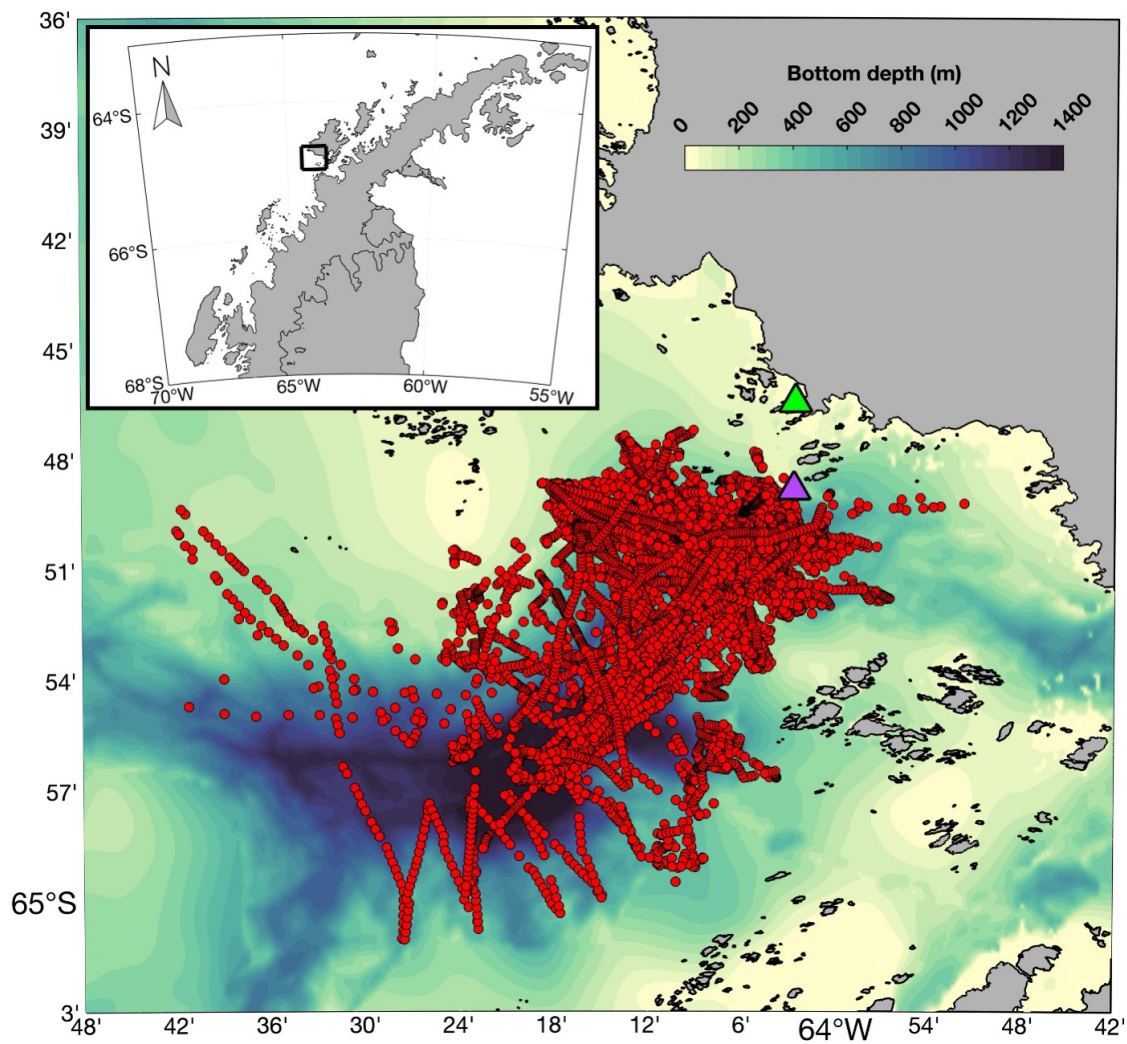


**Figure 1.** Map of the Palmer Deep region, with location along the WAP highlighted by the black box on the inset. Red dots indicate the 13,071 glider profiles used in our analysis, the green triangle marks Palmer Station, and the purple triangle marks Station E.

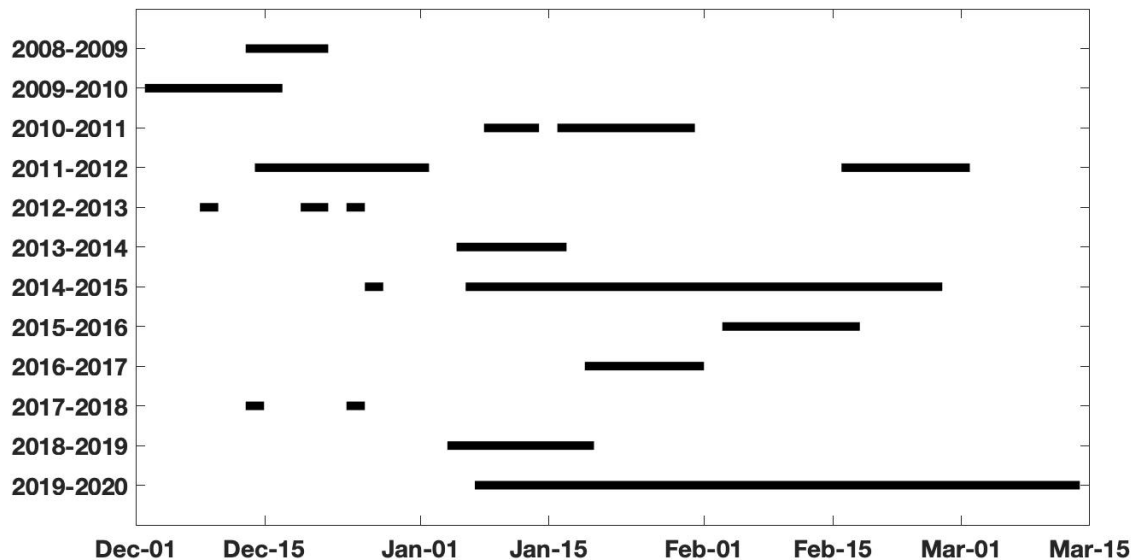


**Figure 2.** Seasonal (December 1 – March 15) coverage of annual glider deployments in the Palmer Deep region.

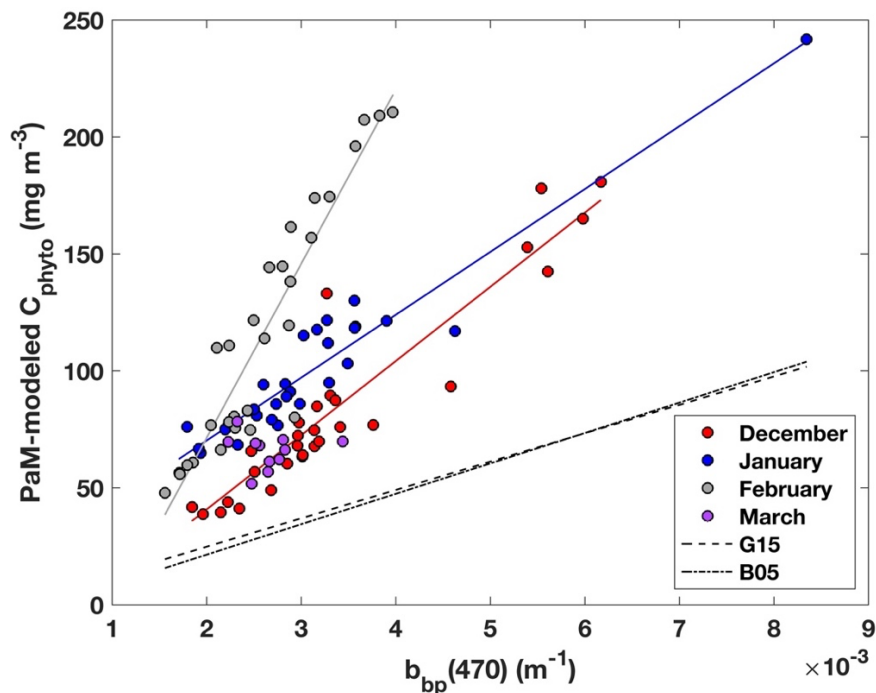


**Figure 3.** Daily climatology values from 2008-2020 of PaM-derived  $C_{\text{phyto}}$  versus  $b_{\text{bp}}(470)$ . The two dashed black lines indicate modeled relationships from Behrenfeld et al. (2005) (B05,  $y = 13000x - 4.55$ ) and Graff et al. (2015) (G15,  $y = 12128x + 0.59$ ). Colored lines represent significant monthly linear relationships between the two variables: December  $y = 31720x - 22.67$ ,  $R^2 = 0.86$ ,  $p < 0.001$ ; January  $y = 26874x + 16.49$ ,  $R^2 = 0.92$ ,  $p < 0.001$ ; February  $y = 74410x - 77.42$ ,  $R^2 = 0.86$ ,  $p < 0.001$ . December  $n = 31$ , January  $n = 31$ , February  $n = 28$ , March  $n = 11$ .

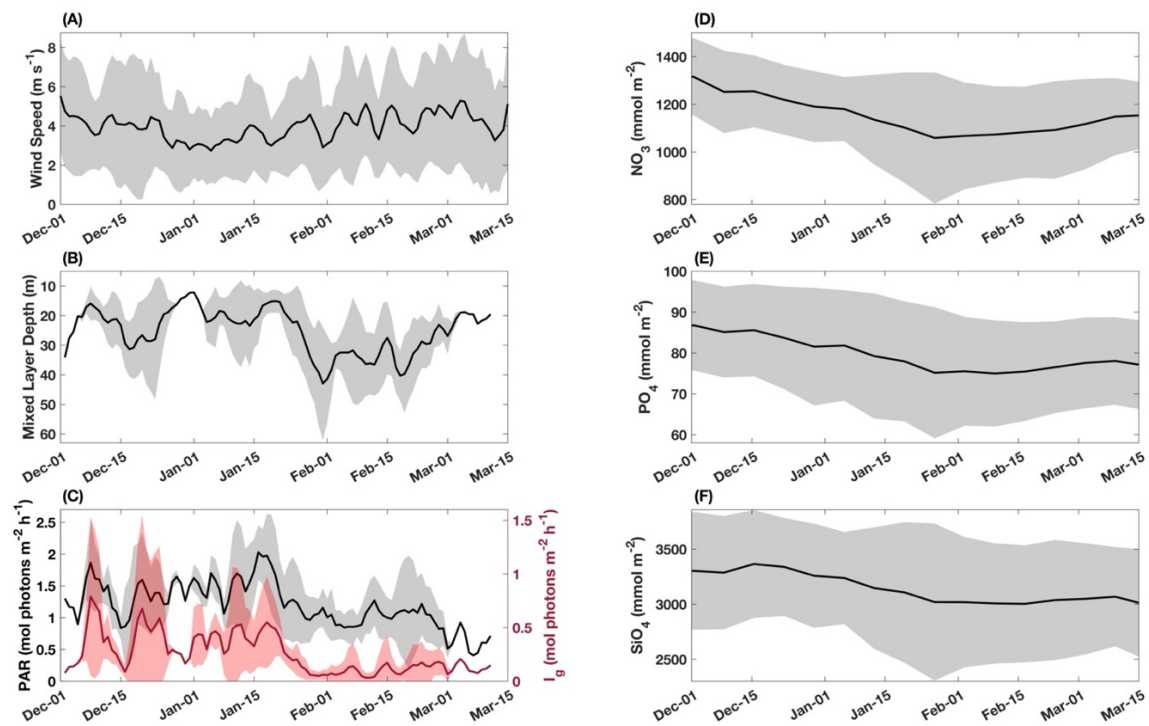


**Figure 4.** Seasonal (December 1 – March 15) climatologies of environmental variables from 2008-2020: (A) wind speed, (B) mixed layer depth, (C) PAR (black line) and  $I_g$  (red line), (D)  $\text{NO}_3$  concentration, (E)  $\text{PO}_4$  concentration, and (F)  $\text{SiO}_4$  concentration. Shaded bounds represent  $\pm 1$  standard deviation of annual daily values.

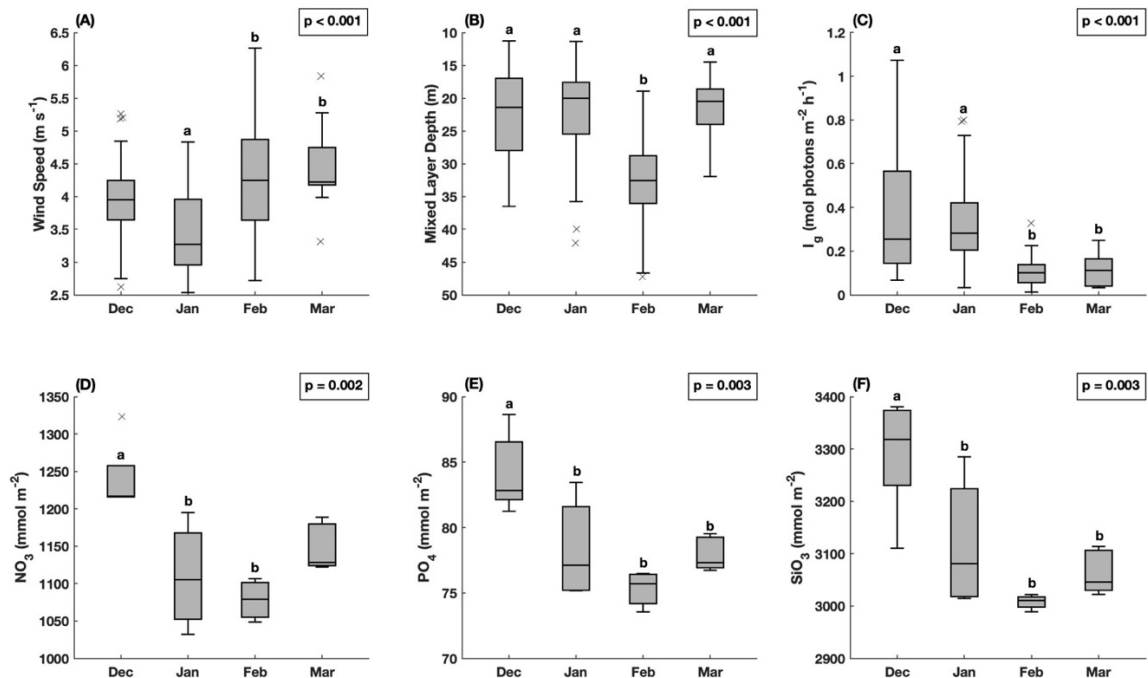


**Figure 5.** Monthly differences of daily climatology values for (A) wind speed, (B) mixed layer depth, (C)  $I_g$ , (D)  $\text{NO}_3$  concentration, (E)  $\text{PO}_4$  concentration, and (F)  $\text{SiO}_3$  concentration. One-way ANOVA  $p$ -values are indicated in the top right of each subplot, and lowercase letters indicate significant differences between months (different letters indicate significant differences) from Tukey-Kramer post-hoc results. (A-C) December  $n = 31$ , January  $n = 31$ , February  $n = 28$ , and March  $n = 11$ . (E-F) December  $n = 5$ , January  $n = 4$ , February  $n = 4$ , March  $n = 3$ . For each box plot, the horizontal line represents the median value, the top and bottom box limits represent the 25th and 75th percentiles, whiskers represent the full range of non-outlier observations, and multiplication ( $\times$ ) symbols represent outliers.

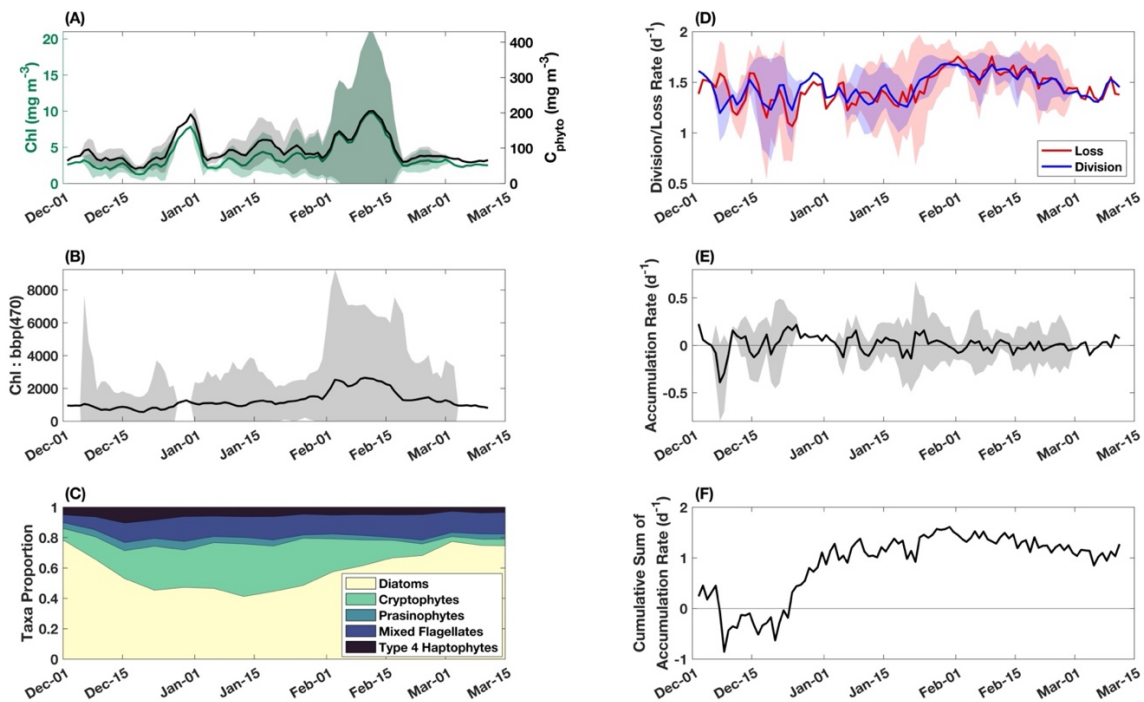


**Figure 6.** Seasonal (December 1 – March 15) climatologies of phytoplankton variables from 2008-2020: (A) MLD-averaged chlorophyll-*a* (green line) and  $C_{\text{phyto}}$  (black line) concentrations, (B) MLD-averaged chlorophyll-*a*:bbp(470) ratios, (C) proportions of phytoplankton taxa derived from HPLC, (D) division (blue line) and loss (red line) rates, (E) net accumulation rate, and (F) the cumulative sum of total accumulation rate. Shaded bounds represent  $\pm 1$  standard deviation of annual daily values.

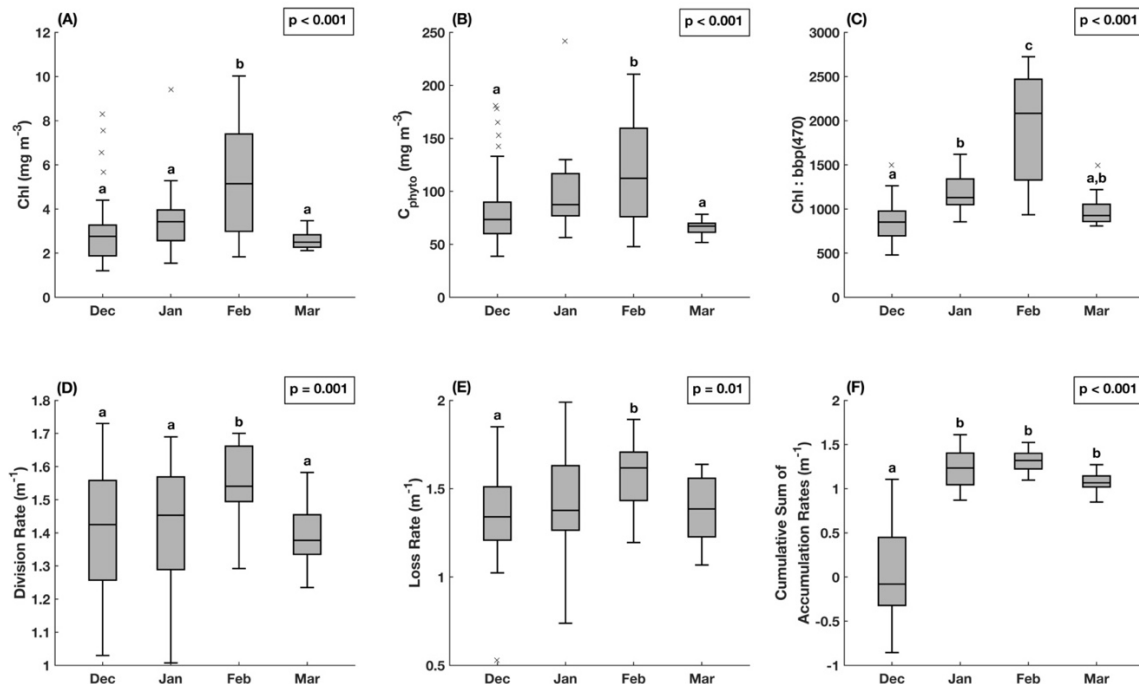
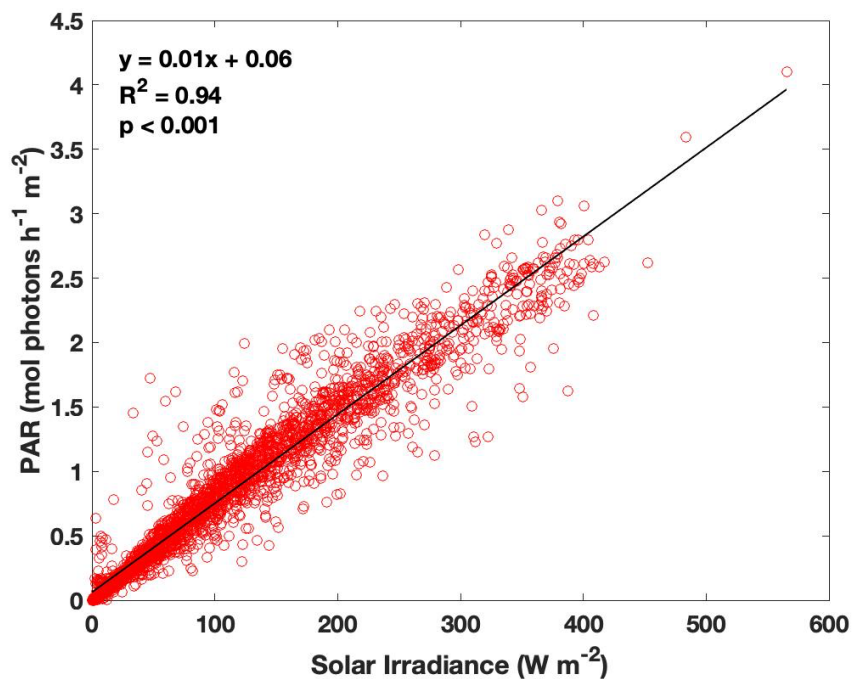
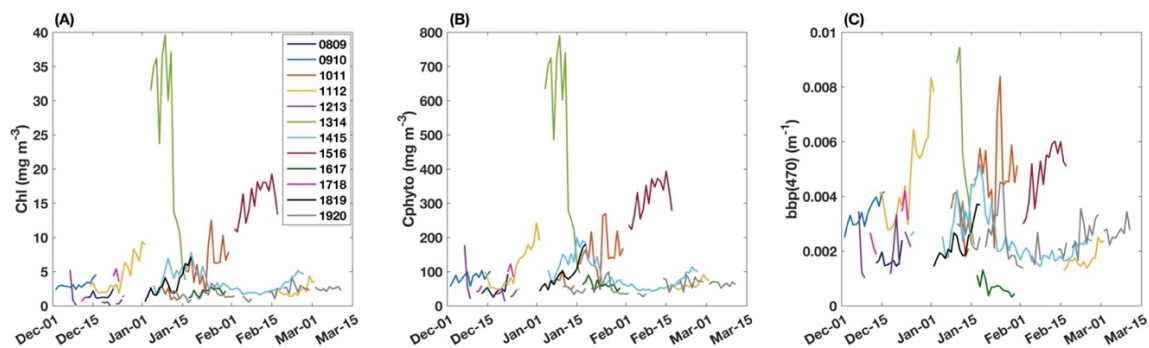


**Figure 7.** Monthly differences of daily climatology values for (A) chlorophyll-*a*, (B)  $C_{\text{phyto}}$ , (C) chlorophyll-*a* : bbp(470) ratio, (D) division rate, (E) loss rate, and (F) cumulative sum of net accumulation rates. One-way ANOVA  $p$ -values are indicated in the top right of each subplot, and lowercase letters indicate significant differences between months (different letters indicate significant differences) from Tukey-Kramer post-hoc results. December  $n = 31$ , January  $n = 31$ , February  $n = 28$ , and March  $n = 11$ . For each box plot, the horizontal line represents the median value, the top and bottom box limits represent the 25th and 75th percentiles, whiskers represent the full range of non-outlier observations, and multiplication ( $\times$ ) symbols represent outliers.

## 4.9 Supplementary Figures



**Supplementary Figure 1.** Relationship between daily-averaged solar irradiance and daily-averaged PAR from 1 October 2010 to 1 March 2019. Equation in top left corner was used to calculate missing PAR values in time series.



**Supplementary Figure 2.** Annual summer timeseries of (A) chlorophyll-*a*, (B)  $C_{\text{phyto}}$ , and (C)  $b_{\text{bp}}(470)$ .

## **5. Krill availability in adjacent Adélie and gentoo penguin foraging regions near Palmer Station, Antarctica**

### **5.1 Abstract**

The Palmer Deep canyon along the West Antarctic Peninsula is a biological hotspot with abundant phytoplankton and krill supporting Adélie and gentoo penguin rookeries at the canyon head. Nearshore studies have focused on physical mechanisms driving primary production and penguin foraging, but less is known about finer-scale krill distribution and density. We designed two acoustic survey grids paired with conductivity-temperature-depth (CTD) profiles within adjacent Adélie and gentoo penguin foraging regions near Palmer Station, Antarctica. The grids were sampled from January to March 2019 to assess variability in krill availability and associations with oceanographic properties. Krill density was similar in the two regions, but krill swarms were longer and larger in the gentoo foraging region, which was also less stratified and had lower chlorophyll concentrations. In the inshore zone near penguin colonies, depth-integrated krill density increased from summer to autumn (January to March) independent of chlorophyll concentration, suggesting a life history-driven adult krill migration rather than a resource-driven biomass increase. The daytime depth of krill biomass deepened through the summer and became decoupled from the chlorophyll maximum in March as diel vertical migration magnitude likely increased. Penguins near Palmer Station did not appear to be limited by krill availability during our study, and regional differences in krill depth match the foraging behaviors of the two penguin species. Understanding fine-scale

physical forcing and ecological interactions in coastal Antarctic hotspots is critical for predicting how environmental change will impact these ecosystems.

## 5.2 Introduction

The West Antarctic Peninsula is characterized by high summer primary productivity, large krill stocks, and abundant penguins, whales, and seals (Ross et al. 1996). Although the entire inner continental shelf is highly productive, penguin colonies are distributed heterogeneously (Fraser and Trivelpiece 1996), which has been related to the presence of deep submarine canyons that extend from the continental shelf break to the land margin and transport warm ( $>1^{\circ}\text{C}$ ), high-nutrient Upper Circumpolar Deep Water inshore (Couto et al. 2017). The interaction between the ocean currents and bathymetry in these canyons serves to concentrate and promote phytoplankton growth (Kavanaugh et al. 2015; Carvalho et al. 2019), and to aggregate Antarctic krill (*Euphausia superba*), supporting large higher trophic level populations (Santora and Reiss 2011). Few studies have investigated local-scale krill distributions within these canyon hotspots and their direct impact on predator foraging ecology.

The West Antarctic Peninsula is undergoing significant warming and melting, leading to a latitudinal climate gradient with warm, moist sub-polar conditions propagating south to replace cold, dry polar conditions (Stammerjohn et al. 2012; Cook et al. 2016). The Palmer Deep submarine canyon, located near the U.S. research base Palmer Station, is in the transition zone between polar and sub-polar climates, making it an ideal location to study ecosystem changes. Polar, ice-obligate Adélie penguins (*Pygoscelis adeliae*) have high breeding site fidelity and natal philopatry (i.e., they repeatedly return to their birthplace to breed), and colonies in the Palmer region have

existed for hundreds to thousands of years (Emslie 2001). With sea ice loss and increased snowfall, local Adélie penguin populations have declined ~90% since the 1970s (Fraser et al. 2020). Concurrently, sub-Antarctic, ice-intolerant gentoo penguins (*Pygoscelis papua*), established colonies near Palmer Station in 1994 and have been increasing ever since (Fraser et al. 2020). In the Palmer region, both species feed almost exclusively on krill (Fraser and Hofmann 2003; Pickett et al. 2018), and krill abundance in the region remained relatively stable from 1993 to 2013 (Steinberg et al. 2015). However, from 1976 to 2016 there was a krill abundance decline in the southwest Atlantic sector, and a southward range contraction that concentrated krill distribution along the West Antarctic Peninsula shelf (Atkinson et al. 2019). This is notable because further warming could cause additional range contractions and decreased krill biomass near Palmer Station (Klein et al. 2018), which in turn could increase penguin foraging efforts and decrease breeding success (Fraser and Hofmann 2003; Chapman et al. 2011).

Adélie and gentoo penguins are central place foragers, and nearly a decade of penguin satellite tag data near Palmer Station shows each species forages ~8 to 25 km from their respective colonies within two spatially segregated foraging habitats (Fig. 1; Cimino et al. 2016; Pickett et al. 2018). Adélie penguins breeding on Humble and Torgerson Islands forage mainly over the northern flank of the Palmer Deep canyon at shallow depths (mean  $17.1 \pm 8.8$  m; Pickett et al. 2018). This region is characterized by fresher, coastally-influenced waters with shallow mixed layer depths (MLDs), slower currents, longer residence times (1 to 4 days), and higher chlorophyll concentrations (Carvalho et al. 2016; Kohut et al. 2018). Gentoo penguins breeding on Biscoe Point forage over the southern flank of the canyon and into the Bismarck Strait, often at deeper

depths (mean  $41.5 \pm 23.6$  m; Pickett et al. 2018). This region is more offshore-influenced with intrusions of warm and nutrient-rich Upper Circumpolar Deep Water, deeper MLDs, faster currents, shorter residence times (0.2 to 2 days), and lower chlorophyll concentrations (Carvalho et al. 2016; Kohut et al. 2018).

Despite the importance of krill within this ecosystem, little is known about their role linking physical and primary production dynamics to penguin foraging. Previous studies show that austral summer krill distributions in the Palmer Deep canyon are influenced by physics (e.g., tidal cycles, MLD, winds) and phytoplankton concentration (Bernard and Steinberg 2013; Cimino et al. 2016; Bernard et al. 2017) and that foraging penguins respond to physical characteristics such as surface convergent features and tides (Oliver et al. 2013, 2019). Our study is the first to document seasonal krill dynamics specific to the two penguin foraging regions and describe differences in krill availability for the respective penguin populations. Using data collected over one austral summer, we assess (1) differences in krill availability (depth-integrated density, spatial and vertical distributions, and swarm structure) between the two penguin foraging regions, (2) associations between these patterns and regional oceanographic properties, and (3) implications for penguin foraging behavior. The surveys created for this study are the start of a new dataset introduced to the Palmer Antarctica Long-Term Ecological Research (LTER) project, designed to provide data on nearshore krill distributions at spatial and temporal scales that are relevant to penguin foraging ecology. Our results emphasize the importance of organismal life histories in understanding ecological interactions over seasonal scales, which is crucial for predicting how continued

environmental change will impact krill and penguin populations in ecologically important coastal areas.

## **5.3 Methods**

### *5.3.1 Survey design*

Survey design was based on nine years of penguin satellite tag data (2009-2018) indicating the key foraging regions for established Adélie and gentoo penguin colonies near Palmer Station. Methods for processing tag data and calculating the penguin foraging 2D kernel density estimations shown in Fig. 1 are outlined in Cimino et al. (2016) and Pickett et al. (2018). Two 20-nautical mile acoustic surveys were centered in each species' foraging region (Fig. 1). Each survey was paired with five conductivity-temperature-depth (CTD) profiling stations located midway across each northwest-southeast survey leg to collect ancillary physical oceanographic and phytoplankton data. Each survey was run weekly over one austral summer season (January to March 2019) during the daytime (approximately 9:00 to 15:00 local) pending weather. When possible, the two surveys were run on consecutive days, however weather sometimes increased the interval to three days. Two additional early-season surveys were conducted on November 28, 2018 in the Adélie region and on December 18, 2018 in the gentoo region. A total of 25 surveys were run over the season, 14 in the gentoo foraging region and 11 in the Adélie foraging region.

### 5.3.2 *Acoustic data collection*

Surveys were conducted aboard a 10-m-long rigid-hulled inflatable boat equipped with a hull-mounted, downward-facing Simrad EK80 single-frequency (120 kHz) transducer (Kongsberg Maritime, Kongsberg, Norway). During all surveys, 1 kW pulses at 256 ms duration were transmitted once per second. Geographic positions were simultaneously logged using the vessel's Global Positioning System. Acoustic surveying speed averaged 5 knots to ensure high-quality data while allowing for the longest feasible survey distance. The system was calibrated mid-season in the field using the standard sphere method (Foote 1990), whereby a 38.1 mm tungsten carbide calibration sphere with known acoustic properties was suspended below the transducer and moved within the acoustic beam.

### 5.3.3 *Krill net sampling*

To inform acoustic processing, *E. superba* were collected from the RV *Laurence M. Gould* in the Palmer Deep canyon using a 2 x 2 m square frame Metro net with 700  $\mu\text{m}$  mesh towed obliquely. Five net tows were conducted from January 6 to 8, 2019 (three tows down to 120 m and two krill-targeted tows to 20 m and 25 m, respectively), and six net tows were conducted from February 3 to 5, 2019 (two tows to 120 m, one krill-targeted tow to 100 m, two double tow-yos to 60 m, and one double tow-yo to 75 m). Length measurements were made for a random subsample of 100 *E. superba*, or all *E. superba* caught in each tow if there were < 100 krill (Standard Length 1 of Mauchline 1980). Krill length-frequencies were calculated in 1 mm bins separately for January, February, and both months combined. Gaussian mixture models were fit to the three

length-frequency distributions using the MATLAB function *fitgmdist*. Based on visual examination of the length-frequency histograms for the different time periods, three length modes were selected for the analysis. The model output gives the mean of each length mode and the mixing proportion for each mode (probability that an observation comes from that mode).

#### 5.3.4 Acoustic data processing

Raw acoustic data from the 120 kHz transducer were processed using Myriax Echoview version 10.0. Estimated background noise levels were subtracted from the echogram, and surface noise (top 4 m) and the ocean bottom were removed before analysis. The calibration from the transducer was applied to the echogram and adjusted for speed of sound and absorption coefficients derived from CTD profiles taken during each survey.

Volume backscattering strength (dB re 1 m<sup>-1</sup>) due to *E. superba* was isolated using a -70 dB threshold (Lawson et al. 2008). This threshold was estimated based on the maximum distance that krill can maintain visual contact with other krill and reflects a packing density of 1.7 ind. m<sup>-3</sup>. In addition to *E. superba*, the krill species *Thysanoessa macrura* was present in the study area during the survey period. In most cases, the -70 dB threshold and swarm detection parameters (see below) likely excluded *T. macrura*, which is distributed more evenly in space than *E. superba* and forms diffuse aggregations that are acoustically distinct from those of *E. superba* (Daly and Macaulay 1988; Lawson et al. 2008). Therefore, the contribution of *T. macrura* to estimated krill biomass in this study is likely minor. The tunicate *Salpa thompsoni* has a similar target strength (TS) to

krill (-85 to -65 dB at 120 kHz; Wiebe et al. 2010), however, during the study period, no salps were encountered in the net tows or seen floating on the surface, which is common in years when salps are abundant.

Because ~98% of krill biomass is contained in patches or swarms (Fielding et al. 2014), swarms were isolated and used for our analysis. Krill swarms were detected using the 'School Detection module' in Echoview. The software detected swarms with a minimum length of 4.5 m and a height of 2 m, and linked swarms within 15 m horizontally and 5 m vertically of each other. These parameters were determined based on the resolution of our acoustic data, guided by methods in Tarling et al. (2018). Detected swarms that were too small to be corrected for beam geometry were removed from the analysis (Diner 2001).

Acoustic noise limited detection of swarms deeper than 250 m, however, this limitation should have minimal impact on our biomass estimates as most studies show that summertime krill swarms typically reside in the top 150 m of the water column (e.g., Miller and Hampton 1989). High phytoplankton productivity in summer and early autumn likely resulted in little to no krill benthic feeding, which is usually a result of reduced feeding success in surface waters (Schmidt et al. 2011). Additionally, this analysis is focused on krill availability to penguins in the Palmer region, which typically forage in the top 150 m of the water column (Pickett et al. 2018).

During our 25 survey days, a total of 3521 krill swarms were detected. Individual swarm features were calculated including mean length (m), mean height (m), and area (m<sup>2</sup>). Volume backscattering strength was integrated within each krill swarm, resulting in an area backscattering coefficient ( $s_a$ ; m<sup>2</sup> m<sup>-2</sup>) value. Depth-integrated krill  $s_a$  values were

similarly calculated by integrating volume backscattering strength from the surface to either 250 m or the seafloor, whichever was shallower, in 10-m horizontal increments along each survey track. To characterize the depth distribution of krill, volume backscattering strength was also integrated within 10-m horizontal by 1-m vertical bins for each survey, providing an  $s_a$  value for each grid cell.

The  $s_a$  values from individual krill swarms, depth-integrated survey segments, and 1-m vertical bins were all converted to density (g wet weight [WW]  $m^{-2}$ ) following methods in Reiss et al. (2008). Krill TS at 120 kHz was calculated using the simplified stochastic distorted-wave Born approximation model (Conti and Demer 2006) based on krill length-frequencies from either January, February, or both months combined. To remove extreme outliers, 99% of krill length-frequencies were used (Tarling et al. 2009). Surveys conducted before January 17 used January length-frequencies, surveys between January 17 and 25 used both months' length-frequencies, and surveys after January 25 used February length-frequencies.

Krill density (g WW  $m^{-2}$ ) in individual krill swarms, depth-integrated survey segments, and 1-m vertical bins was calculated by multiplying  $s_a$  values by an area scattering conversion factor (CF) for the respective length-frequency distribution:

$$CF = \frac{\sum_{b=1}^B f_b \times w(L_b)}{\sum_{b=1}^B f_b \times \sigma(L_b)},$$

where B is the total number of length-frequency bins, b,  $f_b$  is the frequency for each length-frequency bin, w (g per krill) is the wet weight (WW) of an individual krill as a function of body length (L; mm), calculated using the model developed from

Commission for the Conservation of Antarctic Marine Living Resources (CCAMLR)  
2000 survey data in the Scotia Sea (Hewitt et al. 2004):

$$w = 2.236 \times 10^{-6} \times L^{3.314},$$

and  $\sigma$  (m<sup>2</sup> per krill) is the backscattering cross-section of an individual krill as a function of body length:

$$\sigma = 10^{\text{TS}(L)/10}.$$

Total biomass (g WW) in individual krill swarms, depth-integrated survey segments, and 1-m vertical bins was calculated by multiplying the density of a krill swarm or bin by its area in m<sup>2</sup>.

### 5.3.5 *Environmental data*

At each profiling station, CTD (SeaBird Electronics Seacat SBE 19plus sensor) and chlorophyll *a* fluorescence measurements (Wet Labs ECO fluorometer sensor) were made down to 120 m depth or within 10 m of the bottom at shallower stations. These downcast data were averaged in 1-m depth bins. Chlorophyll *a* fluorescence was calibrated against discrete water samples collected at 50 m and 65 m twice per week from January to March at Palmer LTER Station E (located just east of Outcast Island, Fig. 1). Water samples were filtered onto Whatman GF/F filters, extracted in 90% acetone, and analyzed using a Turner fluorometer. Calibrated chlorophyll *a* profiles were then

corrected for non-photochemical quenching using methods from Xing et al. (2012). For each profile, 50 m-averaged temperature, 50 m-averaged salinity, 50 m-averaged particulate beam attenuation coefficient (beam  $c$ ), 50 m-integrated chlorophyll  $a$ , and the depth of the chlorophyll maximum were calculated.

Since photosynthetically active radiation (PAR) measurements were not collected during surveys, 50 m-averaged beam  $c$  measurements were compared to the depth of 1% PAR measured biweekly at Station E from January to March. A negative linear correlation was found between the two (Pearson's  $r = -0.78$ ,  $p \leq 0.001$ ,  $n = 23$ ), and therefore, 50 m-averaged beam  $c$  was used as a proxy for light attenuation in the surface water column.

The seasonal MLD was calculated from vertical profiles of temperature and salinity according to Carvalho et al. (2017) and is based on the depth of the maximum buoyancy frequency ( $\max(N^2)$ ). A quality index value (QI; Lorbacher et al. 2006) was calculated for each vertical profile and was used to filter out profiles without significant stratification ( $QI < 0.5$ ). This approach was validated using a ship-based study along the West Antarctic Peninsula (Schofield et al. 2018).

Wind speed ( $\text{m s}^{-1}$ ) measurements were obtained from an automated weather station located just behind Palmer Station. 12-hour averages of wind speeds were calculated for the duration of the study period using 2-minute data.

### 5.3.6 *Statistical analysis*

All statistical analyses were conducted in MathWorks MATLAB version R2019b. Data were grouped prior to statistical analysis to address specific spatial and temporal

questions. For spatial analysis, a single value for each krill variable (median swarm length, median swarm height, median swarm area, median swarm biomass, median swarm density, median krill depth, mean depth-integrated krill density, and number of krill swarms per km) was calculated for each of the five survey legs in the two penguin foraging regions (see Fig. 1) for all survey days. This approach allowed pairing of the CTD and acoustic data and created equal sample sizes for all variables. For temporal analysis, a single mean or median value for each krill variable (see above) and environmental variable (mean 50 m-averaged temperature, mean 50 m-averaged salinity, mean 50 m-integrated chlorophyll *a*, mean 50 m-averaged beam *c*, mean MLD, and mean  $\max(N^2)$ ) was calculated for each survey day in the two penguin foraging regions. The same approach was used for the two inshore survey legs combined and the two offshore survey legs combined within each foraging region. For temporal and spatial analyses, the median krill depth was calculated using 1-m vertically binned krill densities averaged across each leg and survey. Only the ten weeks when both surveys were conducted were included in statistical analyses to allow for a paired sample design.

Spatial differences between and within penguin foraging regions were analyzed with generalized linear mixed-effects models (GLMMs) fit by maximum likelihood (MATLAB function *fitglme*) using the single mean or median values for each survey leg. We chose GLMMs because many of the model response variables had non-normal data distributions that generalized models can accommodate, and because mixed models can account for the temporal dependence in our data caused by our repeated, paired sample design. Each environmental and krill variable was the response variable in three different models. The first model included penguin foraging region (Adélie or gentoo) as a

categorical, fixed effect to test for spatial differences between foraging regions. The other two models included survey leg (1-5) as a continuous, fixed effect to test for inshore to offshore differences across the Adélie and gentoo regions, respectively. Sampling week was included as a random effect in all models to account for the repeated, paired sample design. For all GLMMs, appropriate model error distributions and link functions were selected by visually inspecting histograms of response variables.

Temporal trends for each penguin foraging region were analyzed with generalized linear models (GLMs; MATLAB function *fitglm*) using the single mean or median values for each survey day. Each environmental and krill variable was set as the response variable in six different models. A pair of models tested for temporal change in the full Adélie and gentoo foraging regions, respectively. A second pair of models tested for temporal change in the two inshore survey legs of the Adélie and gentoo foraging regions, respectively. A third pair of models tested for temporal change in the two offshore survey legs of the Adélie and gentoo foraging regions, respectively. All models included sampling date as a continuous, fixed variable. For all GLMs, appropriate model error distributions and link functions were selected by visually inspecting histograms of response variables.

To determine relationships between environmental and krill variables, non-parametric Kendall rank correlation tests (MATLAB function *corr*) were used due to the non-normal data distributions of most variables. Variables were paired by survey leg for correlations so that the sample size of krill variables matched the sample size of environmental variables derived from CTD profiles.

## 5.4 Results

### 5.4.1 *Krill population characteristics*

During our study, three modes of krill lengths were detected in the Palmer Deep canyon region. Juvenile krill (modes 1 and 2) accounted for 41% of total measured animals (Fig. 2A). From January to February, mode 1 shifted from 13.2 to 15.2 mm, while mode 2, centered at 21.1 mm in January, mostly disappeared from the region by early February (Fig. 2B, C). Adult krill (mode 3) accounted for 59% of total measured animals and shifted from 35.3 to 44.0 mm from January to February (Fig. 2A-C).

### 5.4.2 *Spatial variability*

Significant differences between the adjacent penguin foraging regions were found from January to March. The Adélie region was significantly fresher with higher  $\max(N^2)$  magnitudes, higher integrated chlorophyll *a* concentrations, and shallower MLDs than the gentoo foraging region (GLMM  $p \leq 0.03$ ; Fig. 3A-D and Table 1). The Adélie region was also marginally warmer with higher beam *c* values (i.e., increased light attenuation) than the gentoo foraging region (GLMM  $p = 0.13$  and  $p = 0.08$ , respectively; Fig. 3E, F and Table 1). Temperatures  $< 0.5$  °C, salinities  $< 33.6$ , and  $\max(N^2)$  values  $> 1.0 \times 10^{-3}$  were all present in the Adélie region but absent in the gentoo region, indicating a greater influence of surface meltwater in the Adélie region (Fig. 3A, B, E).

Krill swarms in the gentoo foraging region were longer, thicker, larger, denser, and contained higher biomass than swarms in the Adélie region (GLMM  $p \leq 0.002$ ; Fig. 4A-E and Table 1). Additionally, fewer krill swarms were encountered when the chlorophyll *a* concentration was low (Kendall  $p = 0.01$ ,  $\tau = 0.18$ ,  $n = 94$ ), and these

swarms were longer and larger (Kendall  $p \leq 0.001$  and  $0.002$ ,  $\tau = -0.28$  and  $-0.21$ ,  $n = 94$  and  $94$ , respectively). Despite differences in krill swarm structure, there were no significant differences in the median krill depth, depth-integrated krill density, or the number of krill swarms per km between foraging regions (GLMM  $p \geq 0.27$ ; Fig. 4F-H and Table 1). Although the difference in median krill depth was not statistically significant, the median value in the Adélie region was 28 m shallower than in the gentoo region (55 m versus 83 m; Fig. 4F), which is similar to the 24.4 m difference in mean penguin foraging dive depths between the two regions (17.1 m for Adélie penguins and 41.5 m for gentoo penguins; Pickett et al. 2018).

There was less variability within each foraging region than between them. There were no significant differences across survey legs for environmental variables in either region (GLMM  $p \geq 0.15$ ; Supplementary Table 1), or for krill variables in the gentoo foraging region (GLMM  $p \geq 0.14$ ; Table 2). However, in the Adélie region, depth-integrated krill density was highest inshore where there were more krill swarms per km (GLMM  $p \leq 0.003$ ; Fig. 5A, B and Table 2). This heightened inshore density existed despite individual swarms being less dense and containing less biomass on the inshore survey legs (GLMM  $p \leq 0.004$ ; Fig. 5C, D and Table 2). Krill distribution was also deepest inshore in the Adélie region (GLMM  $p = 0.01$ ; Fig. 5E and Table 2).

#### 5.4.3 *Spatiotemporal variability in krill density*

The temporal trends of environmental and krill variables inshore versus offshore were mostly similar. For example, median krill depth deepens over time both inshore and offshore in both regions (GLM  $p \leq 0.005$ ; Supplementary Tables 2 and 3). However, the

temporal trends in depth-integrated krill density showed different patterns inshore versus offshore. In the first half of our paired sampling period (January 13 to February 16), depth-integrated krill density was highest in the gentoo region, and biomass was concentrated in the offshore survey legs near the Wauwerman Islands (Fig. 6A). In the second half of our study period (February 17 to March 23), krill density was highest at the inshore survey legs in both regions (Fig. 6B). Although krill density was variable week to week, increasing trends in krill density for the inshore survey legs and decreasing trends for the offshore survey legs in both foraging regions suggest an inshore re-distribution of krill biomass from January to March (Fig. 6C, D).

#### 5.4.4 Seasonal patterns

Despite significant environmental differences between the two foraging regions, seasonal patterns were similar (Fig. 7A, B, D, E). Surface freshwater pulses throughout the season stabilized the water column (increased  $\max(N^2)$ ; Kendall  $p = 0.01$ ,  $\tau = -0.24$ ,  $n = 52$ ) and spurred phytoplankton blooms (Kendall  $p = 0.008$ ,  $\tau = -0.19$ ,  $n = 94$ ). In January, relatively calm winds (mean  $2.8 \text{ m s}^{-1}$ ) and the presence of surface meltwater (0 to 10 m) resulted in shallow MLDs (mean Adélie = 7.8 m; mean gentoo = 12.3 m) and high  $\max(N^2)$  values (mean Adélie = 0.001; mean gentoo =  $6.9 \times 10^{-4}$ ). On January 24, a peak in wind speed ( $12.8 \text{ m s}^{-1}$ ) deepened respective MLDs to 48.3 m and 60.0 m in the Adélie and gentoo regions, concurrent with increases in integrated chlorophyll *a* from respective averages of  $69.1 \text{ mg m}^{-2}$  and  $61.7 \text{ mg m}^{-2}$  before the wind event to peaks of  $176.8 \text{ mg m}^{-2}$  and  $159.5 \text{ mg m}^{-2}$  just after the wind event. MLDs deepened to 70.6 m and 67.0 m in the Adélie and gentoo regions, respectively, in late February due to higher wind

speeds in the first half of February (mean  $4.8 \text{ m s}^{-1}$ ). In response, phytoplankton biomass decreased to an average of  $70.4 \text{ mg m}^{-2}$  and  $41.7 \text{ mg m}^{-2}$ . Calmer winds in late February and early March (mean  $2.5 \text{ m s}^{-1}$ ) and a small surface meltwater layer reduced MLDs in mid-March (Adélie =  $10.5 \text{ m}$ ; gentoo =  $28.6 \text{ m}$ ), leading to a secondary small bloom (Adélie =  $111.1 \text{ mg m}^{-2}$ ; gentoo =  $111.9 \text{ mg m}^{-2}$ ).

Krill biomass deepened significantly in both regions (GLM  $p \leq 0.005$ ; Fig. 7C, F and Supplementary Table 4), especially following the primary phytoplankton bloom. The median krill depth increased from an average of  $21.4 \text{ m}$  and  $47.6 \text{ m}$  in January to an average of  $165.7 \text{ m}$  and  $149.5 \text{ m}$  in March for the Adélie and gentoo regions, respectively. Deeper median krill depths were correlated with lower integrated chlorophyll *a* concentrations (Kendall  $p \leq 0.001$ ,  $\tau = -0.26$ ,  $n = 94$ ) and lower beam *c* values (Kendall  $p \leq 0.001$ ,  $\tau = -0.37$ ,  $n = 94$ ). In both regions, the median krill depth remained closer to the depth of the chlorophyll maximum through the primary bloom (Adélie =  $8.4 \text{ m}$  and gentoo =  $28.5 \text{ m}$  average depth differences) than post-bloom when the difference between the two became larger (Adélie =  $84.4 \text{ m}$  and gentoo =  $73.5 \text{ m}$  differences in February; Adélie =  $152.6 \text{ m}$  and gentoo =  $137.7 \text{ m}$  differences in March), indicating a decoupling of krill biomass from the chlorophyll maximum (Fig. 7B, C, E, F).

The date of peak penguin chick fledging (February 13 for Adélie penguins and March 1 for gentoo penguins) coincides with the deepening of krill biomass in both regions (Fig. 7C, F). Percent krill biomass available within each species' observed foraging depths ( $0\text{-}82 \text{ m}$  for Adélie penguins and  $0\text{-}144 \text{ m}$  for gentoo penguins) decreased

from an average of 75.7% to 16.3% in the Adélie region and from 96.3% to 44.8% in the gentoo region from before to after peak fledging.

## 5.5 Discussion

The Adélie and gentoo penguin foraging regions are adjacent to each other in the Palmer area, with the colonies located roughly 10 km apart, yet the foraging regions have significantly different oceanographic properties and krill availability. These small-scale differences are significant to central place foraging penguins that have limited foraging ranges and are responsible for the survival of their chicks at the nest. These fine-scale and dynamic features are important in understanding differences in the foraging ecology between the local penguin populations as this polar ecosystem continues to change.

### 5.5.1 *Krill population characteristics*

Juvenile krill accounted for 41% of total measured animals, indicating a moderately successful recruitment year (Fig. 2; Ross et al. 2014). The prevalence of small (10-20 mm) krill during our study is unusual. Larval *E. superba* spawned the same summer would most likely be in the calyptopis stages (< 5 mm) during January/February, with relatively few having reached furcilia stages (roughly 5-15 mm; Gibbons et al. 1999). Thus, the 10-20 mm mode is either very large age-class 0 krill or small age-class 1 krill. The latter is more likely, and two separate length modes for age-class 1 krill are sometimes reported during summer along the West Antarctic Peninsula (Ross et al. 2014).

### 5.5.2 *Spatial variability*

The Adélie region was fresher, had greater integrated chlorophyll *a* and max( $N^2$ ) values, a shallower MLD, and a greater influence of coastal meltwater (Fig. 3 and Table 1). The Adélie region receives greater inputs of coastal meltwater and has slower currents, resulting in a stable water column conducive to phytoplankton growth (Carvalho et al. 2016; Kohut et al. 2018). Conversely, the gentoo region receives offshore intrusions of Upper Circumpolar Deep Water and has faster currents, which flush coastal meltwater and phytoplankton out of the region more quickly (Carvalho et al. 2016; Kohut et al. 2018).

There were no significant differences between depth-integrated krill density, the median krill depth, or the number of krill swarms per kilometer encountered in the two foraging regions, however, there were significant differences in krill swarming behavior (Fig. 4 and Table 1). These patterns are significant for foraging penguins that depend on food sources proximate to their colonies. Krill swarming behavior responds to the environmental conditions that krill are experiencing, mainly to aid in finding food (Folt and Burns 1999). In the gentoo region, lower integrated chlorophyll *a* concentrations correlated with longer and larger swarms. Previous studies in the Palmer region found krill swarms associated with low chlorophyll environments and attributed this pattern to grazing (Bernard et al. 2017) and to avoidance of high phytoplankton biomass areas that could be associated with higher predation risks (Cimino et al. 2016). Alternatively, assuming some level of organization between individuals within a swarm, a larger swarm area may increase the probability of encountering patches of food and increase foraging efficiency, and could be a strategy to locate food in low-chlorophyll environments

(Hamner and Hamner 2000; Tarling et al. 2009). Greater krill densities are also found in shallower water depths and along steep bathymetric slopes (Santora and Reiss 2011; Silk et al. 2016), thus, the shallow and complex bathymetry (pinnacles and seamounts) around the Wauwerman Islands may contribute to the higher-density swarms in the gentoo region.

Although not statistically significant, the median krill depth was 28 m deeper in the gentoo region than the Adélie region, and was negatively correlated with chlorophyll *a* and beam *c*. Higher integrated chlorophyll *a* concentrations in the Adélie region increase light attenuation (reflected in higher beam *c* values) and may offer more protection from visual predators than in the gentoo region, allowing krill swarms to remain shallower. Additionally, krill may remain deeper in the gentoo region to avoid getting flushed from the region by strong surface currents (Kohut et al. 2018). Differences in krill depth distributions appear to drive differences in Adélie and gentoo foraging depths, with gentoo penguins at Biscoe Point foraging on average at deeper depths than Adélie penguins at Humble and Torgerson Islands (41.5 m and 17.1 m respectively; Pickett et al. 2018), roughly matching the 28 m difference in median krill depth between the regions.

No significant environmental or krill differences were found across the five survey legs in the gentoo region, but in the Adélie region, there was higher depth-integrated density, more krill swarms per km, and deeper krill biomass inshore compared to offshore (Fig. 5). Additionally, krill swarms inshore were less dense and contained less biomass despite the higher depth-integrated density inshore. Higher depth-integrated krill density inshore could be related to the shoaling bottom depths near Outcast Island, and

deeper inshore krill biomass could be a response to increased predation closer to the Adélie penguin colonies (Klevjer et al. 2010). However, numerous low-biomass and low-density swarms inshore contradicts the expectation of larger and denser swarms in the presence of visual predators (Fielding et al. 2012), such as the Adélie penguins making foraging trips from Humble and Torgerson Islands.

### 5.5.3 *Spatiotemporal variability in krill density*

Krill biomass dynamics operate on large spatial and temporal scales linked to their life history, with interannual variability driven by recruitment success (Reiss et al. 2008; Saba et al. 2014) and seasonal variability driven by horizontal migration (Siegel 1988; Nicol 2006). In summer, the adult krill population is concentrated near the shelf break, and juvenile krill are most abundant in coastal waters (Siegel et al. 2013; Conroy et al. 2020). In early autumn, adult krill begin moving inshore to troughs or canyons where they can utilize deep food resources during the winter (Cleary et al. 2016; Reiss et al. 2017), while juvenile and larval krill may remain shallow to access under-ice algae (Bernard et al. 2018; Walsh et al. 2020). Over our study period, krill density increased inshore in the Adélie and gentoo regions (Fig. 6), independent of changes in environmental parameters. Although there is variability in weekly krill distribution due to behavioral responses to ocean physics, food availability, and predation, the increased density inshore (especially in the Adélie region) could be linked to the inshore migration of adult krill in late summer. No net tows were available later than early February to confirm this hypothesis, but presumably we would have found a higher proportion of adult krill in those tows. The inshore increase in the gentoo region is more variable,

which might reflect greater surface current speeds that may flush krill out of the region via the Bismarck Strait (Kohut et al. 2018), or the tendency of krill to aggregate near the seamounts and walls that are present along the offshore survey legs near the Wauwerman Islands.

The prevalence of juvenile krill during our study likely benefitted both penguin species. Juvenile krill remain close to shore in summer (Siegel et al. 2013; Conroy et al. 2020), causing mean depth-integrated krill density in our study to stay high throughout the summer (minimums of 111.9 g WW m<sup>-2</sup> and 72.7 g WW m<sup>-2</sup> for the Adélie and gentoo regions, respectively), which could lead to shorter foraging trips, chicks fed at more frequent intervals, increased chick fledging masses, and increased survival rates (Fraser and Hofmann 2003; Cimino et al. 2014). During failed recruitment years, the lack of juvenile krill inshore during summer may increase the importance of the cross-shelf adult krill migration for coastal penguin colonies and may lead to greater seasonal variability in krill biomass.

Using 12 years of Palmer LTER data (1995-2006), Sailley et al. (2013) found that penguin colonies at Palmer Station did not appear to be limited by local krill biomass. This agrees with the results of our study. In austral summer 2018-2019, there were 1586 Adélie penguin breeding pairs (3172 potentially foraging adults) and 3655 gentoo penguin breeding pairs (7310 potentially foraging adults; W. R. Fraser unpubl.). Along the West Antarctic Peninsula, past studies show average krill consumption values per foraging trip of 348.6 g (n = 48; Volkman et al. 1980) and 510.7 g (n = 12; Trivelpiece et al. 1987) for Adélie penguins and 365.0 g (n = 46; Volkman et al. 1980), 433.4 g (n = 14; Trivelpiece et al. 1987), 671.1 g (Admiralty Bay, n = 120; Miller et al. 2010), and 422.0 g

(Cape Shirreff,  $n = 130$ ; Miller et al. 2010) for gentoo penguins. Using the maximum average consumption estimates for each species and assuming one foraging trip a day per penguin, 3172 Adélie penguins and 7310 gentoo penguins would consume 1.6 and 4.9 tons of krill per day, respectively. Total krill biomass encountered on a given survey day (only considering our 20 nautical mile survey line) ranged from 27.2 to 1075.4 tons WW in the Adélie region and from 18.9 to 1266.6 tons WW in the gentoo region, indicating no shortage of krill for penguins within each foraging region, and plenty of prey left over for other krill predators foraging in the region such as whales, seals, fishes, and flying seabirds. In addition, Palmer region penguins forage relatively close to colonies (~8-25 km) compared to penguins in other locations where foraging trips can reach 100 km (Williams 1995), and both species are capable of much deeper dives than are seen in the Palmer region (Bost et al. 1994; Watanuki et al. 1997), further supporting that penguins do not appear to be limited by krill in this area.

#### 5.5.4 *Seasonal patterns*

The seasonal dynamics of phytoplankton in both foraging regions match those observed over six austral summer seasons (2010 to 2015), with phytoplankton blooms coupled to surface meltwater dynamics (Fig. 7A, B, D, E; Carvalho et al. 2016). In late austral spring, day length is increasing, and solar warming and sea ice melt stratify the upper water column allowing phytoplankton to remain in surface waters with ample access to sunlight (Vernet et al. 2008). These conditions spur a large phytoplankton bloom in January (Carvalho et al. 2016). Following the primary bloom, decreases in meltwater inputs combined with increased wind mixing cause MLDs to deepen, mixing

phytoplankton deeper in the water column out of the range of sunlight needed for growth (Mitchell and Holm-Hansen 1991) and leading to a decline in chlorophyll concentrations. A secondary bloom in late February/early March is associated with increased freshwater input and increased water column stability, likely initiated by continued seasonal warming and glacial meltwater runoff into coastal waters (Moline and Prézelin 1996; Carvalho et al. 2016).

Similar to other Antarctic studies (Taki et al. 2005; Fielding et al. 2012), daytime krill biomass shifted deeper in the water column from January to March (Fig. 7C, F). This pattern suggests an increase in the magnitude of diel vertical migration (DVM), a behavior cued by light that balances feeding with the avoidance of visual predators (Hays 2003). During the midsummer period of near continual daylight, *E. superba* remains in surface waters to feed throughout the diel cycle and exhibits shallow or inconsistent DVM (Tarling et al. 2018). The first half of our study period is characterized by long day length (21:17 to 16:05 hours), with high integrated chlorophyll *a* concentrations that increase light attenuation in surface waters (as evidenced by larger beam *c* values). Although day length is long, darker daytime surface waters may offer some protection from visual predators, allowing krill to remain shallow near the depth of the chlorophyll maximum. The proximity of the median krill depth to the chlorophyll maximum in both regions through the primary bloom in late January/early February suggests krill are feeding during the daytime.

Krill DVM is typically more pronounced during spring and autumn when photoperiod is shorter (Ross et al. 1996; Taki et al. 2005). During the second half of our study, day length was shorter (15:58 to 11:03 hours) and integrated chlorophyll *a*

concentrations decreased, which reduced light attenuation in surface waters (as evidenced by decreased beam  $c$  values). Brighter daytime surface waters may make krill more susceptible to visual predators, and reduced day length increases the opportunity for protected nighttime feeding. The increased distance between median krill depth and the depth of the chlorophyll maximum in both regions after the primary bloom suggests the prioritization of daytime predator avoidance over feeding.

Adélie penguin breeding phenology is typically 2 to 3 weeks earlier than that of gentoo penguins, with peak fledging occurring in mid-February for Adélie penguins and in early March for gentoo penguins (Pickett et al. 2018). Obtaining high krill yields during periods of peak chick growth is critical for chick survival, and interestingly, the date of peak fledging for each species coincided with the deepening of krill biomass in their respective foraging regions (Fig. 7C, F). Adélie penguins are migratory and usually depart the Palmer area after fledging, while gentoo penguins are non-migratory and require food in this region beyond March. There are no foraging data post-fledging, but gentoo penguins likely increase foraging dive depths in March to match the depth of the prey field.

### 5.5.5 *Conclusions*

Ongoing environmental change along the West Antarctic Peninsula is expected to impact krill recruitment and penguin foraging dynamics in the Palmer Station area. Water column stratification and phytoplankton concentration do not appear to impact the krill biomass present on a given day in the Palmer area, however, bottom-up processes drive krill recruitment success or failure over interannual scales (Saba et al. 2014). Long-term

warming, sea ice declines, and increasing wind speeds cause MLDs to deepen and phytoplankton concentrations to decline and shift to smaller cells (Montes-Hugo et al. 2009), which could lead to sustained poor krill recruitment over longer time scales. Decreased krill recruitment could lead to greater seasonal fluctuations in krill abundance near penguin colonies. Warmer waters and less sea ice habitat could also detrimentally impact krill growth and lipid accumulation (Ruck et al. 2014; Klein et al. 2018). Less consistent krill availability and reduced prey quality may result in increased penguin foraging efforts (e.g., longer foraging trip durations, deeper dives). The transition from Adélie to gentoo penguins in the region might shift the demand for krill later in the summer based on differences in breeding phenology and increase the need for seasonally sustained krill to accommodate a non-migratory local population. However, gentoo penguins have a more diverse diet than Adélie penguins, and alternate prey options could potentially support their needs when local krill availability is low (Pickett et al. 2018).

This study highlights large temporal and spatial variability in krill distributions over the scales relevant to foraging penguins in the Palmer Station vicinity (e.g., differences in krill swarming behavior within regions only 10 km apart). This emphasizes the importance of high-resolution data sets in studying predator foraging ecology. Continued full-ecosystem research incorporating organismal life-history strategies is imperative for understanding the underlying factors that structure coastal biological hotspots and how further environmental change will impact them.

## 5.6 Acknowledgments

This work was supported by the National Science Foundation Antarctic Organisms and Ecosystems Program (PLR-1440435) as part of the Palmer Antarctica Long-Term Ecological Research (Palmer LTER) program. Additionally, SN acknowledges support from the Rutgers Institute of Earth, Ocean, and Atmospheric Sciences graduate fellowship, WF acknowledges support from the Detroit Zoological Society and NSF Office of Polar Programs (ANT-1745018), and MC acknowledges support from the NSF Office of Polar Programs (ANT-1744859). This is Contribution No. 4002 from the Virginia Institute of Marine Science, William & Mary. Thank you to Anthony Cossio and Chris Taylor for sharing acoustic processing code and advice. This work would not be possible without the Palmer LTER field teams who aided in data collection and Palmer Station personnel for logistics support. Comments from two anonymous reviewers helped improve and clarify this manuscript.

## 5.7 Tables

**Table 1.** Results from GLMMs assessing the differences in variables between Adélie and gentoo penguin foraging regions. Models for 50m-averaged temperature and 50m-averaged salinity used a normal distribution and identity link function while all other models used a gamma distribution and log link function. Significant results are indicated in bold. Weather occasionally prevented profiling at some CTD stations, and some MLD profiles failed to meet the QI threshold, resulting in  $n < 50$  for those CTD-derived variables.

Variable	Adélie $n$	Gentoo $n$	Coeff	SE	$t$	$p$
50m-avg temperature (°C)	45	49	-0.08	0.05	-1.51	0.13
50m-avg salinity (PSU)	45	49	0.10	0.02	6.78	< <b>0.001</b>
50m-int chlorophyll $a$ (mg m <sup>-2</sup> )	45	49	-0.18	0.08	-2.19	<b>0.03</b>
50m-avg beam $c$ (m <sup>-1</sup> )	45	49	-0.08	0.05	-1.78	0.08
MLD (m)	28	24	0.34	0.15	2.29	<b>0.03</b>
Max(N <sup>2</sup> )	28	24	-0.43	0.12	-3.65	< <b>0.001</b>
Krill swarm length (m)	50	50	0.39	0.09	4.53	< <b>0.001</b>
Krill swarm height (m)	50	50	0.38	0.12	3.21	<b>0.002</b>
Krill swarm area (m <sup>2</sup> )	50	50	0.85	0.17	4.85	< <b>0.001</b>
Krill swarm biomass (g WW)	50	50	4.12	0.43	9.57	< <b>0.001</b>
Krill swarm density (g WW m <sup>-2</sup> )	50	50	1.35	0.34	3.97	< <b>0.001</b>
Median krill depth (m)	50	50	0.11	0.14	0.84	0.41
Depth-int krill density (g WW m <sup>-2</sup> )	50	50	0.28	0.28	0.98	0.33
Number of krill swarms per km	50	50	-0.16	0.14	-1.12	0.27

**Table 2.** Results from GLMMs assessing the differences in krill variables across survey legs within each penguin foraging region (Adélie and gentoo). All models used a gamma distribution and log link function. Significant results are indicated in bold.  $n = 10$  for all legs in each region.

Variable	Adélie Region				Gentoo Region			
	Coeff	SE	<i>t</i>	<i>p</i>	Coeff	SE	<i>t</i>	<i>p</i>
Krill swarm length (m)	0.04	0.03	1.38	0.18	0.008	0.04	0.17	0.86
Krill swarm height (m)	-0.05	0.04	-1.49	0.14	-0.10	0.06	-1.47	0.15
Krill swarm area (m <sup>2</sup> )	-0.06	0.05	-1.08	0.29	-0.15	0.10	-1.51	0.14
Krill swarm biomass (g WW)	-0.48	0.14	-3.49	<b>0.001</b>	-0.23	0.27	-0.83	0.41
Krill swarm density (g WW m <sup>-2</sup> )	-0.28	0.09	-3.06	<b>0.004</b>	-0.20	0.20	-1.01	0.32
Median krill depth (m)	0.15	0.06	2.61	<b>0.01</b>	-0.07	0.05	-1.44	0.16
Depth-int krill density (g WW m <sup>-2</sup> )	0.37	0.12	3.12	<b>0.003</b>	-0.02	0.15	-0.13	0.90
Number of krill swarms per km	0.14	0.04	3.45	<b>0.001</b>	0.10	0.08	1.31	0.20

## 5.8 Figures

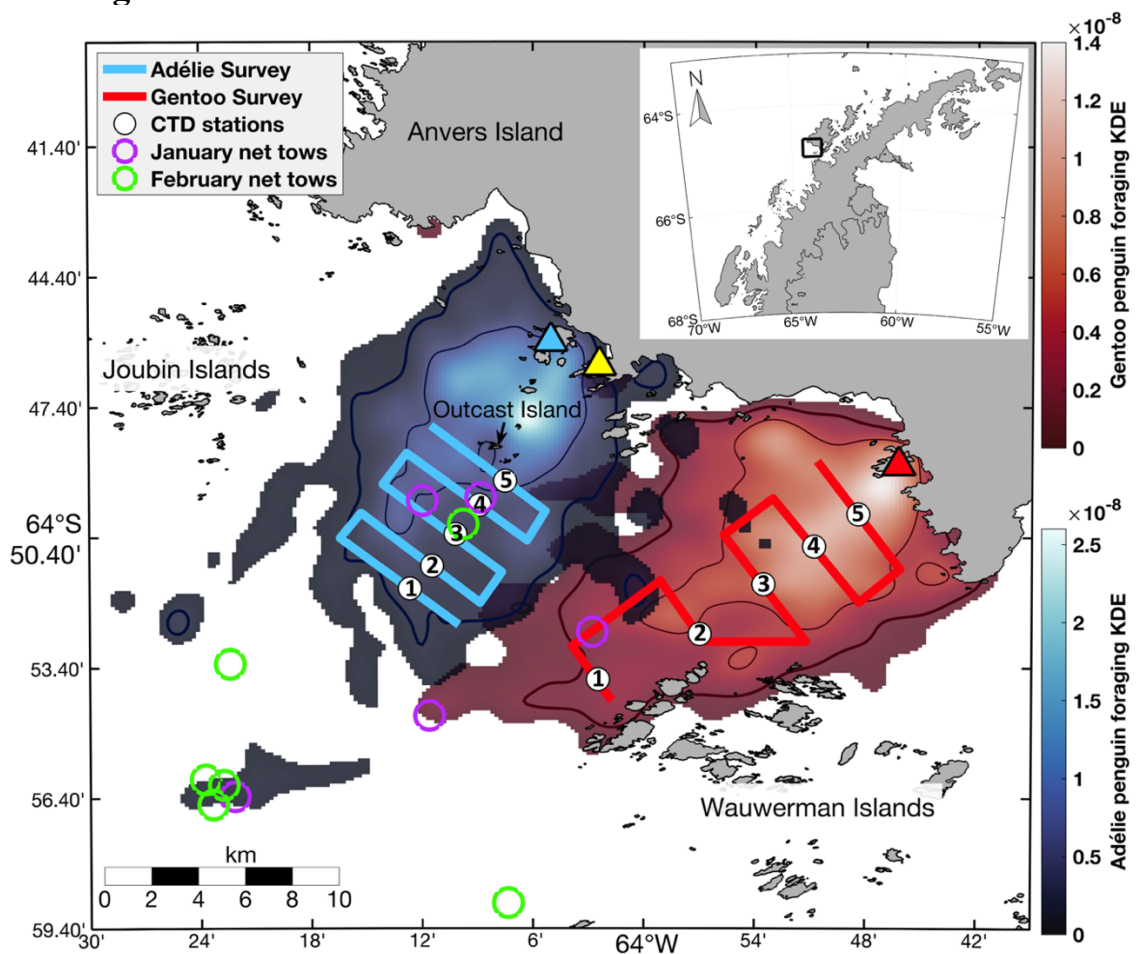


**Figure 1.** Map of the region south of Anvers Island along the West Antarctic Peninsula (inset) showing penguin foraging 2D kernel density estimates (KDE) based on foraging dives from satellite tag data from 2009 to 2019 (blue = Adélie foraging region, red = gentoo foraging region). The outer extent of the colored area is the 90% KDE, the thick line is the 80% KDE, and the thin line is the 50% KDE. Overlaid are the locations of the acoustic surveys, CTD profiling stations, and net tows. The blue triangle represents Adélie penguin colonies on Humble/Torgerson Islands, the red triangle represents the gentoo penguin colony on Biscoe Point, and the yellow triangle represents Palmer Station. Survey leg numbers are labeled 1-5 in black for each foraging region.

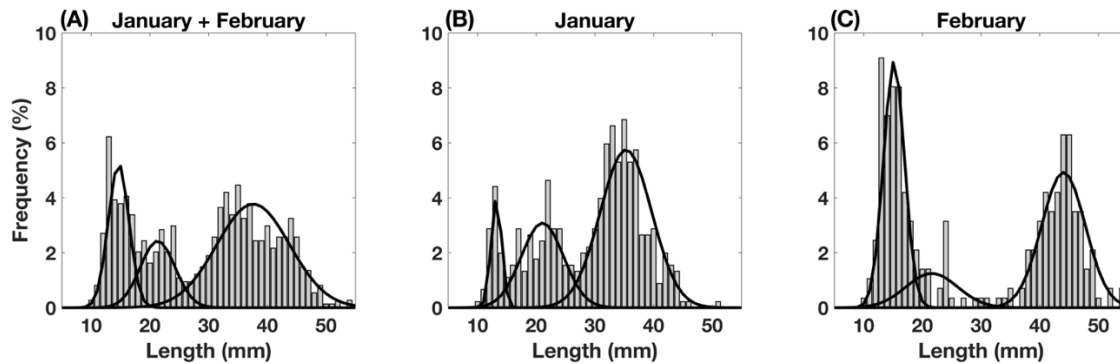


**Figure 2.** *Euphausia superba* length frequency distributions in the nearshore Palmer Deep canyon for (A) January and February combined (11 net tows, 739 krill measured), (B) January 6 to 8, 2019 (5 net tows, 453 krill measured), and for (C) February 3 to 5, 2019 (6 net tows, 286 krill measured). Black lines indicate the best component fits for each krill mode based on gaussian mixture models.

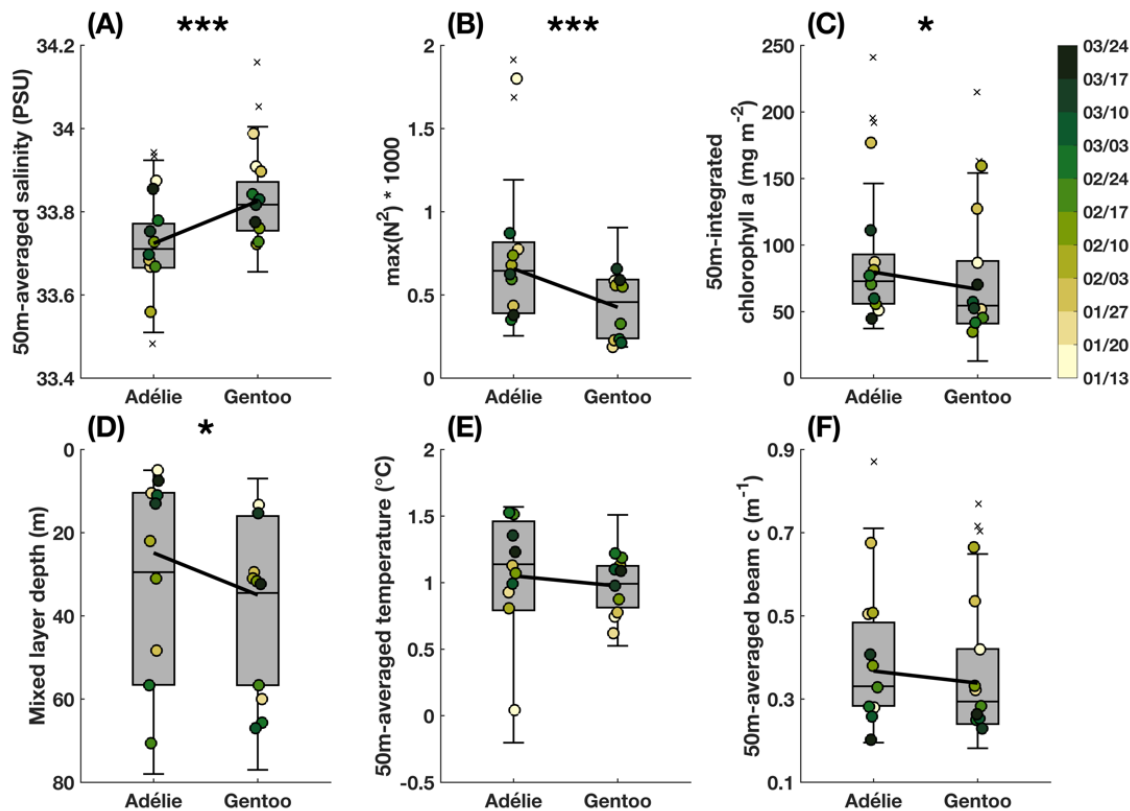


**Figure 3.** Differences in (A) 50 m-averaged salinity, (B)  $\max(N^2)$ , (C) 50 m-integrated chlorophyll *a*, (D) MLD, (E) 50 m-averaged temperature, and (F) 50 m-averaged beam *c* between the Adélie and gento survey regions. In each box plot, the horizontal line represents the median value, the top and bottom box limits represent the 25<sup>th</sup> and 75<sup>th</sup> percentiles, whiskers represent the full range of non-outlier observations, and x's represent outliers. The colored points are the mean values for each paired sampling day. Black lines indicate GLMM fits and asterisks indicate GLMM significance levels in Table 1 (\*  $0.01 < p \leq 0.05$ , \*\*\*  $p \leq 0.001$ , absence of asterisks indicates  $p > 0.05$ ). See Table 1 for *n* values.

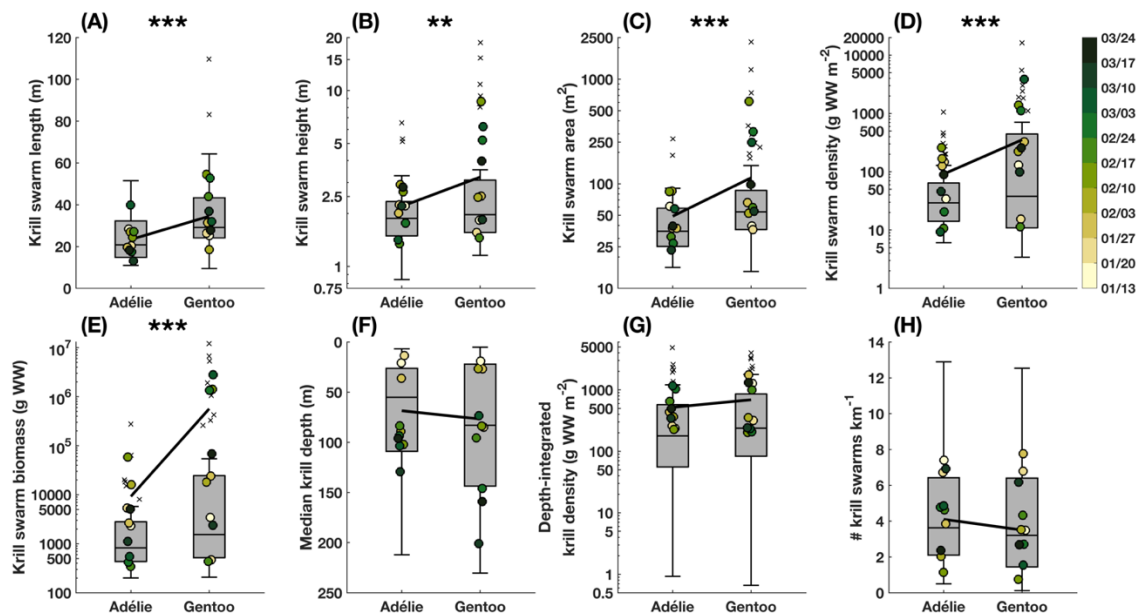


**Figure 4.** Differences in (A) krill swarm length, (B) krill swarm height, (C) krill swarm area, (D) krill swarm density, (E) krill swarm biomass, (F) median krill depth, (G) depth-integrated krill density, and (H) the number of krill swarms per km between the Adélie and gento survey regions. In each box plot, the horizontal line represents the median value, the top and bottom box limits represent the 25<sup>th</sup> and 75<sup>th</sup> percentiles, whiskers represent the full range of non-outlier observations, and x's represent outliers. The colored points are the mean values for each paired sampling day. Black lines indicate GLMM fits and asterisks indicate GLMM significance levels in Table 1 (\*\*  $p \leq 0.01$ , \*\*\*  $p \leq 0.001$ , absence of asterisks indicates  $p > 0.05$ ). See Table 1 for  $n$  values.

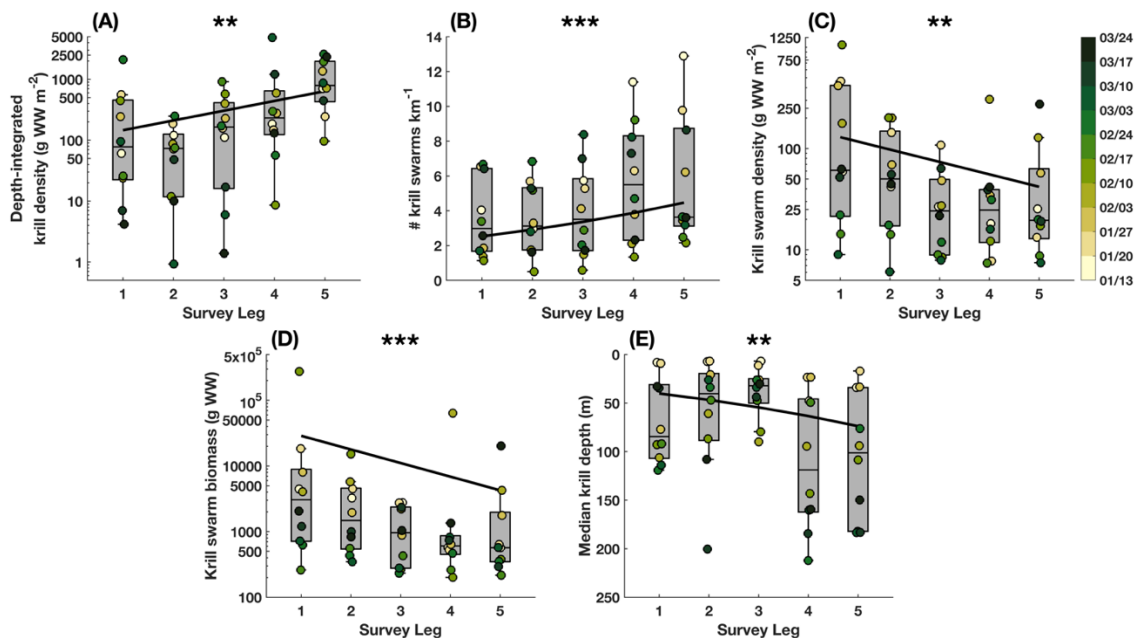


**Figure 5.** Differences in (A) depth-integrated krill density, (B) the number of krill swarms per km, (C) krill swarm density, (D) krill swarm biomass, and (E) median krill depth across the five survey legs of the Adélie survey, with survey leg 1 located offshore and leg 5 located inshore. In each box plot, the horizontal line represents the median value, the top and bottom box limits represent the 25<sup>th</sup> and 75<sup>th</sup> percentiles, and whiskers represent the full range of non-outlier observations. The colored points are the values for each paired sampling day. Black lines indicate GLMM fits and asterisks indicate GLMM significance levels in Table 2 (\*\*  $p \leq 0.01$ , \*\*\*  $p \leq 0.001$ , absence of asterisks indicates  $p > 0.05$ ).  $n = 10$  for all.

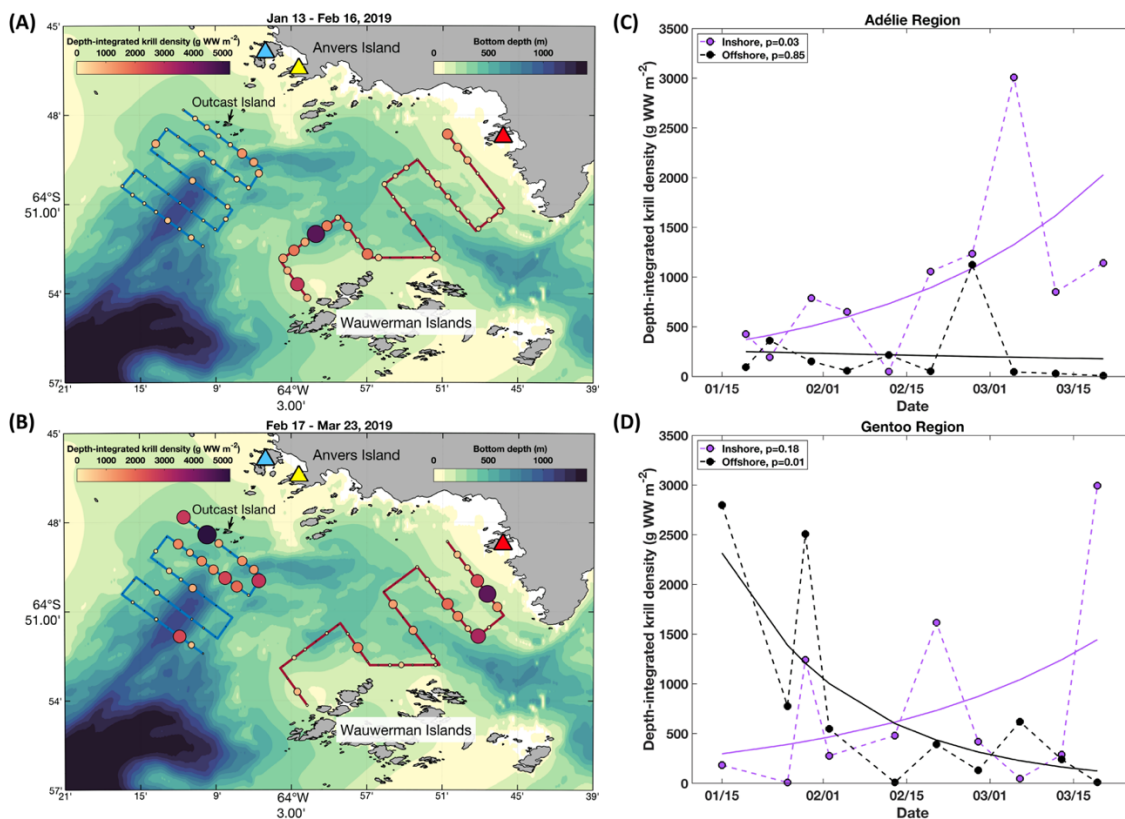


**Figure 6.** Seasonal spatiotemporal trends in krill biomass. Maps of mean depth-integrated krill density with the size of the circle scaled to density for roughly one month periods during the early and late austral summer: **(A)** January 13 to February 16, 2019 ( $n = 5$  surveys) and **(B)** February 17 to March 23, 2019 ( $n = 5$  surveys). The blue triangle represents Adélie penguin colonies on Humble/Torgerson Islands, the red triangle represents the gentoo penguin colony on Biscoe Point, and the yellow triangle represents Palmer Station. Time series of mean depth-integrated krill density for the inshore two survey legs (purple dots) compared to the offshore two survey legs (black dots) for the **(C)** Adélie and **(D)** gentoo penguin foraging regions. Solid lines indicate GLM fits (see Supplementary Tables 2 and 3) with model  $p$ -values indicated in subplot legends.

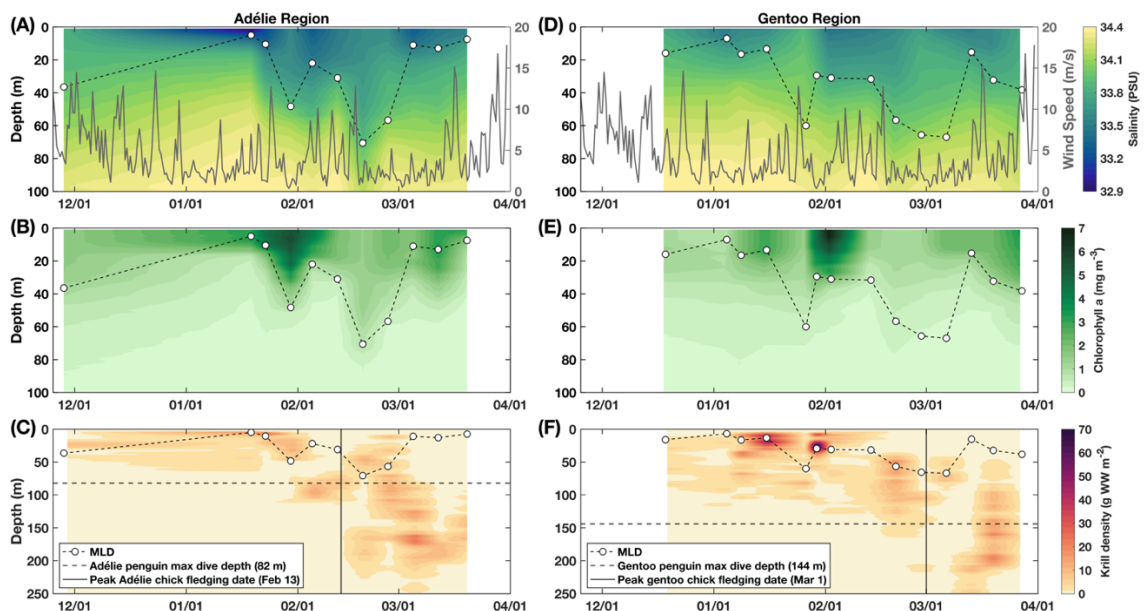


**Figure 7.** Time series of physical and biological properties in the (A-C) Adélie and (D-F) gentoo penguin foraging regions from November 2018 to March 2019. (A and D) Interpolated vertical cross-sections of daily averaged salinity overlaid with MLD (dashed line) and 12-hour averaged wind speed (gray line). (B and E) Interpolated vertical cross-sections of daily averaged chlorophyll *a* overlaid with MLD (dashed line). (C and F) Interpolated vertical cross-sections of daily averaged krill density overlaid with MLD (dashed line). Horizontal dashed lines indicate the maximum dive depth for Adélie and gentoo penguins (82 m and 144 m, respectively) based on five summers of data from Pickett et al. (2018). Vertical solid lines indicate peak penguin chick fledging dates (day when the most chicks fledged) in 2019 for each species (February 13 for Adélie penguins and March 1 for gentoo penguins; methods in Chapman et al. 2010).

## 5.9 Supporting Information

**Table S1.** Results from GLMMs assessing the differences in environmental variables across survey legs within each penguin foraging region (Adélie and gentoo). Models for 50 m averaged temperature and 50 m averaged salinity used a normal distribution and identity link function while all other models used gamma distribution and log link function. For 50 m averaged temperature, 50 m averaged salinity, 50 m integrated chlorophyll *a*, and 50 m averaged beam *c*,  $n = 9, 8, 9, 9, 10$  for legs 1-5 respectively in the Adélie region and  $n = 9, 10, 10, 10, 10$  for legs 1-5 respectively in the gentoo region. For MLD and  $\max(N^2)$ ,  $n = 5, 5, 5, 6, 7$  for legs 1-5 respectively in the Adélie region and  $n = 4, 5, 5, 8, 2$  for legs 1-5 respectively in the gentoo region. Weather occasionally prevented profiling at some CTD stations, and some MLD profiles failed to meet the QI threshold, resulting in  $n < 10$  for those CTD-derived variables.

Variable	Adélie Region				Gentoo Region			
	Coeff	SE	<i>t</i>	<i>p</i>	Coeff	SE	<i>t</i>	<i>p</i>
50 m avg temperature (°C)	0.02	0.02	0.86	0.39	0.007	0.01	0.53	0.60
50 m avg salinity (PSU)	0.005	0.005	0.95	0.35	0.007	0.006	1.23	0.23
50 m int chlorophyll <i>a</i> (mg m <sup>-2</sup> )	-0.02	0.02	-0.77	0.45	-0.05	0.03	-1.47	0.15
50 m avg beam <i>c</i> (m <sup>-1</sup> )	-0.006	0.01	-0.43	0.67	-0.0003	0.02	-0.02	0.99
MLD (m)	0.0004	0.04	0.01	0.99	0.03	0.09	0.30	0.76
Max(N <sup>2</sup> )	0.04	0.06	0.63	0.53	0.04	0.05	0.70	0.49

**Table S2.** Results from GLMs assessing temporal change of variables on the inshore two survey legs combined and the offshore two survey legs combined within the Adélie penguin foraging region. Models for 50 m averaged temperature and 50 m averaged salinity used a normal distribution and identity link function while all other models used gamma distribution and log link function. Significant results are indicated in bold. Weather occasionally prevented profiling at some CTD stations, and some MLD profiles failed to meet the QI threshold, resulting in  $n < 10$  for those CTD-derived variables.

Variable	Inshore Survey Legs					Offshore Survey Legs				
	<i>n</i>	Coeff	SE	<i>t</i>	<i>p</i>	<i>n</i>	Coeff	SE	<i>t</i>	<i>p</i>
50 m avg temperature (°C)	10	0.01	0.006	1.74	0.12	9	0.02	0.008	2.43	<b>0.05</b>
50 m avg salinity (PSU)	10	0.002	0.001	1.44	0.19	9	-0.0008	0.002	-0.40	0.70
50 m int chlorophyll <i>a</i> (mg m <sup>-2</sup> )	10	-0.009	0.007	-1.31	0.23	9	0.002	0.009	0.20	0.85
50 m avg beam <i>c</i> (m <sup>-1</sup> )	10	-0.01	0.005	-2.89	<b>0.02</b>	9	-0.006	0.006	-0.99	0.35
MLD (m)	8	0.02	0.02	1.35	0.23	6	-0.04	0.02	-1.70	0.16
Max(N <sup>2</sup> )	8	-0.02	0.009	-1.84	0.12	6	0.001	0.01	0.13	0.90
Krill swarm length (m)	10	-0.002	0.006	-0.41	0.70	10	-0.006	0.007	-0.78	0.46
Krill swarm height (m)	10	0.0009	0.008	0.12	0.91	10	-0.006	0.008	-0.80	0.45
Krill swarm area (m <sup>2</sup> )	10	-0.004	0.01	-0.38	0.71	10	-0.02	0.01	-1.23	0.26
Krill swarm biomass (g WW)	10	-0.01	0.03	-0.38	0.72	10	-0.07	0.04	-1.58	0.15
Krill swarm density (g WW m <sup>-2</sup> )	10	-0.005	0.02	-0.21	0.84	10	-0.03	0.03	-1.19	0.27
Median krill depth (m)	10	0.03	0.008	4.12	<b>0.003</b>	10	0.04	0.01	4.18	<b>0.003</b>
Depth-int krill density (g WW m <sup>-2</sup> )	10	0.03	0.01	2.61	<b>0.03</b>	10	-0.006	0.03	-0.20	0.85
Number of krill swarms per km	10	-0.009	0.008	-1.03	0.33	10	0.0007	0.01	0.07	0.95

**Table S3.** Results from GLMs assessing temporal change of variables on the inshore two survey legs combined and the offshore two survey legs combined within the gentoo penguin foraging region. Models for 50 m averaged temperature and 50 m averaged salinity used a normal distribution and identity link function while all other models used gamma distribution and log link function. Significant results are indicated in bold. Weather occasionally prevented profiling at some CTD stations, and some MLD profiles failed to meet the QI threshold, resulting in  $n < 10$  for those CTD-derived variables.

Variable	Inshore Survey Legs					Offshore Survey Legs				
	<i>n</i>	Coeff	SE	<i>t</i>	<i>p</i>	<i>n</i>	Coeff	SE	<i>t</i>	<i>p</i>
50 m avg temperature (°C)	10	0.007	0.003	2.52	<b>0.04</b>	10	0.007	0.003	2.08	0.07
50 m avg salinity (PSU)	10	-0.003	0.002	-2.07	0.07	10	-0.0005	0.001	-0.46	0.66
50 m int chlorophyll <i>a</i> (mg m <sup>-2</sup> )	10	-0.005	0.009	-0.59	0.57	10	-0.02	0.007	-2.18	0.06
50 m avg beam <i>c</i> (m <sup>-1</sup> )	10	-0.009	0.005	-1.79	0.11	10	-0.02	0.004	-3.80	<b>0.005</b>
MLD (m)	10	0.01	0.01	1.19	0.27	7	-0.003	0.01	-0.19	0.86
Max(N <sup>2</sup> )	10	0.002	0.01	0.17	0.87	7	0.004	0.007	0.61	0.57
Krill swarm length (m)	10	0.008	0.009	0.95	0.37	10	0.001	0.005	0.26	0.80
Krill swarm height (m)	10	-0.005	0.01	-0.38	0.71	10	0.01	0.01	0.94	0.37
Krill swarm area (m <sup>2</sup> )	10	-0.02	0.04	-0.41	0.69	10	0.01	0.01	0.98	0.36
Krill swarm biomass (g WW)	10	-0.12	0.05	-2.61	<b>0.03</b>	10	-0.009	0.04	-0.23	0.83
Krill swarm density (g WW m <sup>-2</sup> )	10	-0.05	0.03	-1.54	0.16	10	-0.02	0.03	-0.71	0.50
Median krill depth (m)	10	0.03	0.008	4.03	<b>0.004</b>	10	0.03	0.008	3.81	<b>0.005</b>
Depth-int krill density (g WW m <sup>-2</sup> )	10	0.03	0.02	1.47	0.18	10	-0.05	0.01	-3.16	<b>0.01</b>
Number of krill swarms per km	10	0.0008	0.01	0.08	0.94	10	-0.02	0.01	-1.42	0.19

**Table S4.** Results from GLMs assessing temporal change of variables within each penguin foraging region (Adélie and gentoo).

Models for 50 m averaged temperature and 50 m averaged salinity used a normal distribution and identity link function while all other models used gamma distribution and log link function. Significant results are indicated in bold.

Variable	Adélie Region					Gentoo Region				
	<i>n</i>	Coeff	SE	<i>t</i>	<i>p</i>	<i>n</i>	Coeff	SE	<i>t</i>	<i>p</i>
50 m avg temperature (°C)	10	0.01	0.006	2.34	<b>0.05</b>	10	0.006	0.003	2.45	<b>0.04</b>
50 m avg salinity (PSU)	10	0.001	0.002	0.75	0.48	10	-0.002	0.001	-1.50	0.17
50 m int chlorophyll <i>a</i> (mg m <sup>-2</sup> )	10	-0.006	0.008	-0.77	0.46	10	-0.01	0.008	-1.43	0.19
50 m avg beam <i>c</i> (m <sup>-1</sup> )	10	-0.01	0.005	-2.22	0.06	10	-0.01	0.004	-3.02	<b>0.02</b>
MLD (m)	10	-0.002	0.01	-0.16	0.88	10	0.006	0.008	0.73	0.49
Max(N <sup>2</sup> )	10	-0.01	0.007	-1.95	0.09	10	0.003	0.008	0.39	0.71
Krill swarm length (m)	10	-0.004	0.005	-0.77	0.46	10	0.005	0.006	0.84	0.42
Krill swarm height (m)	10	-0.0004	0.004	-0.10	0.92	10	-0.005	0.01	-0.42	0.68
Krill swarm area (m <sup>2</sup> )	10	-0.006	0.006	-0.94	0.37	10	-0.002	0.02	-0.09	0.93
Krill swarm biomass (g WW)	10	-0.01	0.01	-0.98	0.36	10	-0.09	0.05	-1.87	0.10
Krill swarm density (g WW m <sup>-2</sup> )	10	-0.02	0.02	-1.01	0.34	10	-0.04	0.03	-1.34	0.22
Median krill depth (m)	10	0.04	0.008	4.72	<b>0.002</b>	10	0.03	0.008	3.81	<b>0.005</b>
Depth-int krill density (g WW m <sup>-2</sup> )	10	0.02	0.008	2.39	<b>0.04</b>	10	-0.006	0.01	-0.43	0.68
Number of krill swarms per km	10	-0.004	0.008	-0.50	0.63	10	-0.007	0.009	-0.77	0.46

## 6. Summary and Conclusions

The Antarctic coastal ocean is a dynamic environment with large seasonal fluctuations in solar radiation, sea ice coverage, meltwater inputs, and wind-driven vertical mixing. Organisms have developed specialized responses to these seasonal cycles, using environmental cues to regulate timing, behavior, and physiology to optimize growth and reproductive success. The result is an immensely productive ecosystem fueled by large phytoplankton blooms that sustain abundant populations of krill, in turn feeding the iconic penguins, whales, and seals that define this region (Ross et al. 1996). To truly understand the long-term climate impacts on WAP ecosystems, it is critical to consider physical changes and organismal responses for the entire phytoplankton growing season (austral spring to autumn), which was the primary goal of this dissertation.

Novel technology was invaluable in elucidating seasonal patterns near Palmer Station. Chapters 2 and 3 used an Imaging FlowCytobot to collect phytoplankton taxonomy and cell size information at species-level resolution to characterize seasonal succession patterns in response to environmental drivers. In Chapter 2, a convolutional neural network was developed to automatically sort WAP phytoplankton images, which presents future opportunities for characterizing phytoplankton community species and size diversity in near-real time (e.g., in the field). Using this technology, Chapter 3 documented important seasonal events such as recurrent blooms of large-celled diatoms following sea ice retreat, mid-summer cryptophyte blooms, and a massive, small-celled pennate diatom bloom in early February 2019. In Chapter 4, 12-years of autonomous underwater glider deployments were paired with a photoacclimation model to create a

seasonal climatology of phytoplankton bloom phenology, capturing a recurrent phase shift between at the beginning of February in both physical and phytoplankton physiology variables. In Chapter 5, new rigid-hulled inflatable boats at Palmer Station allowed for seasonal acoustic surveys of krill within adjacent Adélie and gentoo penguin foraging regions, highlighting large local variability in oceanographic properties and krill availability, and the seasonal migration of adult krill inshore and to deeper depths.

An important theme of this dissertation was the role the physical environment plays in shaping lower trophic level dynamics. Light availability triggers the initiation of the growing season (Chapter 3), changes in phytoplankton photophysiology (Chapter 4), and the depth of krill diel vertical migration (Chapter 5). High winter sea ice extent and slow retreat from the Palmer region led to high summer phytoplankton biomass, and an increase in meteoric meltwater from late spring to autumn drove a shift towards smaller phytoplankton cells (Chapter 3). Increased wind-driven mixing in February brought sedimentary iron to surface waters, causing a large autumn phytoplankton bloom characterized by small, pennate diatoms (Chapter 3) with increased growth rates and high cellular chlorophyll concentrations (Chapter 4). Differing physical dynamics (e.g., current speeds, MLD) in regions less than 10 km apart led to significantly different krill swarming behaviors (Chapter 5). These relationships emphasize the importance of studying plankton ecology on seasonal scales to contextualize interannual and long-term trends.

Underlying our results are significant environmental changes along the WAP. We found that shorter duration sea ice seasons led to decreased phytoplankton biomass and lower proportions of diatoms, and that spring bloom initiation is tightly coupled to the

timing of sea ice retreat (Chapter 3). From 1979 to 2011, annual ice season duration decreased by 3.3 months, and sea ice retreat advanced by 1.3 months (Stammerjohn et al. 2012). A continuation of these trends could exacerbate phytoplankton decreases and shifts to non-diatom species, and advance the spring bloom leading to predator-prey mismatches (Cushing 1990). Increased cloud cover and wind-driven mixing from 1978 to 2006 reduced light levels in the surface mixed layer (Montes-Hugo et al. 2009), which should decrease phytoplankton growth rates; however, we saw an increase in February growth rates due to iron increases (Chapter 4). Therefore, continued increases in wind speeds could have a complicated response that highlights the importance of the balance between light and nutrient availability for phytoplankton growth, species composition, and size. From late spring to autumn, we also saw decreased phytoplankton cell size concurrent with increases in meltwater inputs (Chapters 3). Thus, continued warming and melting along the WAP could increase the prevalence of smaller cells (Montes-Hugo et al. 2009; Cook et al. 2016).

A reduction in phytoplankton biomass could lead to less successful krill recruitment (Saba et al. 2014), and therefore greater seasonal fluctuations of krill abundance near penguin colonies. Shifts to smaller phytoplankton cells could cause shifts to smaller zooplankton predators in response (e.g., from krill to microzooplankton), resulting in a microbial food web with reduced carbon cycling (Sailley et al. 2013). Additionally, increases in the frequency of salp blooms (Atkinson et al. 2004) could greatly increase grazing rates and decrease phytoplankton biomass further. Warmer waters and less sea ice are also expected to impact krill growth and lipid accumulation (Ruck et al. 2014; Klein et al. 2018). Less consistent prey availability, a changing

zooplankton community, and less nutritious krill would likely increase penguin foraging efforts and decrease breeding success (Fraser and Hofmann 2003; Chapman et al. 2011). For an already declining Adélie penguin population in the Palmer region, the results could be devastating.

Further research is needed to fully understand how significant these changes might be, as many open questions remain. Chapter 3 showed the tight link between sea ice retreat and the spring phytoplankton bloom, but it is unknown whether the advance in sea ice retreat since 1979 has driven advances in spring bloom timing, and how this might affect higher trophic levels. Chapter 4 showed important phase changes in summer phytoplankton physiology, however capturing the full annual bloom cycle and better quantifying loss terms (grazing and advection) would help clarify the drivers of bloom formation in coastal Antarctica. Additionally, more iron data concurrent with phytoplankton biomass and species composition data would help to confirm our hypothesis that the February pennate diatom bloom is driven by wind-driven iron resuspension (Chapters 3 and 4). Finally, Chapter 5 highlighted seasonal patterns in krill availability and the impact on foraging Adélie and gentoo penguins, but we do not know if the same patterns will hold in future years, and continued collection of this seasonal timeseries is crucial for contextualizing interannual variability in coastal krill abundance. Tackling these questions will give us a more complete understanding of how coastal ecosystems will respond and adapt to continued environmental changes along the WAP.

## 7. Acknowledgment of previous publications

**Chapter 2** has been published as a conference proceeding in *IEEE Xplore*:

Nardelli, S.C., P.C. Gray, and O. Schofield (2021). Developing a convolutional neural network to classify phytoplankton images collected with an Imaging FlowCytobot along the West Antarctic Peninsula. *MTS/IEEE OCEANS 2021 San Diego – Porto*. doi: 10.23919/OCEANS44145.2021.9706072.

**Chapter 3** is in prep to be submitted to the journal *Limnology and Oceanography*:

Nardelli, S.C., S.E. Stammerjohn, P.C. Gray, and O. Schofield. Coastal phytoplankton seasonal succession and diversity on the West Antarctic Peninsula. *Limnology and Oceanography* (in prep)

**Chapter 4** is in prep to be submitted to the journal *Frontiers of Marine Science*:

Nardelli, S.C. and O. Schofield. Using gliders to assess ecological drivers of phytoplankton bloom phenology in coastal Antarctica. *Frontiers of Marine Science* (in prep)

**Chapter 5** has been published in the journal *Limnology and Oceanography*:

Nardelli, S.C., M.A. Cimino, J.A. Conroy, W.R. Fraser, D.K. Steinberg, and O. Schofield (2021). Krill availability in adjacent Adélie and gentoo penguin foraging regions near Palmer Station, Antarctica. *Limnology and Oceanography*, 66: 2234-2250, doi: 10.1002/lno.11750.

## 8. References

- Ackley, S. F., and C. W. Sullivan. 1994. Physical controls on the development and characteristics of Antarctic sea ice biological communities - a review and synthesis. *Deep. Res. I* 41: 1583–1604.
- Annett, A. L., D. S. Carson, X. Crosta, A. Clarke, and R. S. Ganeshram. 2010. Seasonal progression of diatom assemblages in surface waters of Ryder Bay, Antarctica. *Polar Biol.* 33: 13–29, doi:10.1007/s00300-009-0681-7
- Ardyna, M., M. Babin, M. Gosselin, E. Devred, L. Rainville, and J.-éric Tremblay. 2014. Recent Arctic Ocean sea ice loss triggers novel fall phytoplankton blooms. *Geophys. Res. Lett.* 41: 6207–6212, doi:10.1002/2014GL061047
- Ardyna, M., and others. 2020. Environmental drivers of under-ice phytoplankton bloom dynamics in the Arctic Ocean. *Elementa* 8: 0–21, doi:10.1525/elementa.430
- Arrigo, K. R., G. L. van Dijken, and S. Bushinsky. 2008. Primary production in the Southern Ocean, 1997–2006. *J. Geophys. Res. Ocean.* 113: 1997–2006, doi:10.1029/2007JC004551
- Arteaga, L. A., E. Boss, M. J. Behrenfeld, T. K. Westberry, and J. L. Sarmiento. 2020. Seasonal modulation of phytoplankton biomass in the Southern Ocean. *Nat. Commun.*, doi:10.1038/s41467-020-19157-2
- Arteaga, L., M. Pahlow, and A. Oschlies. 2016. Modeled Chl:C ratio and derived estimates of phytoplankton carbon biomass and its contribution to total particulate organic carbon in the global surface ocean. *Global Biogeochem. Cycles* 30: 1791–1810, doi:10.1002/2016GB005458
- Atkinson, A., and others. 2019. Krill (*Euphausia superba*) distribution contracts southward during rapid regional warming. *Nat. Clim. Chang.* 9: 142–147, doi:10.1038/s41558-018-0370-z
- Atkinson, A., V. Siegel, E. Pakhomov, and P. Rothery. 2004. Long-term decline in krill stock and increase in salps within the Southern Ocean. *Nature* 432: 100–103, doi:10.1038/nature02950.1
- Beans, C., J. H. Hecq, P. Koubbi, C. Vallet, S. Wright, and A. Goffart. 2008. A study of the diatom-dominated microplankton summer assemblages in coastal waters from Terre Adélie to the Mertz Glacier, East Antarctica (139°E–145°E). *Polar Biol.* 31: 1101–1117, doi:10.1007/s00300-008-0452-x
- Behrenfeld, M. J. 2010. Abandoning sverdrup’s critical depth hypothesis on phytoplankton blooms. *Ecology* 91: 977–989, doi:10.1890/09-1207.1

- Behrenfeld, M. J., E. S. Boss, and K. H. Halsey. 2021a. Phytoplankton community structuring and succession in a competition-neutral resource landscape. *ISME Commun.* 1: 1–8, doi:10.1038/s43705-021-00011-5
- Behrenfeld, M. J., E. Boss, D. A. Siegel, and D. M. Shea. 2005. Carbon-based ocean productivity and phytoplankton physiology from space. *Global Biogeochem. Cycles* 19: 1–14, doi:10.1029/2004GB002299
- Behrenfeld, M. J., S. C. Doney, I. Lima, E. S. Boss, and D. A. Siegel. 2013. Annual cycles of ecological disturbance and recovery underlying the subarctic Atlantic spring plankton bloom. *Global Biogeochem. Cycles* 27: 526–540, doi:10.1002/gbc.20050
- Behrenfeld, M. J., K. H. Halsey, E. Boss, L. Karp-Boss, A. J. Milligan, and G. Peers. 2021b. Thoughts on the evolution and ecological niche of diatoms. *Ecol. Monogr.* 91: 1–25, doi:10.1002/ecm.1457
- Behrenfeld, M. J., and others. 2017. Annual boom-bust cycles of polar phytoplankton biomass revealed by space-based lidar. *Nat. Geosci.* 10: 118–122, doi:10.1038/ngeo2861
- Behrenfeld, M. J., and others. 2019. The North Atlantic Aerosol and Marine Ecosystem Study (NAAMES): Science motive and mission overview. *Front. Mar. Sci.* 6: 1–25, doi:10.3389/fmars.2019.00122
- Behrenfeld, M. J., and others. 2016. Revaluating ocean warming impacts on global phytoplankton. *Nat. Clim. Chang.* 6: 323–330, doi:10.1038/nclimate2838
- Bellacicco, M., G. Volpe, S. Colella, J. Pitarch, and R. Santoleri. 2016. Influence of photoacclimation on the phytoplankton seasonal cycle in the Mediterranean Sea as seen by satellite. *Remote Sens. Environ.* 184: 595–604, doi:10.1016/j.rse.2016.08.004
- Bernard, K. S., and others. 2017. Factors that affect the nearshore aggregations of Antarctic krill in a biological hotspot. *Deep. Res. Part I* 126: 139–147, doi:10.1016/j.dsr.2017.05.008
- Bernard, K. S., and others. 2018. The contribution of ice algae to the winter energy budget of juvenile Antarctic krill in years with contrasting sea ice conditions. *ICES J. Mar. Sci.* 76: 206–216, doi:10.1093/icesjms/fsy145
- Bernard, K. S., and D. K. Steinberg. 2013. Krill biomass and aggregation structure in relation to tidal cycle in a penguin foraging region off the Western Antarctic Peninsula. *ICES J. Mar. Sci.* 70: 834–849, doi:10.1093/icesjms/fst088

- Bernard, K. S., D. K. Steinberg, and O. M. E. Schofield. 2012. Summertime grazing impact of the dominant macrozooplankton off the Western Antarctic Peninsula. *Deep. Res. Part I Oceanogr. Res. Pap.* 62: 111–122, doi:10.1016/j.dsr.2011.12.015
- Biggs, T. E. G., S. Alvarez-Fernandez, C. Evans, K. D. A. Mojica, P. D. Rozema, H. J. Venables, D. W. Pond, and C. P. D. Brussaard. 2019. Antarctic phytoplankton community composition and size structure: importance of ice type and temperature as regulatory factors. *Polar Biol.* 42: 1997–2015, doi:10.1007/s00300-019-02576-3
- Boss, E., and M. Behrenfeld. 2010. In situ evaluation of the initiation of the North Atlantic phytoplankton bloom. *Geophys. Res. Lett.* 37: 1–5, doi:10.1029/2010GL044174
- Boss, E., and W. S. Pegau. 2001. Relationship of light scattering at an angle in the backward direction to the backscattering coefficient. *Appl. Opt.* 40: 5503, doi:10.1364/ao.40.005503
- Boss, E., and others. 2013. The characteristics of particulate absorption, scattering and attenuation coefficients in the surface ocean; Contribution of the Tara Oceans expedition. *Methods Oceanogr.* 7: 52–62, doi:10.1016/j.mio.2013.11.002
- Bost, C. A., J. Lage, and K. Putz. 1994. Maximum diving depth and diving patterns of the gentoo penguin *Pygoscelis papua* at the Crozet Islands. *Mar. Ornithol.* 22: 237–244.
- Boyd, P. W., and others. 2000. A mesoscale phytoplankton bloom in the polar Southern Ocean stimulated by iron fertilization. *Nature* 407: 695–702, doi:10.1038/35037500
- Briggs, N., M. J. Perry, I. Cetinic, C. Lee, E. D'Asaro, A. M. Gray, and E. Rehm. 2011. High-resolution observations of aggregate flux during a sub-polar North Atlantic spring bloom. *Deep. Res. Part I Oceanogr. Res. Pap.* 58: 1031–1039, doi:10.1016/j.dsr.2011.07.007
- Brown, M. S., D. R. Munro, C. J. Feehan, C. Sweeney, H. W. Ducklow, and O. M. Schofield. 2019. Enhanced oceanic CO<sub>2</sub> uptake along the rapidly changing West Antarctic Peninsula. *Nat. Clim. Chang.*, doi:10.1038/s41558-019-0552-3
- Carvalho, F., and others. 2019. Testing the Canyon Hypothesis: Evaluating light and nutrient controls of phytoplankton growth in penguin foraging hotspots along the West Antarctic Peninsula. *Limnol. Oceanogr.* 65: 455–470, doi:10.1002/lno.11313
- Carvalho, F., J. Kohut, M. J. Oliver, and O. Schofield. 2017. Defining the ecologically relevant mixed-layer depth for Antarctica's coastal seas. *Geophys. Res. Lett.* 44: 338–345, doi:10.1002/2016GL071205

- Carvalho, F., J. Kohut, M. J. Oliver, R. M. Sherrel, and O. Schofield. 2016. Mixing and phytoplankton dynamics in a submarine canyon in the West Antarctic Peninsula. *J. Geophys. Res. Ocean.* 121: 5069–5083, doi:10.1002/2016JC011650
- Chapman, E. W., E. E. Hofmann, D. L. Patterson, and W. R. Fraser. 2010. The effects of variability in Antarctic krill (*Euphausia superba*) spawning behavior and sex/maturity stage distribution on Adélie penguin (*Pygoscelis adeliae*) chick growth: A modeling study. *Deep. Res. Part II* 57: 543–558, doi:10.1016/j.dsr2.2009.10.005
- Chapman, E. W., E. E. Hofmann, D. L. Patterson, C. A. Ribic, and W. R. Fraser. 2011. Marine and terrestrial factors affecting Adélie penguin *Pygoscelis adeliae* chick growth and recruitment off the western Antarctic Peninsula. *Mar. Ecol. Prog. Ser.* 436: 273–289, doi:10.3354/meps09242
- Cimino, M. A., W. R. Fraser, D. L. Patterson-Fraser, V. S. Saba, and M. J. Oliver. 2014. Large-scale climate and local weather drive interannual variability in Adélie penguin chick fledging mass. *Mar. Ecol. Prog. Ser.* 513: 253–268, doi:10.3354/meps10928
- Cimino, M. A., M. A. Moline, W. R. Fraser, D. L. Patterson-Fraser, and M. J. Oliver. 2016. Climate-driven sympatry may not lead to foraging competition between congeneric top-predators. *Sci. Rep.* 6: 18820, doi:10.1038/srep18820
- Clarke, A., M. P. Meredith, M. I. Wallace, M. A. Brandon, and D. N. Thomas. 2008. Seasonal and interannual variability in temperature, chlorophyll and macronutrients in northern Marguerite Bay, Antarctica. *Deep. Res. Part II Top. Stud. Oceanogr.* 55: 1988–2006, doi:10.1016/j.dsr2.2008.04.035
- Cleary, A. C., E. G. Durbin, M. C. Casas, and M. Zhou. 2016. Winter distribution and size structure of Antarctic krill *Euphausia superba* populations in-shore along the West Antarctic Peninsula. *Mar. Ecol. Prog. Ser.* 552: 115–129, doi:10.3354/meps11772
- Conroy, J. A., C. S. Reiss, M. R. Gleiber, and D. K. Steinberg. 2020. Linking Antarctic krill larval supply and recruitment along the Antarctic Peninsula. *Integr. Comp. Biol.* 60: 1386–1400, doi:10.1093/icb/icaa111
- Constable, A. J., and others. 2014. Climate change and Southern Ocean ecosystems I: how changes in physical habitats directly affect marine biota. *Glob. Chang. Biol.* 1–22, doi:10.1111/gcb.12623
- Conti, S. G., and D. A. Demer. 2006. Improved parameterization of the SDWBA for estimating krill target strength. *ICES J. Mar. Sci.* 63: 928–935, doi:10.1016/j.icesjms.2006.02.007

- Cook, A. J., P. R. Holland, M. P. Meredith, T. Murray, A. Luckman, and D. G. Vaughan. 2016. Ocean forcing of glacier retreat in the western Antarctic Peninsula. *Science* 353: 283–285, doi:10.1126/science.aac0017
- Couto, N., D. G. Martinson, J. Kohut, and O. Schofield. 2017. Distribution of Upper Circumpolar Deep Water on the warming continental shelf of the West Antarctic Peninsula. *J. Geophys. Res. Ocean.* 122, doi:10.1002/2017JC012840
- Culhane, E., N. Haentjens, A. P. Chase, P. Gaube, and J. Morrill. 2020. Leveraging unsupervised methods to train image classification networks with fewer labelled inputs: Application to species classification of phytoplankton imagery from an Imaging Flow Cytometer. *Ocean Sciences Meeting*.
- Cushing, D. H. 1990. Plankton production and year-class strength in fish populations: An update of the match/mismatch hypothesis. *Adv. Mar. Bio.* 26: 249-293, doi: 10.1016/S0065-2881(08)60202-3
- Daly, K. L., and M. C. Macaulay. 1988. Abundance and distribution of krill in the ice edge zone of the Weddell Sea, austral spring 1983. *Deep Sea Res. Part A Oceanogr. Res. Pap.* 35: 21–41, doi:10.1016/0198-0149(88)90055-6
- Dierssen, H. M., R. C. Smith, and M. Vernet. 2002. Glacial meltwater dynamics in coastal waters west of the Antarctic peninsula. *Proc. Natl. Acad. Sci.* 99: 1790–1795, doi:10.1073/pnas.032206999
- Diner, N. 2001. Correction on school geometry and density: approach based on acoustic image simulation. *Aquat. Living Resour.* 14: 211–222, doi:10.1016/S0990-7440(01)01121-4
- Ducklow, H., and others. 2012. The marine system of the Western Antarctic Peninsula, p. 121–159. In A.D. Rogers, N.M. Johnston, E.J. Murphy, and A. Clarke [eds.], *Antarctic Ecosystems: An Extreme Environment in a Changing World*. Blackwell Publishing Ltd.
- Ducklow, H. W., and others. 2013. West Antarctic Peninsula: An ice-dependent coastal marine ecosystem in transition. *Oceanography* 26: 190–203, doi:10.5670/oceanog.2013.62
- Edwards, K. F. 2019. Mixotrophy in nanoflagellates across environmental gradients in the ocean. *Proc. Natl. Acad. Sci. U. S. A.* 116: 6211–6220, doi:10.1073/pnas.1814860116
- Edwards, M., and A. J. Richardson. 2004. Impact of climate change on marine pelagic phenology and trophic mismatch. *Nature* 430: 881–883, doi:10.1038/nature02808

- Eicken, H. 1992. The role of sea ice in structuring Antarctic ecosystems. *Polar Biol.* 12: 3–13, doi:10.1007/BF00239960
- Emslie, S. D. 2001. Radiocarbon dates from abandoned penguin colonies in the Antarctic Peninsula region. *Antarct. Sci.* 13: 289–295, doi:10.1017/S0954102001000414
- Eppley, R. W., and B. J. Peterson. 1979. Particulate organic matter flux and planktonic new production in the deep ocean. *Nature* 282: 677–680, doi:10.1038/282677a0
- Falkowski, P. G., and J. Laroche. 1991. Acclimation to spectral irradiance in algae. *J. Phycol.* 27: 8–14.
- Fielding, S., J. L. Watkins, M. A. Collins, P. Enderlein, and H. J. Venables. 2012. Acoustic determination of the distribution of fish and krill across the Scotia Sea in spring 2006, summer 2008 and autumn 2009. *Deep Sea Res. II* 59–60: 173–188, doi:10.1016/j.dsr2.2011.08.002
- Fielding, S., J. L. Watkins, P. N. Trathan, P. Enderlein, C. M. Waluda, G. Stowasser, G. A. Tarling, and E. J. Murphy. 2014. Interannual variability in Antarctic krill (*Euphausia superba*) density at South Georgia, Southern Ocean: 1997–2013. *ICES J. Mar. Sci.* 71: 2578–2588, doi:10.1093/icesjms/fsu104
- Finkel, Z. V., J. Beardall, K. J. Flynn, A. Quigg, T. A. V Rees, and J. A. Raven. 2010. Phytoplankton in a changing world: Cell size and elemental stoichiometry. *J. Plankton Res.* 32: 119–137, doi:10.1093/plankt/fbp098
- Folt, C. L., and C. W. Burns. 1999. Biological drivers of zooplankton patchiness. *Trends Ecol. Evol.* 14: 300–305, doi:10.1016/S0169-5347(99)01616-X
- Foote, K. G. 1990. Spheres for calibrating an eleven-frequency acoustic measurement system. *J. Cons. int. Explor. Mer.* 46: 284–286, doi:10.1093/icesjms/46.3.284
- Fox, J., and others. 2020. Phytoplankton growth and productivity in the Western North Atlantic: Observations of regional variability from the NAAMES field campaigns. *Front. Mar. Sci.* 7: 1–15, doi:10.3389/fmars.2020.00024
- Fraser, W. R., H. W. Ducklow, and S. F. Henley. 2020. Corrigendum to “Variability and change in the west Antarctic Peninsula marine system: Research priorities and opportunities” [*Progr. Oceanogr.* (2019) 208–237]. *Prog. Oceanogr.* 186: 102350, doi:10.1016/j.pocean.2020.102350
- Fraser, W. R., and E. E. Hofmann. 2003. A predator’s perspective on causal links between climate change, physical forcing and ecosystem response. *Mar. Ecol. Prog. Ser.* 265: 1–15, doi:10.3354/meps265001

- Fraser, W. R., and W. Z. Trivelpiece. 1996. Factors controlling the distribution of seabirds: winter-summer heterogeneity in the distribution of Adélie penguin populations, p. 257–272. In R.M. Ross, E.E. Hofmann, and L.B. Quetin [eds.], *Foundations for ecological research west of the Antarctic Peninsula*. American Geophysical Union.
- Frölicher, T. L., J. L. Sarmiento, D. J. Paynter, J. P. Dunne, J. P. Krasting, and M. Winton. 2015. Dominance of the Southern Ocean in anthropogenic carbon and heat uptake in CMIP5 models. *J. Clim.* 28: 862–886, doi:10.1175/JCLI-D-14-00117.1
- Garcia, M. D., and others. 2019. Effects of glacier melting on the planktonic communities of two Antarctic coastal areas (Potter Cove and Hope Bay) in summer. *Reg. Stud. Mar. Sci.* 30: 100731, doi:10.1016/j.rsma.2019.100731
- Garibotti, I. A., M. Vernet, and M. E. Ferrario. 2005. Annually recurrent phytoplanktonic assemblages during summer in the seasonal ice zone west of the Antarctic Peninsula (Southern Ocean). *Deep. Res. Part I Oceanogr. Res. Pap.* 52: 1823–1841, doi:10.1016/j.dsr.2005.05.003
- Garrison, D. L., S. F. Ackley, and K. R. Buck. 1983. A physical mechanism for establishing algal populations in frazil ice. *Nature* 306: 363–365, doi:10.1038/306363a0
- Garzio, L. M., and D. K. Steinberg. 2013. Microzooplankton community composition along the Western Antarctic Peninsula. *Deep. Res. Part I* 77: 36–49, doi:10.1016/j.dsr.2013.03.001
- Garzio, L. M., D. K. Steinberg, M. Erickson, and H. W. Ducklow. 2013. Microzooplankton grazing along the Western Antarctic Peninsula. *Aquat. Microb. Ecol.* 70: 215–232, doi:10.3354/ame01655
- Gast, R. J., Z. M. McKie-Krisberg, S. A. Fay, J. M. Rose, and R. W. Sanders. 2014. Antarctic mixotrophic protist abundances by microscopy and molecular methods. *FEMS Microbiol. Ecol.* 89: 388–401, doi:10.1111/1574-6941.12334
- Geider, R. J., and J. La Roche. 1994. The role of iron in phytoplankton photosynthesis, and the potential for iron-limitation of primary productivity in the sea. *Photosynth. Res.* 39: 275–301, doi:10.1007/BF00014588
- Gibbons, M. J., V. A. Spiridonov, and G. A. Tarling. 1999. Euphausiacea, p. 1241–1279. In D. Boltovskoy [ed.], *South Atlantic Zooplankton*. Backhuys Publishers.
- Gleiber, M. R., D. K. Steinberg, and O. M. E. Schofield. 2016. Copepod summer grazing and fecal pellet production along the Western Antarctic Peninsula. *J. Plankton Res.* 38: 732–750, doi:10.1093/plankt/fbv070

- Goes, J. I., and others. 2014. Influence of the Amazon River discharge on the biogeography of phytoplankton communities in the western tropical north Atlantic. *Prog. Oceanogr.* 120: 29–40, doi:10.1016/j.pocean.2013.07.010
- Gonçalves-Araujo, R., M. S. de Souza, V. M. Tavano, and C. A. E. Garcia. 2015. Influence of oceanographic features on spatial and interannual variability of phytoplankton in the Bransfield Strait, Antarctica. *J. Mar. Syst.* 142: 1–15, doi:10.1016/j.jmarsys.2014.09.007
- Graff, J. R., T. K. Westberry, A. J. Milligan, M. B. Brown, G. Dall, V. Van Dongen-vogels, K. M. Reifel, and M. J. Behrenfeld. 2015. Analytical phytoplankton carbon measurements spanning diverse ecosystems. *Deep. Res. I* 102: 16–25,
- Hall, A., and M. Visbeck. 2002. Synchronous variability in the Southern Hemisphere atmosphere, sea ice, and ocean resulting from the annular mode. *J. Clim.* 15: 3043–3057, doi:10.1175/1520-0442(2002)015<3043:SVITSH>2.0.CO;2
- Hamner, W. M., and P. P. Hamner. 2000. Behavior of Antarctic krill (*Euphausia superba*): schooling, foraging, and antipredatory behavior. *Can. J. Fish. Aquat. Sci.* 57: 192–202.
- Hasle, G. R., E. E. Syvertsen, K. A. Steidinger, K. Tangen, J. Throndsen, and B. R. Heimdal. 1997. Identifying marine phytoplankton, C.R. Tomas [ed.]. Academic Press.
- Hays, G. C. 2003. A review of the adaptive significance and ecosystem consequences of zooplankton diel vertical migrations M.B. Jones, A. Ingólfsson, E. Ólafsson, G. V Helgason, K. Gunnarsson, and J. Svavarsson [eds.]. *Hydrobiologia* 503: 163–170, doi:https://doi.org/10.1023/B:HYDR.0000008476.23617.b0
- Henson, S. A., H. S. Cole, J. Hopkins, A. P. Martin, and A. Yool. 2018. Detection of climate change-driven trends in phytoplankton phenology. *Glob. Chang. Biol.* 24: e101–e111, doi:10.1111/gcb.13886
- Hernando, M., I. R. Schloss, G. Malanga, G. O. Almandoz, G. A. Ferreyra, M. B. Aguiar, and S. Puntarulo. 2015. Effects of salinity changes on coastal Antarctic phytoplankton physiology and assemblage composition. *J. Exp. Mar. Bio. Ecol.* 466: 110–119, doi:10.1016/j.jembe.2015.02.012
- Hewitt, R. P., and others. 2004. Biomass of Antarctic krill in the Scotia Sea in January/February 2000 and its use in revising an estimate of precautionary yield. *Deep. Res. Part II* 51: 1215–1236, doi:10.1016/j.dsr2.2004.06.011

- Höfer, J., R. Giesecke, M. J. Hopwood, V. Carrera, E. Alarcón, and H. E. González. 2019. The role of water column stability and wind mixing in the production/export dynamics of two bays in the Western Antarctic Peninsula. *Prog. Oceanogr.* 174: 105–116, doi:10.1016/j.pocean.2019.01.005
- Hudson, K., and others. 2021. A recirculating eddy promotes subsurface particle retention in an Antarctic biological hotspot. *J. Geophys. Res. Ocean.* 126: 1–19, doi:10.1029/2021JC017304
- Hunter-Cevera, K. R., M. G. Neubert, R. J. Olson, A. R. Solow, A. Shalapyonok, and H. M. Sosik. 2016. Physiological and ecological drivers of early spring blooms of a coastal phytoplanktoner. *Science* 354: 326–329.
- Intergovernmental Oceanographic Commission. 1994. Protocols for the Joint Global Ocean Flux Study (JGOFS) core measurements, A. Knap, A. Michaels, A. Close, H. Ducklow, and A. Dickson [eds.]. UNESCO-IOC.
- Kaňa, R., E. Kotabová, R. Sobotka, and O. Prášil. 2012. Non-photochemical quenching in cryptophyte alga *Rhodomonas salina* is located in chlorophyll a/c antennae. *PLoS One* 7, doi:10.1371/journal.pone.0029700
- Kana, T. M., R. J. Geider, and C. Critchley. 1997. Regulation of photosynthetic pigments in micro-algae by multiple environmental factors: A dynamic balance hypothesis. *New Phytol.* 137: 629–638, doi:10.1046/j.1469-8137.1997.00857.x
- Kavanaugh, M. T., and others. 2015. Effect of continental shelf canyons on phytoplankton biomass and community composition along the western Antarctic Peninsula. *Mar. Ecol. Prog. Ser.* 524: 11–26, doi:10.3354/meps11189
- Key, T., A. McCarthy, D. A. Campbell, C. Six, S. Roy, and Z. V. Finkel. 2010. Cell size trade-offs govern light exploitation strategies in marine phytoplankton. *Environ. Microbiol.* 12: 95–104, doi:10.1111/j.1462-2920.2009.02046.x
- Kim, H., S. C. Doney, R. A. Iannuzzi, M. P. Meredith, D. G. Martinson, and H. W. Ducklow. 2016. Climate forcing for dynamics of dissolved inorganic nutrients at Palmer Station, Antarctica: An interdecadal (1993–2013) analysis. *J. Geophys. Res. Biogeosciences* 121: 2369–2389, doi:10.1002/2015JG003311
- Kim, H., and others. 2018. Inter-decadal variability of phytoplankton biomass along the coastal West Antarctic Peninsula. *Phil Trans R Soc A* 376: 1–21.
- Klein, E. S., S. L. Hill, J. T. Hinke, T. Phillips, and G. M. Watters. 2018. Impacts of rising sea temperature on krill increase risks for predators in the Scotia Sea. *PLoS One* 13: e0191011, doi:10.1371/journal.pone.0191011

- Klevjer, T. A., G. A. Tarling, and S. Fielding. 2010. Swarm characteristics of Antarctic krill *Euphausia superba* relative to the proximity of land during summer in the Scotia Sea. *Mar. Ecol. Prog. Ser.* 409: 157–170, doi:10.3354/meps08602
- Kohut, J. T., P. Winsor, H. Statscewich, M. J. Oliver, E. Fredj, N. Couto, K. Bernard, and W. Fraser. 2018. Variability in summer surface residence time within a West Antarctic Peninsula biological hotspot. *Philos. Trans. R. Soc. A* 376: 20170165, doi:10.1098/rsta.2017.0165
- Kozlowski, W. A., D. Deutschman, I. Garibotti, C. Trees, and M. Vernet. 2011. An evaluation of the application of CHEMTAX to Antarctic coastal pigment data. *Deep. Res. Part I Oceanogr. Res. Pap.* 58: 350–364, doi:10.1016/j.dsr.2011.01.008
- Lafond, A., and others. 2019. Late spring bloom development of pelagic diatoms in Baffin Bay. *Elementa* 7, doi:10.1525/elementa.382
- Lawson, G. L., P. H. Wiebe, T. K. Stanton, and C. J. Ashjian. 2008. Euphausiid distribution along the Western Antarctic Peninsula- Part A: Development of robust multi-frequency acoustic techniques to identify euphausiid aggregations and quantify euphausiid size, abundance, and biomass. *Deep. Res. Part II Top. Stud. Oceanogr.* 55: 412–431, doi:10.1016/j.dsr2.2007.11.014
- LeCun, Y., Y. Bengio, and G. Hinton. 2015. Deep learning. *Nature* 521: 436–444, doi:10.1038/nature14539
- van Leeuwe, M. A., and others. 2018. Microalgal community structure and primary production in Arctic and Antarctic sea ice: A synthesis. *Elementa* 6, doi:10.1525/elementa.267
- van Leeuwe, M., A. Webb, H. Venables, R. Visser, M. Meredith, J. Elzenga, and J. Stefels. 2019. Annual patterns in phytoplankton phenology in Antarctic coastal waters explained by environmental drivers. *Limnol. Oceanogr.* 1–18, doi:10.1002/lno.11477
- Letelier, R. M., D. M. Karl, M. R. Abbott, and R. R. Bidigare. 2004. Light driven seasonal patterns of chlorophyll and nitrate in the lower euphotic zone of the North Pacific Subtropical Gyre. *Limnol. Oceanogr.* 49: 508–519, doi:10.4319/lo.2004.49.2.0508
- Li, W. K. W., F. A. McLaughlin, C. Lovejoy, and E. C. Carmack. 2009. Smallest algae thrive as the Arctic ocean freshens. *Science* 326: 539, doi:10.1126/science.1179798
- Lorbacher, K., D. Dommenges, P. P. Niiler, and A. Köhl. 2006. Ocean mixed layer depth: A subsurface proxy of ocean-atmosphere variability. *J. Geophys. Res.* 111: C07010, doi:10.1029/2003JC002157

- Maeda, E. E., F. Lisboa, L. Kaikkonen, K. Kallio, S. Koponen, V. Brotas, and S. Kuikka. 2019. Temporal patterns of phytoplankton phenology across high latitude lakes unveiled by long-term time series of satellite data. *Remote Sens. Environ.* 221: 609–620, doi:10.1016/j.rse.2018.12.006
- Margalef, R. 1978. Life-forms of phytoplankton as survival alternatives in an unstable environment. *Oceanol. Acta* 1: 493–509, doi:10.1007/BF00202661
- Martinson, D. G., and D. C. McKee. 2012. Transport of warm upper circumpolar deep water onto the Western Antarctic Peninsula Continental Shelf. *Ocean Sci.* 8: 433–442, doi:10.5194/os-8-433-2012
- Mauchline, J. 1980. Measurement of body length of *Euphausia superba* Dana, p. 1–9. In *BIOMASS Handbook*, No. 4. Scientific Committee Antarctic Research.
- McClatchie, S., and C. M. Boyd. 1983. Morphological study of sieve efficiencies and mandibular surfaces in the Antarctic krill, *Euphausia superba*. *Can. J. Fish. Aquat. Sci.* 40: 955–967, doi:10.1139/f83-122
- Mendes, C. R. B., V. M. Tavano, T. S. Dotto, R. Kerr, M. S. de Souza, C. A. E. Garcia, and E. R. Secchi. 2017. New insights on the dominance of cryptophytes in Antarctic coastal waters: A case study in Gerlache Strait. *Deep. Res. Part II Top. Stud. Oceanogr.* 1–10, doi:10.1016/j.dsr2.2017.02.010
- Mendes, C. R. B., V. M. Tavano, M. C. Leal, M. S. de Souza, V. Brotas, and C. A. E. Garcia. 2013. Shifts in the dominance between diatoms and cryptophytes during three late summers in the Bransfield Strait (Antarctic Peninsula). *Polar Biol.* 36: 537–547, doi:10.1007/s00300-012-1282-4
- Meredith, M. P., and J. C. King. 2005. Rapid climate change in the ocean west of the Antarctic Peninsula during the second half of the 20th century. *Geophys. Res. Lett.* 32: L19604, doi:10.1029/2005GL024042
- Meredith, M. P., and others. 2021. Local- and large-scale drivers of variability in the coastal freshwater budget of the Western Antarctic Peninsula. *J. Geophys. Res. Ocean.* 1–22, doi:10.1029/2021jc017172
- Miller, A. K., M. A. Kappes, S. G. Trivelpiece, and W. Z. Trivelpiece. 2010. Foraging-niche separation of breeding gentoo and chinstrap penguins, South Shetland Islands, Antarctica. *Condor* 112: 683–695, doi:10.1525/cond.2010.090221
- Miller, D. G. M., and I. Hampton. 1989. Krill aggregation characteristics: Spatial distribution patterns from hydroacoustic observations. *Polar Biol.* 10: 125–134, doi:10.1007/BF00239157

- Mitchell, G. B., and O. Holm-Hansen. 1991. Bio-optical properties of Antarctic Peninsula waters: differentiation from temperate ocean models. *Deep Sea Res.* 38: 1009–1028, doi:10.1016/0198-0149(91)90094-V
- Moline, M. A. 1996. Temporal dynamics and regulation of coastal Antarctic phytoplankton communities: spring/summer 1991–1994. University of California, Santa Barbara.
- Moline, M. A., H. Claustre, T. K. Frazer, O. Schofield, and M. Vernet. 2004. Alteration of the food web along the Antarctic Peninsula in response to a regional warming trend. *Glob. Chang. Biol.* 10: 1973–1980, doi:10.1111/j.1365-2486.2004.00825.x
- Moline, M. A., and B. B. Prézelin. 1996. Long-term monitoring and analyses of physical factors regulating variability in coastal Antarctic phytoplankton biomass, in situ productivity and taxonomic composition over subseasonal, seasonal and interannual time scales. *Mar. Ecol. Prog. Ser.* 145: 143–160, doi:10.3354/meps145143
- Montes-Hugo, M., S. C. Doney, H. H. Ducklow, W. Fraser, D. Martinson, S. E. Stammerjohn, and O. Schofield. 2009. Recent changes in phytoplankton communities associated with rapid regional climate change along the Western Antarctic Peninsula. *Science* 323: 1470–1473, doi:10.1126/science.1164533
- Morel, A., Y. Huot, B. Gentili, P. J. Werdell, S. B. Hooker, and B. A. Franz. 2007. Examining the consistency of products derived from various ocean color sensors in open ocean (Case 1) waters in the perspective of a multi-sensor approach. *Remote Sens. Environ.* 111: 69–88, doi:10.1016/j.rse.2007.03.012
- Nardelli, S. C., M. A. Cimino, J. A. Conroy, W. R. Fraser, D. K. Steinberg, and O. Schofield. 2021a. Krill availability in adjacent Adélie and gentoo penguin foraging regions. *Limnol. Ocean.* 66: 2234–2250, doi:10.1002/lno.11750
- Nardelli, S. C., P. C. Gray, and O. Schofield. 2021b. Developing a convolutional neural network to classify phytoplankton images collected with an Imaging FlowCytobot along the West Antarctic Peninsula. *MTS/IEEE OCEANS 2021 San Diego – Porto*: 1-7, doi: 10.23919/OCEANS44145.2021.9706072
- Nicol, S. 2006. Krill, currents, and sea ice: *Euphausia superba* and its changing environment. *Bioscience* 56: 111–120, doi:10.1641/0006-3568(2006)056[0111:KCASIE]2.0.CO;2
- Oliver, M. J., A. Irwin, M. A. Moline, W. Fraser, D. Patterson, O. Schofield, and J. Kohut. 2013. Adélie penguin foraging location predicted by tidal regime switching. *PLoS One* 8: e55163, doi:10.1371/journal.pone.0055163

- Oliver, M. J., and others. 2019. Central place foragers select ocean surface convergent features despite differing foraging strategies. *Sci. Rep.* 9: 1–10, doi:10.1038/s41598-018-35901-7
- Olson, R. J., and H. M. Sosik. 2007. A submersible imaging-in-flow instrument to analyze nano- and microplankton: Imaging FlowCytobot. *Limnol. Oceanogr. Methods* 5: 195–203, doi:10.4319/lom.2007.5.195
- Pan, B., and others. 2020. Environmental drivers on phytoplankton taxonomic composition in an Antarctic fjord. *Prog. Oceanogr.* 183: 1–43, doi:10.1016/j.pocean.2020.102295
- Passow, U., and C. A. Carlson. 2012. The biological pump in a high CO<sub>2</sub> world. *Mar. Ecol. Prog. Ser.* 470: 249–271, doi:10.3354/meps09985
- Picheral, M., C. E. Sanders, and J.-O. Irisson. 2017. EcoTaxa, a tool for the taxonomic classification of images. <http://ecotaxa.obs-vlfr.fr>
- Pickett, E. P., W. R. Fraser, D. L. Patterson-Fraser, M. A. Cimino, L. G. Torres, and A. S. Friedlaender. 2018. Spatial niche partitioning may promote coexistence of *Pygoscelis* penguins as climate-induced sympatry occurs. *Ecol. Evol.* 8: 9764–9778, doi:10.1002/ece3.4445
- Pikitch, E. K., and others. 2014. The global contribution of forage fish to marine fisheries and ecosystems. *Fish Fish.* 15: 43–64, doi:10.1111/faf.12004
- Polito, M. J., C. S. Reiss, W. Z. Trivelpiece, W. P. Patterson, and S. D. Emslie. 2013. Stable isotopes identify an ontogenetic niche expansion in Antarctic krill (*Euphausia superba*) from the South Shetland Islands, Antarctica. *Mar. Biol.* 160: 1311–1323, doi:10.1007/s00227-013-2182-z
- Prézelin, B. B., E. E. Hofmann, C. Mengelt, and J. M. Klinck. 2000. The linkage between Upper Circumpolar Deep Water (UCDW) and phytoplankton assemblages on the west Antarctic Peninsula continental shelf. *J. Mar. Res.* 58: 165–202, doi:10.1357/002224000321511133
- Reiss, C. S., A. M. Cossio, V. Loeb, and D. A. Demer. 2008. Variations in the biomass of Antarctic krill (*Euphausia superba*) around the South Shetland Islands, 1996–2006. *ICES J. Mar. Sci.* 65: 497–508, doi:10.1093/icesjms/fsn033
- Reiss, C. S., and others. 2017. Overwinter habitat selection by Antarctic krill under varying sea-ice conditions: implications for top predators and fishery management. *Mar. Ecol. Prog. Ser.* 568: 1–16, doi:10.3354/meps12099

- Rogers, A. D., and others. 2020. Antarctic futures: An assessment of climate-driven changes in ecosystem structure, function, and service provisioning in the Southern Ocean. *Ann. Rev. Mar. Sci.* 12: 87–120, doi:10.1146/annurev-marine-010419-011028
- Ross, R. M., E. E. Hofmann, and L. B. Quentin, eds. 1996. Foundations for ecological research west of the Antarctic Peninsula, American Geophysical Union.
- Ross, R. M., L. B. Quetin, T. Newberger, C. T. Shaw, J. L. Jones, S. A. Oakes, and K. J. Moore. 2014. Trends, cycles, interannual variability for three pelagic species west of the Antarctic Peninsula 1993-2008. *Mar. Ecol. Prog. Ser.* 515: 11–32, doi:10.3354/meps10965
- Rozema, P. D., H. J. Venables, W. H. van de Poll, A. Clarke, M. P. Meredith, and A. G. J. Buma. 2017. Interannual variability in phytoplankton biomass and species composition in northern Marguerite Bay (West Antarctic Peninsula) is governed by both winter sea ice cover and summer stratification. *Limnol. Oceanogr.* 62: 235–252, doi:10.1002/lno.10391
- Ruck, K. E., D. K. Steinberg, and E. A. Canuel. 2014. Regional differences in quality of krill and fish as prey along the Western Antarctic Peninsula. *Mar. Ecol. Prog. Ser.* 509: 39–55, doi:10.3354/meps10868
- Saba, G. K., and others. 2014. Winter and spring controls on the summer food web of the coastal West Antarctic Peninsula. *Nat. Commun.* 5: 4318, doi:10.1038/ncomms5318
- Sailley, S. F., H. W. Ducklow, H. V. Moeller, W. R. Fraser, O. M. Schofield, D. K. Steinberg, L. M. Garzio, and S. C. Doney. 2013. Carbon fluxes and pelagic ecosystem dynamics near two western Antarctic Peninsula Adélie penguin colonies: an inverse model approach. *Mar. Ecol. Prog. Ser.* 492: 253–272, doi:10.3354/meps10534
- Santora, J. A., and C. S. Reiss. 2011. Geospatial variability of krill and top predators within an Antarctic submarine canyon system. *Mar. Biol.* 158: 2527–2540, doi:10.1007/s00227-011-1753-0
- Schmidt, K., and A. Atkinson. 2016. Feeding and food processing in Antarctic krill (*Euphausia superba* Dana), p. 175–224. In *Biology and ecology of the Antarctic krill*.
- Schmidt, K., A. Atkinson, D. W. Pond, and L. C. Irel. 2014. Feeding and overwintering of Antarctic krill across its major habitats: The role of sea ice cover, water depth, and phytoplankton abundance. *Limnol. Oceanogr.* 59: 17–36, doi:10.4319/lo.2014.59.1.0017

- Schmidt, K., and others. 2011. Seabed foraging by Antarctic krill: Implications for stock assessment, benthic-pelagic coupling, and the vertical transfer of iron. *Limnol. Oceanogr.* 56: 1411–1428, doi:10.4319/lo.2011.56.4.1411
- Schofield, O., M. Brown, J. Kohut, S. Nardelli, G. Saba, N. Waite, and H. Ducklow. 2018. Changes in the upper ocean mixed layer and phytoplankton productivity along the West Antarctic Peninsula. *Philos. Trans. R. Soc. A* 376: 20170173, doi:10.1098/rsta.2017.0173
- Schofield, O., and others. 2017. Decadal variability in coastal phytoplankton community composition in a changing West Antarctic Peninsula. *Deep Sea Res. Part I Oceanogr. Res. Pap.* 124: 42–54, doi:10.1016/j.dsr.2017.04.014
- Scott, F. J., and others. 2005. Antarctic Marine Protists, F.J. Scott and H.J. Marchant [eds.]. Australian Biological Resources Study and Australian Antarctic Division.
- Sherrell, R. M., A. L. Annett, J. N. Fitzsimmons, V. J. Rocanova, and M. P. Meredith. 2018. A “shallow bathtub ring” of local sedimentary iron input maintains the Palmer Deep biological hotspot on the West Antarctic Peninsula shelf. *Phil Trans R Soc A* 376: 1–18.
- Siegel, V. 1988. A concept of seasonal variation of krill (*Euphausia superba*) distribution and abundance west of the Antarctic Peninsula, p. 219–230. In D. Sahrhage [ed.], *Antarctic ocean and resources variability*. Springer.
- Siegel, V., C. S. Reiss, K. S. Dietrich, M. Haraldsson, and G. Rohardt. 2013. Distribution and abundance of Antarctic krill (*Euphausia superba*) along the Antarctic Peninsula. *Deep. Res. Part I Oceanogr. Res. Pap.* 77: 63–74, doi:10.1016/j.dsr.2013.02.005
- Silk, J. R. D., S. E. Thorpe, S. Fielding, E. J. Murphy, P. N. Trathan, J. L. Watkins, and S. L. Hill. 2016. Environmental correlates of Antarctic krill distribution in the Scotia Sea and southern Drake Passage. *ICES J. Mar. Sci.* 73: 2288–2301, doi:10.1093/icesjms/fsw097
- Sosik, H. M., and R. J. Olson. 2007. Automated taxonomic classification of phytoplankton sampled with imaging-in-flow cytometry. *Limnol. Oceanogr. Methods* 5: 204–216, doi:10.4319/lom.2007.5.204
- Stammerjohn, S. E., D. G. Martinson, R. C. Smith, and R. A. Iannuzzi. 2008a. Sea ice in the western Antarctic Peninsula region: Spatio-temporal variability from ecological and climate change perspectives. *Deep. Res. Part II Top. Stud. Oceanogr.* 55: 2041–2058, doi:10.1016/j.dsr2.2008.04.026

- Stammerjohn, S. E., D. G. Martinson, R. C. Smith, X. Yuan, and D. Rind. 2008b. Trends in Antarctic annual sea ice retreat and advance and their relation to El Niño–Southern Oscillation and Southern Annular Mode variability. *J. Geophys. Res.* 113: C03S90, doi:10.1029/2007JC004269
- Stammerjohn, S., R. Massom, D. Rind, and D. Martinson. 2012. Regions of rapid sea ice change: An inter-hemispheric seasonal comparison. *Geophys. Res. Lett.* 39: L06501, doi:10.1029/2012GL050874
- Steinberg, D. K., and others. 2015. Long-term (1993–2013) changes in macrozooplankton off the Western Antarctic Peninsula. *Deep. Res. Part I Oceanogr. Res. Pap.* 101: 54–70, doi:10.1016/j.dsr.2015.02.009
- Sullivan, J. M., M. S. Twardowski, J. Ronald, V. Zaneveld, and C. C. Moore. 2013. Measuring optical backscattering in water, p. 189–224. In *Light Scattering Reviews 7*. Springer Praxis Books.
- Taki, K., T. Hayashi, and M. Naganobu. 2005. Characteristics of seasonal variation in diurnal vertical migration and aggregation of Antarctic krill (*Euphausia superba*) in the Scotia Sea, using Japanese fishery data. *CCAMLR Sci.* 12: 163–172.
- Tarling, G. A., and others. 2009. Variability and predictability of Antarctic krill swarm structure. *Deep. Res. Part I* 56: 1994–2012, doi:10.1016/j.dsr.2009.07.004
- Tarling, G. A., S. E. Thorpe, S. Fielding, T. Klevjer, A. Ryabov, and P. J. Somerfield. 2018. Varying depth and swarm dimensions of open-ocean Antarctic krill *Euphausia superba* Dana, 1850 (*Euphausiacea*) over diel cycles. *J. Crustac. Biol.* 38: 716–727, doi:10.1093/jcbiol/ruy040
- Thomas, E. R., G. J. Marshall, and J. R. McConnell. 2008. A doubling in snow accumulation in the western Antarctic Peninsula since 1850. *Geophys. Res. Lett.* 35: 1–5, doi:10.1029/2007GL032529
- Thompson, D. W. J., and S. Solomon. 2002. Interpretation of Recent Southern Hemisphere Climate Change. *Science* 296: 895–899, doi:10.1126/science.1069270
- Trathan, P. N., J. Forcada, and E. J. Murphy. 2007. Environmental forcing and Southern Ocean marine predator populations: Effects of climate change and variability. *Phil Trans R Soc B* 362: 2351–2365, doi:10.1098/rstb.2006.1953
- Trefault, N., and others. 2021. Annual phytoplankton dynamics in coastal waters from Fildes Bay, Western Antarctic Peninsula. *Sci. Rep.* 11: 1–17, doi:10.1038/s41598-020-80568-8

- Trivelpiece, W. Z., S. G. Trivelpiece, and N. J. Volkman. 1987. Ecological segregation of Adélie, gentoo, and chinstrap penguins at King George Island, Antarctica. *Ecology* 68: 351–361, doi:10.2307/1939266
- Turner, J., and others. 2005. Antarctic climate change during the last 50 years. *Int. J. Climatol.* 25: 279–294, doi:10.1002/joc.1130
- Venables, H. J., A. Clarke, and M. P. Meredith. 2013. Wintertime controls on summer stratification and productivity at the western Antarctic Peninsula. *Limnol. Ocean.* 58: 1035–1047, doi:10.4319/lo.2013.58.3.1035
- Vernet, M., D. Martinson, R. Iannuzzi, S. Stammerjohn, W. Kozlowski, K. Sines, R. Smith, and I. Garibotti. 2008. Primary production within the sea-ice zone west of the Antarctic Peninsula: I- Sea ice, summer mixed layer, and irradiance. *Deep. Res. Part II* 55: 2068–2085, doi:10.1016/j.dsr2.2008.05.021
- Vernet, M., and R. C. Smith. 2006. Measuring and modelling primary production in marine pelagic ecosystems, In J. Fahey and A. Knapp [eds.], *ILTER Net Primary Production Methods*. Oxford University Press.
- Volkman, N. J., P. Presler, and W. Trivelpiece. 1980. Diets of Pygoscelid penguins at King George Island, Antarctica. *Condor* 82: 373–378, doi:10.2307/1367558
- Walsh, J., C. S. Reiss, and G. M. Watters. 2020. Flexibility in Antarctic krill *Euphausia superba* decouples diet and recruitment from overwinter sea-ice conditions in the northern Antarctic Peninsula. *Mar. Ecol. Prog. Ser.* 642: 1–19, doi:10.3354/meps13325
- Ward, B. A., S. Dutkiewicz, and M. J. Follows. 2014. Modelling spatial and temporal patterns in size-structured marine plankton communities: Top-down and bottom-up controls. *J. Plankton Res.* 36: 31–47, doi:10.1093/plankt/fbt097
- Watanuki, Y., A. Kato, Y. Naito, G. Robertson, and S. Robinson. 1997. Diving and foraging behaviour of Adélie penguins in areas with and without fast sea-ice. *Polar Biol.* 17: 296–304, doi:10.1007/PL00013371
- Wiebe, P. H., D. Chu, S. Kaartvedt, A. Hundt, W. Melle, E. Ona, and P. Batta-Lona. 2010. The acoustic properties of *Salpa thompsoni*. *ICES J. Mar. Sci.* 67: 583–593, doi:10.1093/icesjms/fsp263
- Williams, T. D. 1995. *The penguins*, Oxford University Press.
- Winder, M., and D. E. Schindler. 2004. Climatic effects on the phenology of lake processes. *Glob. Chang. Biol.* 10: 1844–1856, doi:10.1111/j.1365-2486.2004.00849.x

- Woo, L. M., and C. Gourcuff. 2021. Delayed Mode QA/QC Best Practice Manual Version 3.0 Integrated Marine Observing System.
- Wright, S. W., S. W. Jeffrey, R. F. C. Mantoura, C. A. Llewellyn, T. Bjornland, D. Repeta, and N. Welschmeyer. 1991. Improved HPLC method for the analysis of chlorophylls and carotenoids from marine phytoplankton. *Mar. Ecol. Prog. Ser.* 77: 183–196, doi:10.3354/meps077183
- Xing, X., H. Claustre, S. Blain, F. D’Ortenzio, D. Antoine, J. Ras, and C. Guinet. 2012. Quenching correction for in vivo chlorophyll fluorescence acquired by autonomous platforms: A case study with instrumented elephant seals in the Kerguelen region (Southern Ocean). *Limnol. Oceanogr. Methods* 10: 483–495, doi:10.4319/lom.2012.10.483
- Zhang, X., and L. Hu. 2009. Scattering by pure seawater at high salinity. *Opt. Express* 17: 12685, doi:10.1364/oe.17.012685